



Fall 12-21-2011

Inhaled Oxygen as a Quantitative Intravascular MRI Contrast Agent

David T. Pilkinton

University of Pennsylvania, davt@mail.med.upenn.edu

Follow this and additional works at: <http://repository.upenn.edu/edissertations>

 Part of the [Biophysics Commons](#), and the [Radiology Commons](#)

Recommended Citation

Pilkinton, David T., "Inhaled Oxygen as a Quantitative Intravascular MRI Contrast Agent" (2011). *Publicly Accessible Penn Dissertations*. 450.

<http://repository.upenn.edu/edissertations/450>

This paper is posted at ScholarlyCommons. <http://repository.upenn.edu/edissertations/450>

For more information, please contact libraryrepository@pobox.upenn.edu.

Inhaled Oxygen as a Quantitative Intravascular MRI Contrast Agent

Abstract

Increasing the fraction of inspired oxygen (FiO_2) generates MR contrast by two distinct mechanisms: increased T_2 from deoxyhemoglobin dilution in venous compartments (blood oxygenation level-dependent effect or BOLD) and reduced T_1 from paramagnetic molecular oxygen dissolved in blood plasma and tissues. Many research and clinical applications using hyperoxic contrast have recently emerged, including delineating ischemic stroke penumbra, oxygen delivery to tumors, and functional MRI data calibration. However, quantitative measurements using this contrast agent depend on the precise knowledge of its effects on the MR signal – of which there remain many crucial missing pieces.

This thesis aims to obtain a more quantitative understanding of intravascular hyperoxic contrast *in vivo*, with the hope of increasing its precision and utility. Specifically, our work focuses on the following areas: (1) paramagnetic effects of molecular oxygen BOLD and arterial spin labeling (ASL) data, (2) degree and temporal characteristics of hyperoxia-induced reductions in cerebral blood flow (CBF), (3) use of oxygen in quantitative measurements of metabolism, and (4) biophysical mechanisms of hyperoxic T_1 contrast.

In Chapter 2, the artifactual influence of paramagnetic molecular oxygen on BOLD-modulated hyperoxic gas studies is characterized as a function of static field strength, and we show that optimum reduction in FiO_2 mitigates this effect while maintaining BOLD contrast. Since ASL measurements are highly sensitive to arterial blood T_1 (T_{1a}), the value of T_{1a} *in vivo* is determined as a function of arterial oxygen partial pressure in Chapter 3. The effect of both the degree and duration of hyperoxic exposure on absolute CBF are quantified using simultaneous ASL and *in vivo* T_{1a} measurements, as described in Chapter 4. In Chapter 5, hyperoxic gas calibration of BOLD/ASL data is used to measure cerebral oxygen metabolism in a hypermetabolic swine model, with our results comparing favorably to $^{17}\text{O}_2$ measurements of absolute metabolism. In Chapter 6, a model to describe the relationship between CBF, oxygen consumption, and hyperoxic T_1 reduction is developed, which allows for a more rigorous physiological interpretation of these data. Taken together, this work represents several important steps towards making hyperoxia a more quantitative MRI contrast agent for research and clinical applications.

Degree Type

Dissertation

Degree Name

Doctor of Philosophy (PhD)

Graduate Group

Biochemistry & Molecular Biophysics

First Advisor

Ravinder Reddy

Keywords

magnetic resonance imaging oxygen hyperoxia brain

Subject Categories

Biophysics | Radiology

INHALED OXYGEN AS A QUANTITATIVE INTRAVASCULAR MRI CONTRAST AGENT

David Thomas Pilkinton

A DISSERTATION

in

Biochemistry and Molecular Biophysics

Presented to the Faculties of the University of Pennsylvania

in Partial Fulfillment of the Requirements for the Degree of Doctor of Philosophy

2011

Supervisor of Dissertation

Ravinder Reddy
Professor of Radiology

Graduate Group Chairperson

Kathryn Ferguson
Associate Professor of Physiology

Dissertation Committee

Felix Wehrli	Professor of Radiology	Jeremy Magland	Research Assistant Professor of Radiology
Joshua Wand	Professor of Biochemistry	Sergei Vinogradov	Associate Professor of Biochemistry
Ari Borthakur	Assistant Professor of Radiology	Andrew Newberg	Director of Research, Brind Center, Jefferson Univ.

**INHALED OXYGEN AS A QUANTITATIVE INTRAVASCULAR
MRI CONTRAST AGENT**

COPYRIGHT

2011

David Thomas Pilkinton

Dedicated to my mother and father,

Janet and David

ACKNOWLEDGEMENTS

I want to express my sincere gratitude to my thesis advisor, Ravinder Reddy, and the members of my working thesis committee, Felix Wehrli, Ari Borthakur, Jeremy Magland, and Mark Elliott for their guidance along the way. I am also indebted to other faculty members who have also provided me with substantial support, especially John Detre and Joel Greenberg. I would also like to thank all the members of the Reddy lab, including graduate students, post-docs, and staff for their support. Special thanks to Susan Colleluori for all her assistance with all matter administrative and otherwise. I would also like to thank Eric Mellon, Santosh Gaddam, Victor Babu, Teruyuki Hiraki, Wes Baker, Kejia Cai, and Anup Singh for their assistance with experiments.

My heartfelt appreciation to my significant other, Jie Xu, for her love, support, and friendship. To my parents, Janet and David, to my sister, Julie, to my extended family, including all the Pilkintons and Wills, and to all of my friends – I could not have made it this far without your love and generosity. Thank you.

ABSTRACT

Inhaled Oxygen as a Quantitative Intravascular MRI Contrast Agent

David Thomas Pilkinton

Thesis Supervisor: Ravinder Reddy, PhD

Increasing the fraction of inspired oxygen (FiO_2) generates MR contrast by two distinct mechanisms: increased T_2 from deoxyhemoglobin dilution in venous compartments (blood oxygenation level-dependent effect or BOLD) and reduced T_1 from paramagnetic molecular oxygen dissolved in blood plasma and tissues. Many research and clinical applications using hyperoxic contrast have recently emerged, including delineating ischemic stroke penumbra, oxygen delivery to tumors, and functional MRI data calibration. However, quantitative measurements using this contrast agent depend on the precise knowledge of its effects on the MR signal – of which there remain many crucial missing pieces.

This thesis aims to obtain a more quantitative understanding of intravascular hyperoxic contrast *in vivo*, with the hope of increasing its precision and utility. Specifically, our work focuses on the following areas: (1) paramagnetic effects of molecular oxygen BOLD and arterial spin labeling (ASL) data, (2) degree and temporal characteristics of hyperoxia-induced reductions in cerebral blood flow (CBF), (3) use of oxygen in

quantitative measurements of metabolism, and (4) biophysical mechanisms of hyperoxic T_1 contrast.

In Chapter 2, the artifactual influence of paramagnetic molecular oxygen on BOLD-modulated hyperoxic gas studies is characterized as a function of static field strength, and we show that optimum reduction in FiO_2 mitigates this effect while maintaining BOLD contrast. Since ASL measurements are highly sensitive to arterial blood T_1 (T_{1a}), the value of T_{1a} *in vivo* is determined as a function of arterial oxygen partial pressure in Chapter 3. The effect of both the degree and duration of hyperoxic exposure on absolute CBF are quantified using simultaneous ASL and *in vivo* T_{1a} measurements, as described in Chapter 4. In Chapter 5, hyperoxic gas calibration of BOLD/ASL data is used to measure cerebral oxygen metabolism in a hypermetabolic swine model, with our results comparing favorably to $^{17}O_2$ measurements of absolute metabolism. In Chapter 6, a model to describe the relationship between CBF, oxygen consumption, and hyperoxic T_1 reduction is developed, which allows for a more rigorous physiological interpretation of these data. Taken together, this work represents several important steps towards making hyperoxia a more quantitative MRI contrast agent for research and clinical applications.

Table of Contents

Chapter 1: Theory and Technical Challenges of the Use of Inhaled Oxygen as an Intravascular MRI Contrast Agent.....	1
1.1 Overview.....	1
1.2 Physical Properties of Oxygen.....	2
1.3 Oxygen Delivery and Consumption <i>In Vivo</i>	4
1.3.1 Cellular Respiration.....	4
1.3.2 Oxygen Transport and Hemoglobin.....	4
1.3.3 Structure of Hemoglobin and Oxygen Binding.....	5
1.3.4 Arterial Partial Pressure of Oxygen and Blood Oxygen Content.....	8
1.3.5 Conservation of Mass: Fick's Principle.....	9
1.3.6 Hyperoxic Dilution of Deoxyhemoglobin.....	10
1.4 NMR Relaxation and Paramagnetic MR Contrast Agents.....	12
1.5 Blood Oxygenation and the Relaxivity of Deoxyhemoglobin.....	17
1.6 Relaxivity of Molecular Oxygen in Arterial Blood and Tissue.....	22
1.7 Oxygen Gas and Bulk Static Magnetic Field Shifts.....	24
1.8 Cerebral Oxygen Consumption, Blood Flow, and Volume During Hyperoxia.....	26
1.9 Safety of Inhalation of Hyperoxic Gas Mixtures.....	28
1.10 Current Applications of Hyperoxic MRI Contrast.....	32

1.11 Summary of the Technical Challenges in Using Hyperoxia as a Quantitative Intravascular Contrast Agent.....	33
1.12 Specific aims of the thesis research	34
1.12.1 Aim 1: Characterize the effects of molecular oxygen on BOLD-modulated hyperoxic contrast studies.....	34
1.12.2 Aim 2: Determine the change in the longitudinal relaxation time of arterial blood in vivo at arbitrary levels of hyperoxia.....	35
1.12.3 Aim 3: Quantify absolute cerebral blood flow during hyperoxia using arterial spin labeling.....	36
1.12.4 Aim 4: Implement hyperoxic gas calibration BOLD/ASL measurements of relative cerebral metabolic rate of oxygen in a hypermetabolic animal model.....	36
1.12.5 Aim 5: Develop a biophysical model of the dependence of cerebral blood flow and metabolism on hyperoxia-induced changes in the longitudinal relaxation rate of tissue.....	36
 Chapter 2: Characterization of Paramagnetic Effects of Molecular Oxygen on Blood Oxygenation Level-Dependent-Modulated Hyperoxic Contrast Studies.....	38
2.1 Overview.....	38
2.2 Introduction.....	39
2.3 Materials and Methods.....	41

2.3.1 Gas Delivery and MRI Hardware.....	41
2.3.2 Hyperoxic Challenge Paradigm.....	42
2.3.3 MRI Sequence Parameters.....	42
2.3.4 Data Analysis.....	44
2.3.5 Calculation of Regional Cerebral Blood Volume.....	45
2.4 Localization of Hyperoxia-Induced Positive and Negative EPI Signal Changes.....	46
2.5 Hyperoxia-Induced Negative EPI Signal Changes versus FiO_2	48
2.6 Measurement of Hyperoxia-Induced B_0 field Perturbation versus FiO_2	50
2.7 CBV Measurement Accuracy at Low FiO_2	53
2.8 Chapter Discussion.....	55
 Chapter 3: <i>In Vivo</i> Measurement of Longitudinal Relaxation Time of Arterial Blood During Hyperoxia.....	 62
3.1 Overview.....	62
3.2 Introduction.....	62
3.3 Material and Methods.....	64
3.3.1 Phantom Study of Oxygen Longitudinal Relaxivity.....	64
3.3.2 Animals.....	65
3.3.3 Hyperoxia Challenge Paradigm.....	66
3.3.4 MRI Hardware.....	66
3.3.5 Measurement of Arterial Blood T_1 (T_{1a}).....	67

3.3.6 Data Analysis.....	69
3.4 Inversion-Prepared ΔM as a Function of Preparation Time.....	70
3.5 Baseline T_{1a} and Response to Hyperoxia.....	71
3.6 Longitudinal Relaxivity of Oxygen in PBS and Arterial Blood <i>In Vivo</i>	74
3.7 Chapter Discussion.....	77
3.8 Future Directions.....	79
 Chapter 4: Absolute Quantification of Cerebral Perfusion with Pulsed Arterial Spin Labeling During Hyperoxia.....	80
4.1 Overview.....	80
4.2 Introduction.....	80
4.3 Material and Methods.....	82
4.3.1 Animal Preparation.....	82
4.3.2 Hyperoxia Challenge Paradigms.....	82
4.3.3 Measurement of Cerebral Blood Flow (CBF) with Pulsed ASL.....	85
4.3.4 Data Analysis.....	90
4.4 Arterial Blood Gas and Blood Pressure Analysis.....	91
4.5 Cerebral Blood Flow Mapping with Correction for T_{1a}	92
4.6 ROI Analysis of Hyperoxia-Induced CBF Reduction.....	97

4.7 Chapter Discussion.....	99
 Chapter 5: Hyperoxic Calibrated Quantitative fMRI for the Measurement of Regional Cerebral Metabolic Rate of Oxygen in a Hypermetabolic Swine Model.....	 103
5.1 Overview.....	103
5.2 Introduction.....	103
5.3 Material and Methods.....	106
5.3.1 <i>Animal Preparation</i>	106
5.3.2 <i>Preparation and Administration of 2,4-Dinitrophenol</i>	107
5.3.3 <i>Hyperoxia and Hypercapnia Challenge Paradigms</i>	108
5.3.4 <i>MRI Hardware</i>	108
5.3.5 <i>MRI Sequences</i>	109
5.3.6 <i>BOLD and Arterial Spin Labeling Analysis</i>	110
5.3.7 <i>Calculation of Regional Cerebral Metabolic Rate of Oxygen: Hyperoxic and Hypercapnia Calibration Methods</i>	111
5.4 Physiologic Responses to Hyperoxia, Hypercapnia, and DNP.....	120
5.5 Arterial Blood Gases.....	123
5.6 BOLD and CBF Signal Responses to Hyperoxia, Hypercapnia, and DNP.....	124
5.7 Calculation of the Calibration Factor M for Hyperoxia and Hypercapnia.....	129
5.8 CMRO ₂ Calculation with Hyperoxia and Hypercapnia.....	130

5.9 Chapter Discussion.....	134
 Chapter 6: Investigation of the Dependence of Cerebral Blood Flow and Oxygen Consumption on Hyperoxia-Induced Changes in the Longitudinal Relaxation Time.....	139
6.1 Overview.....	139
6.2 Introduction.....	139
6.3 Theory.....	141
6.4 Material and Methods.....	147
6.4.1 <i>Animal</i>	148
6.4.2 <i>Hyperoxia and Hypercapnia Inhalation Challenge Paradigms</i>	148
6.4.3 <i>MRI Hardware</i>	149
6.4.4 <i>Measurement of CBF During Hypercapnia</i>	149
6.4.5 <i>Measurement of the Longitudinal Relaxation Time</i>	150
6.4.6 <i>Data Analysis</i>	150
6.5 Cerebral Blood Flow versus Hypercapnia Level.....	151
6.6 T_1 Mapping.....	152
6.7 Hyperoxia-Induced R_1 versus CBF.....	153
6.8 Chapter Discussion.....	155

Chapter 7: Summary and Future Directions.....	158
7.1. Future Directions	158
7.2. Summary of dissertation	161
References.....	164

List of Tables

Chapter 1: Theory and Technical Challenges of the Use of Inhaled Oxygen as an Intravascular MRI Contrast Agent

Chapter 2: Characterization of Paramagnetic Effects of Molecular Oxygen on Blood Oxygenation Level-Dependent-Modulated Hyperoxic Contrast Studies

Table 2.1. Mean Percent Negative Voxels for All Subjects within Specified Tissue Regions for $\text{FiO}_2=1.0$ and 0.5	53
Table 2.2. Mean Global CBV Values (mL / 100 g) for All Subjects Measured with 100% and 50% Inhaled Oxygen.....	55

Chapter 3: *In Vivo* Measurement of Longitudinal Relaxation Time of Arterial Blood During Hyperoxia

Table 3.1. Measured T_{1a} Values in Whole Brain ROIs During Normoxia ($\text{FiO}_2 = 0.3$) and Hyperoxia ($\text{FiO}_2 = 1.0$).....	74
--	----

Chapter 4: Absolute Quantification of Cerebral Perfusion with Pulsed Arterial Spin Labeling During Hyperoxia

Table 4.1. Arterial Blood Gas Parameters for Normoxia and Hyperoxia in 1.5% Isoflurane Anesthesia (Group I).....	91
Table 4.2. Arterial Blood Gas Parameters for Graded Levels of Hyperoxia in 1.5% Isoflurane Anesthesia (Group II).....	92

Chapter 5: Hyperoxic Calibrated Quantitative fMRI for the Measurement of Regional Cerebral Metabolic Rate of Oxygen in a Hypermetabolic Swine Model

Table 5.1. Arterial Blood Gas Parameters for Hyperoxia, Hypercapnia, and Post-DNP Infusion.....	123
Table 5.2a. Calculation of Calibration Factor M with Hyperoxia†.....	130
Table 5.2b. Calculation of Calibration Factor M with Hypercapnia†.....	131
Table 5.3. Calculation of Relative CMRO ₂ After DNP Infusion†.....	134

Chapter 6: Investigation of the Dependence of Cerebral Blood Flow and Oxygen Consumption on Hyperoxia-Induced Changes in the Longitudinal Relaxation Time

List of Illustrations

Chapter 1: Theory and Technical Challenges of the Use of Inhaled Oxygen as an Intravascular MRI Contrast Agent

Figure 1.1. The hemoglobin oxygen binding curve.....	7
Figure 1.2. The arterial blood oxygen content as a function of arterial partial pressure of oxygen.....	9
Figure 1.3. The relative change in the dHb concentration versus PaO_2	12
Figure 1.4. R_2 versus oxygen saturation (1-Y) at 1.5, 3, and 4.7 Tesla.....	21

Chapter 2: Characterization of Paramagnetic Effects of Molecular Oxygen on Blood Oxygenation Level-Dependent-Modulated Hyperoxic Contrast Studies

Figure 2.1. Percent signal change from baseline upon $\text{FiO}_2=1.0$	47
Figure 2.2. Comparison of percent negative signal change from baseline for $\text{FiO}_2 = 1.0$ and 0.5 with their associated EPI images.....	49
Figure 2.3. Tissue masks of cerebrospinal fluid , gray matter, and white matter with a registered, unwarped EPI image.....	50
Figure 2.4. Baseline B_0 maps and change in B_0 after different levels of oxygen inhalation at 3T and 7T.....	52
Figure 2.5. Percent difference and CBV maps in mL/100 g tissue calculated according to Eq. [2.1].....	54

Chapter 3: *In Vivo* Measurement of Longitudinal Relaxation Time of Arterial Blood During Hyperoxia

Figure 3.1. Pulse sequence diagram of the PICORE sequence with a global inversion preparation.....	68
--	----

Figure 3.2. A representative set of PICORE signal difference ΔM (control minus tag) images.....	72
Figure 3.3. PICORE signal difference (ΔM) versus inversion preparation time τ in a whole brain ROI.....	73
Figure 3.4. Effect of oxygen concentration on R_1 in a phosphate-buffered saline (PBS) phantom (a) and effect of arterial oxygen tension on R_1 of arterial blood.....	76

Chapter 4: Absolute Quantification of Cerebral Perfusion with Pulsed Arterial Spin Labeling During Hyperoxia

Figure 4.1. Hyperoxic challenge paradigms used for Group I and II animals.....	84
Figure 4.2. A multi-shot fast spin echo sequence (FSE) quantitative imaging of perfusion using a single subtraction with thin-slice TI_1 periodic saturation (Q2TIPS) based on proximal inversion with control for off-resonance (PICORE) tagging.....	87
Figure 4.3. T_2 -weighted structural images with ROIs (outlined in white) for analysis of regional CBF values (corresponding columns below), from a representative animal.....	94
Figure 4.4. Representative signal time course of ΔM (control minus tag) and control image signal intensity during normoxia ($FiO_2 = 0.3$) and hyperoxia ($FiO_2 = 1.0$).....	95
Figure 4.5. Overlays of the measured reduction (% decrease) on anatomical images of the CBF maps from a representative animal and the effect of FiO_2 on whole-brain relative CBF.....	96
Figure 4.6. Mean calculated CBF values (ml/100 g/min) in seven ROIs (both hemispheres; see Fig. 4.3) during normoxia ($FiO_2 = 0.3$) and hyperoxia ($FiO_2=1.0$) uncorrected and corrected for T_{1a} during hyperoxia.....	98

Chapter 5: Hyperoxic Calibrated Quantitative fMRI for the Measurement of Regional Cerebral Metabolic Rate of Oxygen in a Hypermetabolic Swine Model

Figure 5.1. Physiological monitoring traces for the entire experiment from a representative animal.....	122
Figure 5.2. Baseline-normalized changes in BOLD and CBF for each experimental condition.....	126
Figure 5.3. BOLD and ASL signal traces from a whole brain ROI from a representative animal.....	128
Figure 5.4. CMRO ₂ signal traces from a whole brain ROI from a representative animal immediately after DNP infusion.....	132
Figure 5.5. CMRO ₂ change after thirty minutes of DNP administration in percent increase from baseline.....	133

Chapter 6: Dependence of Cerebral Blood Flow and Oxygen Consumption on Hyperoxia-Induced Changes in the Longitudinal Relaxation Time

Figure 6.1. The relationships between $\Delta\Delta R_1$, CBF, and CMRO ₂ as derived by Eq. [6.10].....	147
Figure 6.2. Relative CBF at each hypercapnia level from a representative animal with a co-registered structural image.....	152
Figure 6.3. Quantitative T ₁ map from a representative animal with a co-registered structural image.....	153
Figure 6.4. The change in hyperoxic longitudinal relaxation enhancement ($\Delta\Delta R_1$) versus relative change in the CBF (% increase from baseline).....	154

Chapter 1: Theory and Technical Challenges of Using Inhaled Oxygen as an Intravascular MRI Contrast Agent

1.1 Overview

Understanding how oxygen is delivered to and consumed in tissue are central questions in physiology. Many of the details concerning how these processes occur are still the subject of ongoing scientific investigation. Adequate oxygen delivery to tissues at a rate that meets or exceeds its demand is critical for life, and impairments in this process are centrally important to many diseases, including stroke, cancer, and Alzheimer's disease. Therefore, there is a tremendous potential research and clinical benefit in developing imaging techniques that are sensitive to the delivery and utilization of oxygen *in vivo*.

Magnetic resonance imaging (MRI) is capable of utilizing a wide variety of modalities to monitor oxygen physiology *in vivo*. One important technique to monitor oxygen delivery and consumption involves the use of hyperoxic (fraction of inspired oxygen or $\text{FiO}_2 > 0.21$) inhalation contrast. The work undertaken in this thesis consists of important steps towards further developing hyperoxia as a quantitative intravascular contrast agent. But before discussing this work in detail, several fundamental concepts must be understood, including: the physical properties of oxygen, the mechanisms of *in vivo* oxygen delivery and utilization, the relaxivities of hemoglobin and molecular oxygen, static field shifts

from oxygen gas, the physiologic effects of hyperoxia, and the applications of hyperoxic MR contrast.

1.2 Physical Properties of Oxygen

At standard temperature and pressure, oxygen is an odorless, pale blue, diatomic gas with the molecular formula of O_2 (1). Two oxygen atoms are covalently bonded in a spin triplet configuration. Triplet oxygen is the normal ground state of the O_2 molecule and it has two unpaired electrons occupying two degenerate molecular orbitals (2). In its triplet form, oxygen is paramagnetic, the property of a material indicating that it generates an attractive magnetic field in the presence of an external magnetic field. The paramagnetism of oxygen is due to its unpaired electrons, which have their own spin magnetic moments (2). While gaseous and dissolved oxygen exhibit mild paramagnetism, liquid oxygen is strongly paramagnetic and can even be held up by a strong permanent magnet (1).

Oxygen has three naturally occurring stable isotopes: ^{16}O , ^{17}O , and ^{18}O , with ^{16}O being by far the most common form with a 99.8% natural abundance level. ^{18}O is an important precursor for fluorodeoxyglucose (FDG), which is used in positron emission tomography (PET). To create ^{18}F for FDG, enriched water, $H_2\ ^{18}O$, is bombarded with high energy hydrogen ions in a cyclotron. ^{17}O is the only stable oxygen isotope with a nuclear spin

(5/2), making it the only directly detectable form of oxygen by NMR. It has been used *in vivo* for a direct measurement of regional metabolism, since the formation of H_2^{17}O from aerobic metabolism is detectable by an increase in the proton transverse relaxation rate. The metabolic rate of oxygen can then be determined by measuring the rate of formation of H_2^{17}O (3).

Oxygen has a similar solubility in water to other non-polar, non-chemically reactive gases. The formation of dissolved oxygen gas in water is well-described by Henry's law, which states that, at a constant temperature, the amount of gas that will dissolve into a liquid is directly proportional to the partial pressure of the gas in equilibrium with the liquid. The solubility of the gas can be described by the measurement of Henry's law constant:

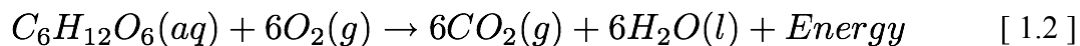
$$p = k_H \cdot c \quad [1.1]$$

Oxygen is approximately twice as soluble in water as nitrogen. Temperature is inversely related to the solubility of oxygen, with about 20°C water dissolving approximately twice the oxygen of 37°C water. The solubility of oxygen in water at 37°C is 0.0031 mL/dL/mm Hg. It is also interesting to note that oxygen is approximately four times more soluble in lipid than in water. The relative lipophilicity of oxygen is due to its nonpolar structure.

1.3 Oxygen Delivery and Consumption *In Vivo*

1.3.1 Cellular Respiration

Since continuous cellular respiration is crucial to the biology of obligate aerobes, a continuous delivery of oxygen to tissues is necessary for the viability of almost all multi-cellular organisms. Animals that are not adapted to hypoxia cannot survive for more than a few minutes without oxygen. Most cellular respiration is aerobic and can be described as:



Energy created by respiration is converted to an energy storage molecule, adenosine-5'-triphosphate (ATP). The metabolic rate of consumption of oxygen is substantial in humans, as the body turns over more than its own weight in ATP every day (4).

1.3.2 Oxygen Transport and Hemoglobin

As stated above, the amount of oxygen that can be dissolved in water is relatively small. Animals have evolved a solution to this problem with the molecule hemoglobin, an iron-containing oxygen-transport metalloprotein in the red blood cells (RBC) of all vertebrates. Red blood cells are approximately 95% hemoglobin by dry weight, and hemoglobin makes up around 35% of total RBC content. Each molecule of hemoglobin can carry up to four molecules of O₂, and approximately 1.34 mL O₂ can be carried per

gram of hemoglobin. At a partial pressure of oxygen of 100 mm Hg, the carrying capacity of oxygen in the blood is increased by approximately 65 fold over blood plasma alone. Hemoglobin also carries approximately 10% of respiratory carbon dioxide in the form of carbaminohemoglobin.

1.3.3 Structure of Hemoglobin and Oxygen Binding

The hemoglobin molecule has a quaternary structure consisting of four globular protein subunits. In humans, the most common hemoglobin type is hemoglobin A, which consists of two α and two β subunits non-covalently bound as a tetramer. These subunits are structurally similar and approximately the same size. Each subunit has a protein chain arranged into a set of alpha-helix structural elements, which assemble to form a globin fold arrangement. In this arrangement, a pocket is formed that tightly binds a heme group, which consists of a charged atom of iron (Fe) held inside a heterocyclic ring known as a porphyrin. The iron atom is the site of oxygen binding and it can be in the Fe^{2+} or Fe^{3+} state. Oxygen can only bind in the Fe^{2+} state, which reversibly oxidizes it to Fe^{3+} and transforms oxygen into superoxide.

Due to the structural features of hemoglobin, it exhibits cooperative binding of oxygen. In general, hemoglobin exists as oxyghemoglobin and deoxyhemoglobin, depending on whether it is saturated or desaturated with oxygen, respectively. When an oxygen molecule binds to hemoglobin, steric conformational changes occur to increase the

affinity of hemoglobin for additional oxygen molecules on the remaining binding sites. This results in a sigmoidal or S-shaped hemoglobin oxygen binding curve (Fig. 1.1). The oxygen binding curve is the relationship between the saturation of oxygen and the arterial partial pressure of oxygen (PaO_2); for human hemoglobin, it is described by the Severinghaus equation:

$$SaO_2 = \frac{1}{1 + \left(\frac{23,400}{(PaO_2)^3 + 150 \cdot PaO_2} \right)} \quad [1.3]$$

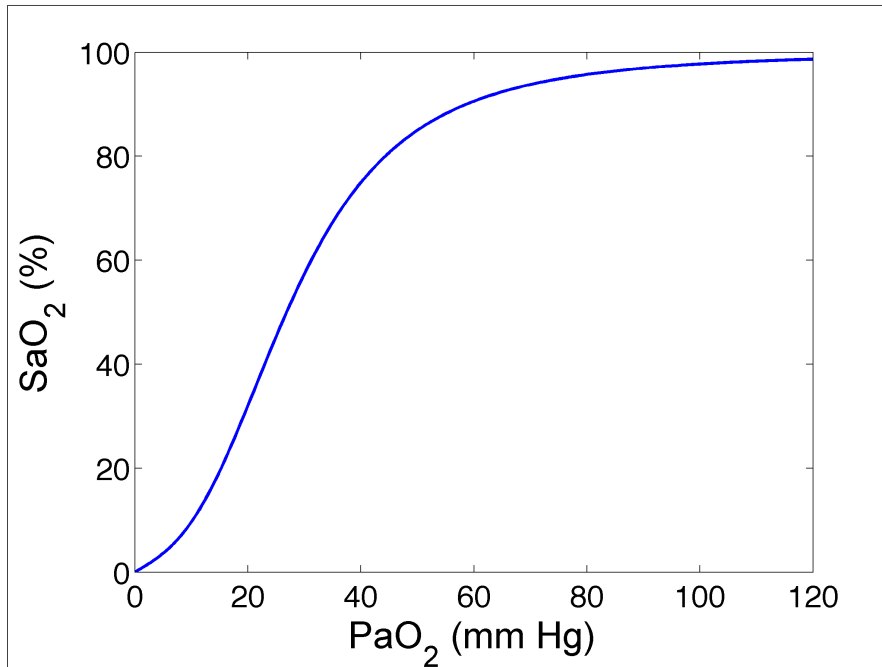


Figure 1.1. The hemoglobin oxygen binding curve. The curve has a sigmoidal shape that is due to the cooperative binding of hemoglobin, created through steric conformational changes induced from binding oxygen molecules.

Hemoglobin has two distinct structural states, a taut form and a relaxed form. The taut form has lower affinity to oxygen than the relaxed form. Physiological blood factors including high partial pressure of CO₂, low pH, and high 2,3-bisphosphoglycerate levels favor the taut form, which lowers the affinity for oxygen of hemoglobin and results in a rightward shift of the hemoglobin-oxygen binding curve. This action assists in off-loading oxygen from hemoglobin in the capillaries, where the partial pressure of CO₂ is high and the pH is low. The opposite physiological changes increase the oxygen binding

affinity and produce a leftward shift of oxygen binding curve, which is important in assisting the uptake of oxygen in the lungs.

1.3.4 Arterial Partial Pressure of Oxygen and Blood Oxygen Content

When inhaled at normal atmospheric pressure and concentration, the partial pressure of oxygen (pO_2) is approximately 160 mm Hg. Taking water vapor pressure into account, the pO_2 in the trachea is reduced to approximately 150 mm Hg. By the time oxygen reaches the alveoli, the site of final gas exchange in the lung, the pO_2 is approximately 100 mm Hg. This is because the alveolar pO_2 represents a balance between the removal of oxygen by the pulmonary capillaries and the supply of oxygen from the airway.

Total arterial blood oxygen content is the sum of oxygen bound to hemoglobin and dissolved in the plasma. When PaO_2 is 100 mm Hg, hemoglobin is approximately 98% saturated. Based on its oxygen carrying capacity, the content of oxygen in hemoglobin is approximately 19.6 mL_{O₂} per dL of blood. The solubility of oxygen in the plasma is essentially the same as water. Therefore, the oxygen content of the plasma for this PaO_2 is 0.31 mL_{O₂} per dL of blood, or 1.6% of the total oxygen content of blood. As normobaric oxygen concentration increases to a partial pressure of 760 mm Hg, PaO_2 will increase to approximately 570 mm Hg (the precise maximum level depending on the particular details of lung ventilation). At 570 mm Hg, content of oxygen in hemoglobin increases to only about 20.1 mL_{O₂} per dL of blood, but plasma oxygen content increases

to 1.8 mL_{O2} per dL of blood. Therefore, the overall increase in the oxygen content of blood from a PaO₂ of 100 to 570 mm Hg is approximately 9.6%. The relationship of PaO₂ to the arterial blood oxygen content (CaO₂) is shown in Fig. 1.2. The process is described in further detail in Chapter 5.

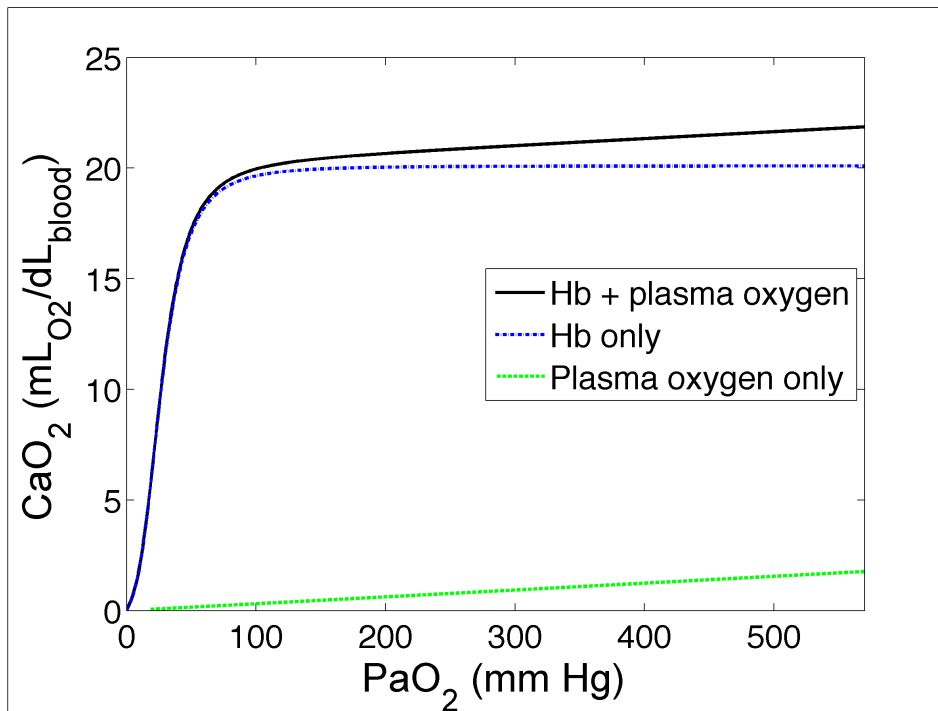


Figure 1.2. The arterial blood oxygen content (CaO₂) as a function of arterial partial pressure of oxygen (PaO₂).

1.3.5 Conservation of Mass: Fick's Principle

The conservation of mass principle indicates that the total amount of oxygen delivered to the tissue from the arteries must either be consumed by the tissue or must exit via the

venous blood. This is also known as Fick's principle, and when concerning oxygen consumption in the brain, is often stated in the following forms, which are equivalent:

$$CMRO_2 = CBF \cdot (Ca_{O_2} - Cv_{O_2}) \quad [1.4]$$

$$CMRO_2 = CBF \cdot Ca_{O_2} \cdot OEF \quad [1.5]$$

where $CMRO_2$ is the cerebral metabolic rate of oxygen in mL of oxygen per 100 g of tissue per minute, Cv_{O_2} is the oxygen content of venous blood, Sv_{O_2} is the saturation of venous blood, and OEF is the oxygen extraction fraction, the difference in saturation of arterial and venous blood. Based on Fick's principle, we can calculate the regional metabolic rate of oxygen consumption in tissue if we know the arterial oxygen content, the regional blood flow, and its regional venous oxygen content. While blood flow and venous oxygen concentration must be known locally, it is generally a safe assumption that the arterial blood oxygen concentration is a global value and the same in all regions.

1.3.6 Hyperoxic Dilution of Deoxyhemoglobin

As can be seen from Eqs. [1.4] and [1.5], if the arterial concentration of oxygen is increased while metabolism and flow remain constant, the saturation of venous blood must also increase. If we can assume that hyperoxic gas does not affect the blood flow or metabolism of oxygen significantly (5), then oxygen can be considered to produce a change in the venous saturation that is directly proportional to the excess concentration of oxygen in the arterial blood (6).

Although there are regional variations in flow and metabolism values at rest, PET studies using ^{15}O have found that the resting OEF is remarkably stable and consistent throughout the brain (7). This is important for measurements using the dilution of deoxyhemoglobin (dHb) with hyperoxia, since, if a local value of OEF can be assumed, then the local saturation of venous blood can be determined from the blood flow and the arterial oxygen content. The concentration of dHb is known to be directly proportional to venous saturation. If we assume a value of $\text{OEF}=0.3$ (8), a quantitative relationship between changes in dHb and PaO_2 , as shown in Fig. 1.3, can be produced. This line of argument is very important for calibrating BOLD measurements of CMRO_2 with hyperoxia and is discussed more thoroughly in Chapter 5. From Fig. 1.3, we can see that changing the PaO_2 from 100 to 570 mm Hg results in a reduction of deoxyhemoglobin concentration by more than 20%.

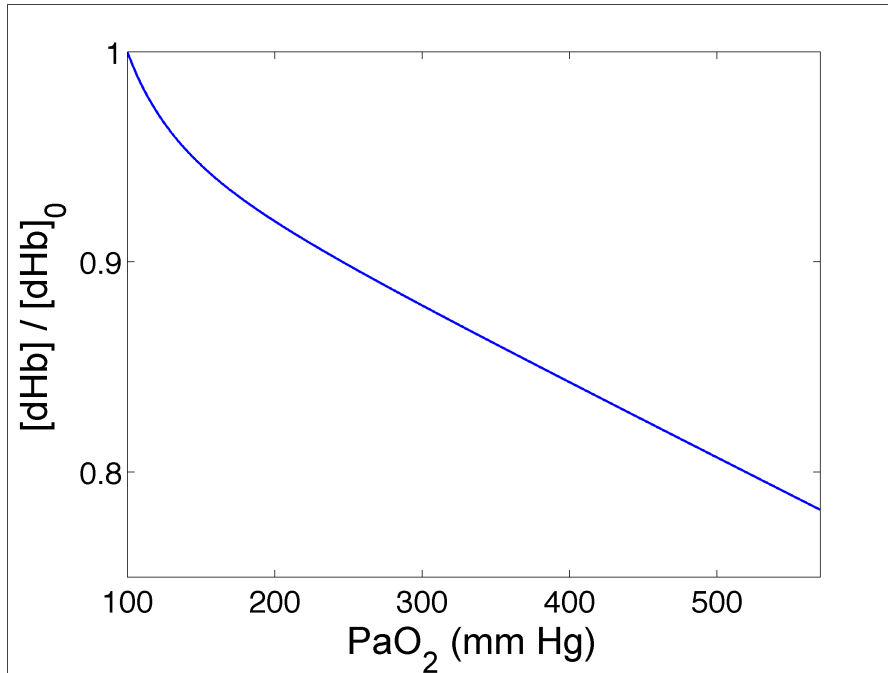


Figure 1.3. The relative change in the deoxyhemoglobin concentration versus PaO₂ (assuming an OEF=0.3 and no change in blood flow or oxygen consumption).

1.4 NMR Relaxation and Paramagnetic MR Contrast Agents

From thermal agitation, molecules undergo random translation and rotational motion, and the nuclear spins are affected by rapidly fluctuating microscopic magnetic fields from nearby nuclear and electron paramagnetic spins. These local fluctuating fields provide a mechanism for spins to return to the thermal equilibrium after they are perturbed by a radiofrequency magnetic field pulse. A mathematical description of nuclear magnetic resonance relaxation mechanisms was first developed by Bloembergen and his colleagues in what is now known as the Bloembergen-Purcell-Pound (BPP) theory (9). In this theory, time series analysis is used to model the random field fluctuations with an

exponential autocorrelation function of the form $\exp(-t/\tau_c)$, where τ_c is the correlation time. The correlation time is of the order of the time a molecule takes to turn through a radian or translate over a distance comparable to its size. The Fourier transform of the autocorrelation function is referred to as the spectral density, and it describes the frequency distribution of the energy of these fluctuating magnetic fields. Short correlation times correspond to fast molecular motions, with increased energy at higher frequencies, while long correlation times correspond to slow molecular motions, with increased energy at lower frequencies.

Nuclear magnetic relaxation can be separated into two distinct processes, spin-lattice and spin-spin relaxation. Spin-lattice relaxation is the process by which spins return to thermal equilibrium from a perturbation by an RF pulse and can be described by a single time constant, T_1 . T_1 is also referred to as the longitudinal relaxation time because it determines the rate of approach of the perturbed magnetization back to its equilibrium position lying parallel to the static magnetic field. An accurate phenomenological description of the spin-lattice relaxation is a monotonic exponential recovery process to the equilibrium magnetization value, which was first described by Bloch (10). Spin-lattice relaxation occurs primarily from motions at or near the resonance (Larmor) frequency, ω_0 ; it is insensitive to low frequencies ($\ll \omega_0$) and high frequencies ($\gg \omega_0$).

Spin-spin relaxation, described by T_2 , is the process by which nuclei interact with other magnetic moments to change their phase relative to one another, also known as phase decoherence. T_2 is also called the transverse relaxation time because it reflects the decay of magnetization lying orthogonal to the static magnetic field. The phenomenological description of the spin-spin relaxation is a monotonic exponential decay process. Unlike spin-lattice relaxation, spin-spin relaxation is sensitive to low frequency processes in addition to those at the Larmor frequency.

Relaxation processes are produced by two distinct physical mechanisms: magnetic moments of nuclear and electron spins (i) on the same molecule (intramolecular) and (ii) on other adjacent molecules (intermolecular). An analysis of the forces between spins shows that the strength of the interaction is proportional to the inverse of distance between the spins to the sixth power (11). This means that only close neighbors of a spin provide a significant contribution to its relaxation process.

The intra- and intermolecular interactions between spins represent different physical processes. The intramolecular interaction is dominated by the random rotational motion of the molecule and is characterized by a rotational correlation time. On the other hand, the random translational motion of neighboring spins from diffusion dominates the intermolecular interaction, which is described by a translational correlation time (11). Rotational and/or translational motions of nearby spins described by correlations times whose inverse is at the Larmor frequency will have the most significant effect on T_1 . The

effects on T_2 become larger with increasingly slow rotational and/or translational motions, i.e. longer correlations times. When the motions of neighboring spins are so rapid that the correlation times are much less than the inverse of Larmor frequency (i.e. the “extreme narrowing limit”), the effects on T_1 and T_2 are equal.

This description of the intermolecular contribution to relaxation is not complete, however, because this interaction depends not only on the transverse correlation time but also on the time scale of the interaction between spins. This interaction was first described by Bloembergen (12) in his account of the anomalous inequality of T_1 and T_2 in dilute aqueous solutions of the paramagnetic ions Mn^{2+} and Gd^{3+} . For these ions, the proton transverse relaxation rates are larger than the longitudinal rates in aqueous solution due to the spin exchange interaction between the bulk water and the hydration sphere around the ion. The probability of the water molecule being adjacent to the ion is larger for these ions than for other paramagnetic ions, such as Fe^{3+} , where the T_1 is equal to T_2 . By increasing the interaction time of the water and paramagnetic ions, the spectral density is shifted to lower frequencies. While this process decreases T_1 and T_2 , it has a larger effect on T_2 due to its low frequency sensitivity.

Paramagnetic molecules have magnetic moments that are many orders of magnitude stronger than nuclear magnetic moments, and through their translational diffusion, they produce strong intermolecular interactions that dominate relaxation rates of neighboring nuclei. Since they produce large effects on the relaxation times, paramagnetic molecules

are valuable sources of MR contrast. The effect of a paramagnetic molecule on the relaxation rate can be quantified as the relaxivity or r , which is the change in the relaxation rate per unit of concentration of the contrast agent:

$$r_i = \frac{(R_i - R_{i0})}{c} \quad [1.6]$$

where $i=1,2$, $R_i = (1/T_i)$, and c corresponds to the concentration of contrast agent. It should be noted that this linear description of relaxivity is only an accurate description of the pure liquids in a single, homogenous compartment. The relaxivity of paramagnetic contrast agents in tissue is substantially more complex, since the relaxation mechanisms involve factors such as local inhomogeneities and exchange between multiple compartments. Despite this fact, the use of this simplified linear model is actually a good approximation for most paramagnetic contrast agents in tissue, as we will show below.

In summary, we have provided a basic overview of the nuclear magnetic relaxation processes, with a focus on intermolecular interactions that describe the effects of paramagnetic molecules. A complete mathematical description of spin relaxation and its intra- and intermolecular contributions is beyond the scope of this work, but it is described in detail by the work of Bloembergen, et al. (9,11,12) and Solomon (13). A more rigorous description of relaxation based on density matrix formalism was developed by Kubo and Tomita (14), which was further generalized by the work of Gutowsky and

Woessner (15).

1.5 Blood Oxygenation and Relaxivity of Deoxyhemoglobin

Early in the study of hemoglobin, it was discovered that deoxyhemoglobin was paramagnetic and oxyhemoglobin was diamagnetic (16). Given that the lowest energy configurations of oxygen and iron are paramagnetic, discovering that oxyhemoglobin was diamagnetic was somewhat unexpected. The conclusion to this finding must be that some physical process occurs in the interaction between oxygen and iron in hemoglobin to alter the paramagnetism of both species and make their combination diamagnetic. In this case, the low-spin Fe^{3+} and superoxide anion ($\cdot\text{O}_2^-$) that form upon oxygen binding to hemoglobin collectively have two unpaired electrons that couple antiferromagnetically to give diamagnetic properties. This has been proven true by various experiments (17).

Since deoxyhemoglobin is paramagnetic and oxyhemoglobin is diamagnetic, the change in the oxygenation of blood can be determined by analyzing its relaxation times. Deoxyhemoglobin primarily affects the transverse relaxation time. Hemoglobin is a large molecule at 68 kDa, and under normal circumstances, all deoxyhemoglobin in the blood is compartmentalized within red blood cells, which are approximately 6 μm in diameter. These large sizes means deoxyhemoglobin will exhibit a long translational correlation time due to its slow translational diffusion. This makes deoxyhemoglobin relatively

ineffective at enhancing T_1 relaxation, and quite effective at decreasing T_2 . Although there is exchange of plasma water protons with intracellular protons, the red blood cell membrane limits this process to a significant extent (18). In fact, an accurate approximation of the T_2 of blood water protons can be made by a physical model that only considers the difference in the magnetic susceptibility between the red blood cell and the plasma (19). The difference in susceptibility between fully desaturated red blood cells and plasma is substantial and is approximately equal to 0.27 ppm, a value accurately estimated by Pauling in 1936 (16).

Although it is very difficult to develop a precise analytic expression for the transverse relaxation rate of blood as a function of oxygenation (20), there are accurate models based on simulations and experimental measurements. An accurate estimation of the transverse relaxation time can be made by the Monte Carlo simulation of plasma spin diffusion through the inhomogeneous magnetic fields around desaturated red blood cells (21). Briefly, such a simulation can be done as follows. First, a set of N desaturated red blood cells (assuming spherical shape) are randomly distributed in a three-dimensional space to give a volume fraction equal to hematocrit and the blood oxygen saturation level. Second, a single proton is placed at a random starting position. For every time step Δt , this proton is randomly displaced in the x , y , z dimension by a distance equivalent to the random sample of a normal distribution (mean equal to zero and standard deviation equal to the $\sqrt{(2D\Delta t)}$, where D is the proton diffusion coefficient).

Third, the magnetic field experienced by this proton at this location, ΔB_z , is determined by summing over the fields produced by all of the individual red blood cells according to:

$$\Delta B_z = \frac{4\pi}{3} \Delta\chi B_0 \sum_{i=1}^N \left(\frac{R}{r_i} \right)^3 (3\cos^2\theta_i - 1) \quad [1.7]$$

where r_i is the radial distance and θ_i is the azimuthal angle of the proton from the i th red blood cell. Fourth, the phase accumulated by the proton in this time interval is determined by the equation $\Delta\theta = \gamma\Delta B_z\Delta t$. Fifth, if there is an RF refocusing pulse(s) in the measurement, 180° is added to the phase at the point of refocusing pulse. Sixth, this process is repeated for the proton over a time scale allowing for sufficient relaxation decay. This will depend on the field strength, per Eq. [1.7]. Lastly, this process should be repeated for a sufficiently large number of protons ($\geq n=10,000$), and the phases of all proton vectors summed to give a signal at each time point. The resulting decay curve can be fitted to a monoexponential decay, $S=\exp(-t/T_2)$, to provide a value for T_2 . This process can be repeated for different hematocrit and oxygenation levels, as well as static magnetic field strengths. As illustrated by this model, the transverse relaxation rate will increase nonlinearly with the static field strength, because the phase accrual of spins in the same condition is directly proportional to the field strength.

In both simulations and direct experimental measurements, the transverse relaxation rate versus oxygenation is best described by a quadratic model (22-24):

$$R_2^{(*)} = A^{(*)}(1 - Y)^2 + B^{(*)}(1 - Y) + C^{(*)} \quad [1.8]$$

where Y is the blood oxygen saturation fraction (where 1 is fully saturated blood) and R_2 is $1/T_2$. R_2^* is the transverse relaxation rate with a component due to spin dephasing from macroscopic static field inhomogeneities, an effect which can be generally be eliminated with RF refocusing. Based on published empirical fits to the constants A , B , and C from *in vitro* experiments, we can determine the value of R_2 and R_2^* at arbitrary levels of blood oxygenation (22,23). Curves of R_2 versus venous oxygenation ($1-Y$) of blood are shown in Fig. 1.5. R_2^* shows similar trends in relaxivity to R_2 , but at higher relaxation rates.

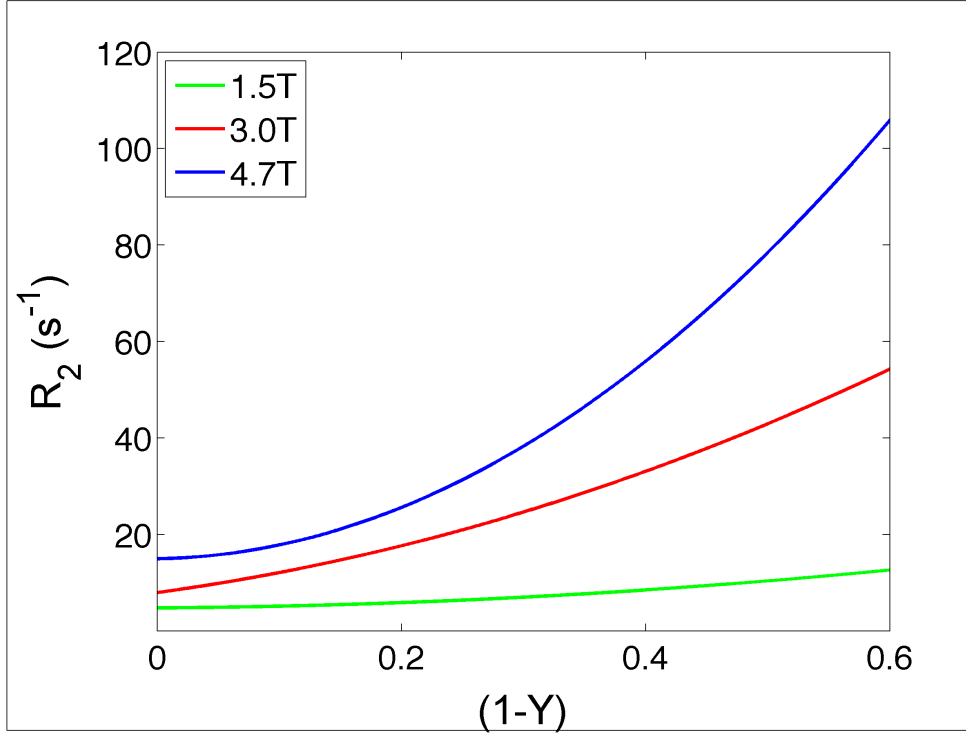


Figure 1.4. R_2 versus oxygen saturation (1-Y) at 1.5, 3, and 4.7 Tesla from Eq. [1.8] and literature values of constants A, B, and C.

The expected relaxivity in tissue from deoxyhemoglobin concentration changes is discussed in detail in Chapter 5. As discussed above, the R_2 modulation will depend on both the intra- and extravascular effects of local deoxyhemoglobin concentrations, which in turn depend on the tissue microstructure. Modeling these processes is much more difficult than for blood, as it depends on many tissue specific features including average vessel size, density, and spatial arrangement. In T_2^* -weighted images, the orientation of the sample in the magnetic field also has a substantial effect.

To approximate the scale of the *in vivo* relaxivity of deoxyhemoglobin in tissues, consider T_2^* -weighted images of the brain at 3T. If deoxyhemoglobin were to be completely diluted out, we would expect to see approximately a 5-9% signal change across the brain in T_2^* -weighted gradient-echo echo planar imaging (EPI) with an echo time of 32 ms (6). Since the change in venous oxygenation is smaller during hyperoxia, we typically expect to measure approximately a 1-2% signal change in the same setting. These changes are readily detectable with T_2 and T_2^* -weighted approaches such as echo planar and fast spin echo imaging that can produce per voxel signal-to-noise ratios greater than 100:1.

1.6 Relaxivity of Molecular Oxygen in Arterial Blood and Tissue

As discussed above in Section 1.3, the inhalation of hyperoxic gas mixtures dilutes the concentration of deoxyhemoglobin in the blood by dramatically increasing the concentration of dissolved oxygen in blood plasma. However, molecular oxygen is itself a paramagnetic molecule and will influence the relaxation behavior of blood. The effects of dissolved molecular oxygen on *in vivo* relaxation times are not as extensively studied as those for deoxyhemoglobin and other paramagnetic contrast agents, likely because substantial interest in hyperoxic contrast has only recently emerged. Understanding the influence of molecular oxygen on arterial blood is particularly important for quantitative studies of arterial spin labeling, as discussed in Chapters 3 and 4.

As discussed above in Section 1.4, small paramagnetic molecules contribute to proton relaxation in aqueous solutions by two distinct mechanisms, translational diffusion of the paramagnetic molecule and the proton interaction with the hydration sphere of the paramagnetic molecule (12). The effective correlation time will therefore involve the combination of the contributions of (i) the translational diffusion rate and (ii) the proton residence time in the hydration sphere or the electron T_1 , whichever is shorter (11,25). In the case of dissolved molecular oxygen, the spin exchange with the hydration sphere is extremely rapid, so the effective correlation time is the linear combination of the electron T_1 and translational diffusion rate (26). In water, the correlation time of translational diffusion and the electron T_1 are close in value, so both contribute significantly to the effective correlation time (27). However, the effective correlation time of oxygen is still very short in dilute aqueous solutions (26), making the contribution of oxygen to T_1 and T_2 small and equal (11). For a complete mathematical description of the effect of dissolved oxygen relaxation of water, we refer readers to the work of Mirhej (27), Parker and Harmon, (28), and Teng, et al. (26).

In Chapter 3, we measured the longitudinal relaxivity of molecular oxygen and determined that its plasma relaxivity is approximately $1.6 \times 10^{-4} \text{ s}^{-1} \text{ mm Hg}^{-1}$. This translates into a T_1 change in arterial blood at 3T of approximately 150 ms when breathing pure oxygen. If arterial blood makes up 5% of the measured signal in tissue, we expect a change in T_1 approaching 10 ms – a change that, although small, is readily

detectable by *in vivo* T_1 mapping approaches (29,30). Although not measured, we expect the transverse relaxivity of oxygen to be equal to its longitudinal relaxivity based on the arguments above. However, since the transverse relaxation time in body tissues is dominated by interactions with proteins, we do not expect dissolved oxygen to produce measurable changes to the linewidth *in vivo*.

The effect of inhaled oxygen on T_1 has been used in several studies to provide information about oxygen delivery and consumption in normal tissues and tumors (31-35). Although there have been qualitative attempts to explain the origin of this contrast, no attempts have been made to relate its T_1 relaxivity to blood flow, blood volume, and oxygen metabolism. We take up this task in Chapter 6, where we attempt to establish quantitative relationships between the change in T_1 during hyperoxia, tissue blood flow, and oxygen consumption.

1.7 Oxygen Gas and Bulk Static Magnetic Field Shifts

When a material is placed in magnetic field \mathbf{B} , a magnetization \mathbf{M} (magnetic moment per unit volume) is induced in the direction of \mathbf{B} if the material is paramagnetic. \mathbf{M} is induced opposite to \mathbf{B} if the material is diamagnetic. \mathbf{M} is directly proportional to \mathbf{B} :

$$\mathbf{M} = \kappa \cdot \mathbf{B} \quad [1.9]$$

where κ is the unitless volume susceptibility. Differences in magnetic susceptibility across samples induce static field inhomogeneities. The brain is near large air filled spaces, which have dramatically different magnetic susceptibility than tissue. Since there can be no instantaneous change in magnetic fields when crossing these large susceptibility differences (i.e., Maxwell's equations must be satisfied), large scale magnetic field inhomogeneities are created near these boundaries. The spatial extent and magnitude of these field inhomogeneities increase at stronger magnetic field strengths, since induced magnetic field differences in the air-filled spaces and tissues also increase.

Due to the paramagnetic and diamagnetic properties of oxygen and nitrogen gas, respectively, oxygen dominates the magnetic susceptibility of air. When the oxygen content of inhaled gases increases, bulk susceptibility of the inhaled gas is altered in a directly proportional manner. The volume magnetic susceptibilities of air and oxygen gas are opposite in sign and similar in magnitude to tissue; normal air is approximately 3.2×10^{-8} (cgs units) with pure oxygen gas having a susceptibility five times higher at 1.6×10^{-7} . A good approximation for tissue susceptibility is water, which is diamagnetic and has a volume susceptibility of -7.2×10^{-7} .

Although a complete physical model of the effect of oxygen gas in the upper airway on the static magnetic field requires solving Maxwell's equations as a partial differential

equation boundary problem, we can predict that the effects will be measurable based on the large changes in magnetic susceptibility of the gases. The effect of background magnetic field shifts is generally not considered in hyperoxic contrast studies of the human brain ((36-39)). However, it is quite possible this will have a significant effect on measured values, since gradient-echo echo planar imaging (EPI) approaches typically used in these studies are highly sensitive to local static magnetic field changes. For these reasons, we set out in Chapter 2 to further investigate the effect of hyperoxic gas inhalation on the static magnetic field of brain regions around the upper airway as a function of FiO_2 and static magnetic field strength.

1.8 Cerebral Oxygen Consumption, Blood Flow, and Volume During Hyperoxia

Beyond increasing SaO_2 and dissolved oxygen in the arterial blood, an increase in the fraction of inspired oxygen (FiO_2) is known to produce a multitude of detectable biochemical and physiological effects (40,41). These include altering the partial pressures of oxygen and carbon dioxide in tissues, changing the binding of carbon dioxide and oxygen with hemoglobin, as well as changing ventilation and cerebral blood flow (CBF) (42-45). Although the causes of such effects and their relationships are quite complex, it is not necessary to fully characterize all of the details of these physiological processes in order to use hyperoxia as a quantitative MRI contrast agent. What is essential is to fully characterize the effect of hyperoxia on physiological phenomena that affect the MR signal during a typical experiment. While hyperoxia produces detectable

effects on CBF, the magnitude and temporal characteristics of these changes is important for determining whether or not we can assume that brief oxygen inhalation periods are pure sources of image contrast with negligible effects on metabolism.

From prior studies, it has been established that oxygen produces a mild reduction in CBF (5,37,41,43,44,46,47). However, the degree of this reduction and its relationship to FiO_2 , as well as the mechanisms that contribute to it, remain controversial and uncertain (37). Increasing FiO_2 in humans is known to lower end tidal CO_2 , which results in arteriolar vasoconstriction and a reduction in CBF. However, oxygen itself also exhibits a vasoconstrictive effect that is independent of end tidal CO_2 (48,49). This vasoconstrictive mechanism of oxygen is unclear, but likely stems from lower nitric oxide activity (50,51). Although the temporal response characteristics of these effects are also different, they are expected to exhibit reproducible dose-dependent responses in most physiologic conditions.

Although it has been established that hyperoxia can mildly lower CBF, studies have shown that hyperoxia has little to no effect on CBV, even at a $\text{FiO}_2 = 1.0$ (6,49,52). Additionally, arterial hypocapnia has been shown to produce minimal effects on the arterial cerebral blood volume (53). Similarly, hyperoxia has been shown to have no effect on the resting cerebral metabolic rate of oxygen (CMRO_2), even with pure normobaric hyperoxia (5). However, it is important to note that direct measures of

CMRO₂ changes are difficult to perform, and therefore such changes during hyperoxia are difficult to rule out. This assumption would best be tested by glucose uptake PET studies or ¹⁷O₂ inhalation MRI studies, yet these have not yet been performed. Nevertheless, the lack of evidence to the contrary, despite many studies in this area, is a good indicator that significant changes in oxygen metabolism during hyperoxia are unlikely. Since metabolic and CBV changes are likely to contribute very minimally to MR signal during hyperoxic inhalation, the main physiological parameter that is important is CBF. Hence, if we can characterize the induced temporal changes of CBF in a dose-dependent manner during hyperoxia, we can correct for its effects on the MR signal.

1.9 Safety of Inhalation of Hyperoxic Gas Mixtures

Oxygen begins to exhibit toxic effects at a FiO₂ ≥ 0.5 or 50 kPa. Fortunately, most non-severe forms of oxygen toxicity are well tolerated. Oxygen toxicity has its biochemical basis in the partial reduction of oxygen by one or two electrons to form reactive oxygen species (ROS), including the superoxide anion (O₂⁻) and the hydroxyl radical (·OH). Increasing the partial pressure of oxygen in tissue with hyperoxia also increases ROS concentrations in these tissues (54). All the pathogenic mechanisms of these reactive species are not fully understood (55), but they are known to create damage to cellular membranes and DNA (56). The body employs antioxidant systems, such as glutathione, that can neutralize the effects of ROS in tissues (57). However, these defenses are

overwhelmed at sufficiently high concentrations of reactive species, leading to cellular damage and potential tissue necrosis (58).

The effects of oxygen toxicity may be classified by the affected organs, namely the central nervous system, the pulmonary system, or the ocular system. Central nervous system toxicity is characterized by convulsions and loss of consciousness. This is the most severe form of oxygen toxicity, but it almost always occurs under hyperbaric oxygen exposure (>100 kPa). Pulmonary toxicity is characterized by difficulty breathing and chest pain, which can occur when breathing normobaric or hyperbaric oxygen. However, this is typically experienced after prolonged exposure times on the order of several hours to days. Ocular toxicity is characterized by damage to the lens of the eye, which can lead to myopia or retinal damage causing detachment. Ocular damage can also occur with normobaric or hyperbaric oxygen exposure, but it is also typically due to chronic exposure on the order of many hours to days.

Only hyperbaric oxygen exposure generally leads to cerebral and ocular clinical manifestations. Exposures as short as a few minutes to partial pressures of oxygen greater than 160 kPa (eight times the atmospheric pressure of 21 kPa) can cause central nervous system toxicity. While the exact mechanism for central nervous system toxicity during hyperoxia remains unclear (59,60), it is likely related to the uncontrolled formation of ROS in the brain (56). In adults, ocular damage occurs primarily through

damage to the lens. Hyperoxic myopia has been shown to occur in close circuit scuba diving and in those undergoing repeated hyperbaric oxygen therapy (61). The mechanism is an increase in the refractive power of the lens, which is usually reversible with time.

Since the lungs and respiratory tract are exposed to the highest concentrations of oxygen during hyperoxia, they are the first areas to show effects of oxygen toxicity. Normobaric levels of oxygen can cause acute lung damage, beginning with tracheobronchitis or inflamed upper airways, experienced 4 to 22 hours after exposure to pure normobaric oxygen after an asymptomatic period (62). At hyperbaric levels of 200-300 kPa, these effects may begin as soon as 3 hours after oxygen exposure. Small animal experiments indicate that a decline in lung function can occur as soon as 24 hours after continuous 100% oxygen exposure (63). Diffuse alveolar damage and acute respiratory distress syndrome can develop after 48 hours at $\text{FiO}_2 = 1.0$ (62). Alveolar collapse, known as atelectasis, can also be induced by hyperoxia and occurs rapidly during 100% oxygen inhalation. In this context, known specifically as absorption atelectasis, as oxygen replaces nitrogen in the alveoli it is absorbed into the blood rapidly, decreasing alveolar volume and causing alveolar collapse. High partial pressures of oxygen balanced by nitrogen (i.e., hyperbaric gas) avoid this scenario (62).

Adult populations that are particularly at risk for oxygen toxicity are those that have been treated with the chemotherapeutic agent bleomycin or those with chronic obstructive pulmonary disease. Bleomycin exposure can greatly increase the effects of pulmonary oxygen toxicity through the role of proinflammatory cytokines IL-18 and IL-1beta (64). Any hyperoxic exposures should be avoided in these patients. Patients with chronic obstructive pulmonary disease can experience a clinical condition called carbon dioxide narcosis when inhaling hyperoxic gas mixtures. Carbon dioxide narcosis is caused by excessive CO₂ retention, and can be at least in part attributed to a reduction in normal ventilation-perfusion matching and a reduction in hypoxic drive (62). Hyperoxia can lead to dangerously high levels of CO₂ in these patients and its administration should generally be avoided.

In summary, although oxygen is not entirely devoid of toxicity and contraindications, most of the danger occurs either at high levels of oxygen exposure (>160 kPa) for short periods of time or moderate levels (>50 kPa) for long durations. Therefore, most adverse effects can be avoided by reducing oxygen concentration to minimal levels (FiO₂ < 1.0) and limiting exposure durations. In our studies, the maximum oxygen exposure was 100% oxygen for ten minutes, which is generally considered to be very safe and we also avoided any adverse events in our healthy adult subjects.

1.10 Current Applications of Hyperoxic MRI Contrast

There has been emerging research and clinical interest in using oxygen as an intravascular MRI contrast agent because of a number of attractive features, including its wide availability, negligible cost, high tolerability, lack of contraindications, minimal physiologic effects, and rapid wash-in and wash-out times. Most of the studies on hyperoxic contrast have focused on using oxygen to create an isometabolic dilution of deoxyhemoglobin and have used T_2 - and T_2^* -weighted imaging approaches to measure this effect. Some of the main techniques that have been developed using this effect are calibrated simultaneous BOLD/ASL measurement of the relative cerebral metabolic rate of oxygen (as an alternative to carbon dioxide) (6,38,39), measurements of regional capillary-venous cerebral blood volume (36), the characterization of the ischemic penumbra of stroke lesions including its oxygen consumption and spatial extent (65-68), and the delineation of hypoxic regions in tumors (31,69).

Other techniques have focused on the other contrast mechanism of hyperoxia, the measurement of T_1 reduction from the delivery of excess oxygen to tissues as an indicator of baseline tissue oxygenation. Although increases in dissolved oxygen are fairly small, many have been successful in measuring these longitudinal relaxation changes using T_1 -weighted gradient echo and Look-Locker techniques. These studies include: measuring relative baseline tumor oxygenation (31,33), oxygen delivery and consumption in skeletal

muscle (70), lung ventilation (29), and oxygen delivery to physiologic fluids including the CSF and vitreous humor (71).

1.11 Summary of Technical Challenges in Using Hyperoxia as a Quantitative

Intravascular Contrast Agent

Although progress has been made toward the use of hyperoxia as a quantitative intravascular contrast agent, several technical challenges remain. First, the effect of bulk oxygen gas on background field inhomogeneities in typical BOLD-modulated studies of the human brain using gradient echo EPI has not been explored. We expect that the fields are likely to change substantially in the frontal lobes near the frontal sinus and oral cavity, due to the large changes in volume susceptibility between air and pure oxygen gas. Second, although there have been numerous studies regarding the effects of oxygen on regional CBF using ASL, they do not correct for the effect of T_1 changes in arterial blood plasma. Furthermore, the temporal effects of CBF change as a function of oxygen exposure duration have also not been studied in detail. Knowledge of these effects is crucial for any measurement using ASL and hyperoxia simultaneously, particularly for BOLD/ASL calibrated studies where flow changes significantly affect the calibration. Third, the use of hyperoxia calibration studies of relative changes in $CMRO_2$ has not been validated against absolute quantitative measurements of $CMRO_2$. It is unclear to what extent these techniques contain sources of errors in their model assumptions, which can only be determined by comparing them to a gold standard. Fourth, although there

have been various studies using the longitudinal relaxation enhancement of molecular oxygen to study oxygen delivery and consumption, there have been no attempts to quantitatively model the effect of T_1 on local tissue blood flow and metabolism. If these techniques are to provide quantitative information concerning the physiological status of the tissue, it will be crucial to understand these relationships.

1.12 Specific Aims of Thesis Research

Several technical issues remain concerning the use of hyperoxia as a quantitative intravascular contrast agent. Hence, the focus of this thesis is to address some of these important issues, namely to: (1) characterize the paramagnetic effects of molecular oxygen BOLD and arterial spin labeling (ASL) data, (2) determine the degree and temporal characteristics of hyperoxia-induced reductions in cerebral blood flow (CBF), (3) investigate the use of oxygen in quantitative measurements of metabolism, and (4) elucidate the biophysical mechanisms of hyperoxic T_1 contrast. It is towards these goals that we present the following specific aims:

1.12.1 Aim 1: Characterize the effects of molecular oxygen on BOLD-modulated hyperoxic contrast studies

Standard approaches to measuring BOLD-modulated hyperoxic contrast in the brain, including gradient echo EPI and other T_2^* -weighted approaches, are highly sensitive to

changes in the background static magnetic fields. There have been no attempts in the literature to establish whether or not field changes induced by bulk changes in the oxygen concentration of the upper airway near the brain can affect the background field to cause detectable changes in measured signals. Chapter 2 aims to characterize these effects as a function of field strength and FiO_2 .

1.12.2 Aim 2: Determine the change in longitudinal relaxation time of arterial blood at arbitrary levels of hyperoxia in vivo

Although ASL techniques are very sensitive to T_1 of arterial blood, there have been no studies that attempt to develop an accurate model of arterial blood T_1 measurements as a function of hyperoxia. Toward this end, we set out to produce such a model by making *in vitro* and *in vivo* measurements of the longitudinal relaxivity versus arterial partial pressure of oxygen. The work in Chapter 3 represents our work toward developing a complete quantitative model of the longitudinal relaxation time of arterial blood that depends only on knowledge of the partial pressure of arterial blood at a given FiO_2 .

1.12.3 Aim 3: Quantify absolute cerebral blood flow during hyperoxia using arterial spin labeling

Since ASL is quite sensitive to the T_1 of arterial blood, a quantification of absolute cerebral blood flow during hyperoxia requires knowledge of arterial blood T_1 as a function of arterial oxygen concentration. To date, there have been no published studies

using *in vivo* measurements of T_1 for arterial blood to correct ASL data. In an attempt to characterize the effect of this variable on measures of CBF, we made simultaneous *in vivo* measurements of T_{1a} and CBF during normoxia and hyperoxia under a brief hyperoxic inhalation, as well as graded hyperoxic inhalation paradigms on a per subject basis. This work is the focus of Chapter 4.

1.12.4 Aim 4: Implement hyperoxic gas calibration BOLD/ASL measurements of relative cerebral metabolic rate of oxygen using a hypermetabolic animal

The focus of this aim is to quantify metabolic changes using hyperoxic calibrated BOLD/ASL fMRI in a hypermetabolic swine model. Metabolic changes in this animal model were previously studied by our group using gas isotopically-enriched with $^{17}\text{O}_2$. The goal of this study is to cross-validate these absolute metabolic measurements with the deoxyhemoglobin dilution methods of relative metabolism, as well as to compare the results of hyperoxia and hypercapnia calibrations. This work is detailed in Chapter 5.

1.12.5 Aim 5: Develop a biophysical model of the dependence of cerebral blood flow and metabolism on hyperoxia-induced changes in the longitudinal relaxation rate of tissue

There have been several studies published regarding the effect of elevated partial pressures of oxygen in the arterial blood on longitudinal relaxation time in normal and diseased tissue, mostly using tumor models. While these studies show promising contrast

from the reduction in T_1 , indicating an increase in partial pressure of oxygen in these tissue regions, a quantitative understanding of this contrast mechanism has yet to be developed. Chapter 6 represents an attempt to establish a quantitative understanding of the relationship between cerebral blood flow, oxygen consumption, and the longitudinal relaxivity of hyperoxic contrast.

Chapter 2: Characterization of the Paramagnetic Effects of Molecular Oxygen on Blood Oxygenation Level-Dependent-Modulated Hyperoxic Contrast Studies

2.1 Overview

In hyperoxic contrast studies modulated by the blood oxygenation level-dependent (BOLD) effect, it is often assumed that hyperoxia is a purely intravascular, positive contrast agent in T_2^* -weighted images, and that the effects not due to BOLD contrast are small enough to be ignored. In this chapter, this assumption is reevaluated and non-BOLD effects in T_2^* -weighted hyperoxic contrast studies of the human brain were characterized. We observed significant negative signal changes in T_2^* -weighted images in the frontal lobes; B_0 maps suggest this effect was primarily due to increased intravoxel dephasing from increased static field inhomogeneity due to susceptibility changes from oxygen in and around the upper airway. These static field effects were shown to scale with magnetic field strength. Signal changes observed around the brain periphery and in the ventricles suggest the effect of image distortions from oxygen-induced bulk B_0 shifts, along with a possible contribution from decreased T_2^* due to oxygen dissolved in the cerebrospinal fluid. Reducing the concentration of inhaled oxygen was shown to mitigate negative contrast of molecular oxygen due to these effects, while still maintaining sufficient BOLD contrast to produce accurate measurements of cerebral blood volume. This results of this work serve to outline limits in which studies of the human brain using

hyperoxic T_2^* contrast can be considered to avoid the artifactual effects of paramagnetic oxygen and be entirely due to deoxyhemoglobin dilution.

2.2 Introduction

As discussed above in Chapter 1, the inhalation of hyperoxic gas mixtures is known to be an effective positive contrast agent in T_2^* -weighted images (53,72). To summarize the process again briefly, an elevated inspired fraction of oxygen (FiO_2) causes excess molecular oxygen to dissolve in the blood plasma in the lungs. The excess oxygen in the plasma is then delivered to capillaries, where it diffuses into the tissues preferentially to the oxygen bound to hemoglobin. The deoxy-/oxyhemoglobin ratio and the paramagnetism of the blood (blood oxygenation level-dependent, or BOLD, effect) are subsequently decreased, resulting in an increase in signal on T_2^* -weighted images. The T_2^* contrast generated in a given voxel is dependent on the capillary-venous blood volume in that voxel and the degree to which the concentration of deoxyhemoglobin changes in the capillary-venous blood (72).

For oxygen to be considered as a purely intravascular contrast agent in T_2^* -weighted images, it must have minimal effects on the MR signal that are not due to the dilution of deoxyhemoglobin. As covered in Chapter 1, molecular oxygen dissolved in the blood has a detectable T_1 relaxivity (73), and molecular oxygen has been shown to be effective

as a T_1 contrast agent in body fluids (71,74), displaying a fast wash-in of a significant concentration of molecular oxygen into these tissues. Unless T_1 -weighting is completely eliminated by the imaging sequence approach, it could present a possible confounding factor in these studies.

Another important effect is the disruption of the static magnetic field (B_0) in the frontal lobes of the brain due to the influence of paramagnetic gaseous oxygen in the upper airway. This effect has not yet been characterized or considered in hyperoxic contrast studies of the human brain (6,38). The physical argument for this effect was covered in Chapter 1. To summarize, gaseous nitrogen is diamagnetic, while gaseous oxygen is weakly paramagnetic. However, since the magnetic susceptibility of gaseous oxygen is more than 300 times that of gaseous nitrogen (75), the magnetic properties of air are dominated by oxygen. The volume magnetic susceptibility of air and of oxygen are therefore approximately equal in value and opposite in sign. The inhalation of $FiO_2 = 1.0$ will make the frontal sinuses approximately five times more paramagnetic than air, further increasing the difference in magnetic susceptibility at the air-tissue interface. This will substantially increase the static field inhomogeneity in surrounding brain regions, leading to decreased signal in T_2^* -weighted images, distortions in echo-planar imaging (EPI) acquisitions, and shifts in slice locations.

In this study, the paramagnetic effects of molecular oxygen on typical BOLD-modulated T_2^* -weighted gradient echo EPI studies in the human brain have been characterized. The degree of negative contrast in tissue specific compartments and regions was also examined. The effects of inhaled oxygen on the static field were characterized by the measurement of the difference in B_0 maps during normoxia and hyperoxia at 3T and 7T field strengths. We have shown that the degree of static field inhomogeneity increases with inhaled oxygen concentration and with increasing field strength. Furthermore, we demonstrate that a reduction in the concentration of inhaled oxygen significantly reduced non-BOLD T_2^* signal changes, while maintaining adequately high contrast-to-noise from the BOLD effect for accurate CBV calculation.

2.3 Materials and Methods

2.3.1 Gas Delivery and MRI Hardware

All experiments involving humans subjects were done under protocols approved by our Institutional Review Board, and signed, informed consent was obtained from each volunteer. All images were collected on a whole-body clinical 3T MRI scanner (Siemens Trio; Siemens Healthcare, Erlangen, Germany) with a body coil transmitter and 8-channel receiver head coil, except for one dataset collected on a whole-body 7T system (Siemens Magnetom) with a transmit-receive circularly-polarized head coil. For all experiments, medical air, oxygen, or hyperoxic mixtures were delivered to the subject with a nonrebreathing mask fitted tightly over the nose and chin, running at a flow rate of

40 L/min from an air/oxygen blending device capable of delivering precise FiO_2 values of 0.21-1.0 at high flow rates (Precision Medical Inc, Northampton, PA, Model PM5300). A high flow rate was used to ensure that normal resting maximum peak inspiratory flow rates were exceeded (76), thus eliminating any entrainment of room air upon inhalation. The magnet bore fan was run at maximum to ensure that gases did not build up around the subject.

2.3.2 Hyperoxic Challenge Paradigm

For all hyperoxic challenge experiments, a baseline – stimulation – rest paradigm was used. To examine the positive and negative contrast effects across the brain, an experimental paradigm lasting twenty-seven minutes was performed on one normal, healthy male volunteer (28 years old). A baseline three-minute period of normoxia ($\text{FiO}_2 = 0.21$) was followed by two cycles of a six-minute hyperoxic stimulation period $\text{FiO}_2 = 1.0$ and six-minute rest period of $\text{FiO}_2 = 0.21$.

2.3.3 MRI Sequence Parameters

During the experiment, continuous whole-brain echo-planar imaging (EPI) data were collected with the following sequence parameters: FOV: 220 x 220 mm, 128 x 128 matrix, TE/TR: 29/2000 ms, 22 slices, slice thickness: 5 mm, 1 mm slice gap, FA: 90° . In addition to the EPI acquisitions, a high-resolution structural T_1 -weighted MP-RAGE scan with 1 x 1 x 1 mm³ voxel size and a whole-brain dual-echo 3D GRE with phase

reconstruction and $2 \times 2 \times 2 \text{ mm}^3$ voxel size (for B_0 mapping) were performed at the beginning of the experiment to allow for unwarping, structural coregistration, and tissue segmentation of the EPI data. To characterize the positive and negative contrast effects as a function of the level of hyperoxia, the same whole-brain EPI data, structural images, and B_0 maps were collected on a set of normal, healthy volunteers ($N=6$, three male subjects, age range 28-32 years). All subjects were imaged with experimental paradigm lasting 27 minutes similar to the one above, except two different FiO_2 levels were used. In this case, a baseline three-minute period of normoxia ($\text{FiO}_2 = 0.21$) was followed by a six-minute mild hyperoxic stimulation period of $\text{FiO}_2 = 0.5$, a six-minute rest period of $\text{FiO}_2 = 0.21$, a six-minute hyperoxic stimulation period of $\text{FiO}_2 = 1.0$, and a second six-minute rest period of $\text{FiO}_2 = 0.21$.

To characterize changes in B_0 occurring as a function of the level of hyperoxia, the same experimental paradigm was performed again while sagittally-oriented whole-brain continuous dual-echo 3D GRE phase images were acquired for three of the six subjects following the final normoxic rest period. The sequence parameters were: FOV: $256 \times 256 \times 160 \text{ mm}$, $128 \times 128 \times 80$ matrix, $\text{TE}_1/\text{TE}_2/\text{TR}$: 3/7/12 ms, 6/8 partial Fourier factor (phase and slice), and FA: 7° . The total acquisition time of each 3D GRE image was 72 seconds, allowing five whole-brain B_0 maps to be acquired during each stimulation and rest period. To characterize changes in B_0 during hyperoxia as a function of the static

field strength, this same B_0 mapping experiment at different FiO_2 levels was performed at 7T for one of these subjects.

2.3.4 Data Analysis

All data were processed using the FMRIB Software Library (FSL) Tools (77). The EPI data were motion corrected and unwrapped using a software package designed to process intramodal MRI time series data (FEAT) (78). Each phase image was unwrapped separately using an automatic phase unwrapping algorithm (PRELUDE) (77). The structural images were segmented into masks of three tissue types – CSF, gray matter, and white matter – using an automatic tissue segmentation algorithm (FAST) (79). The structural images and their respective masks were co-registered to the EPI data using an automatic affine registration algorithm (FLIRT) (80). This tool was also used for motion correction of the series B_0 maps by co-registering all magnitude volumes and applying the affine matrix to the phase data.

Final analysis of all the datasets was performed using custom scripts written in MATLAB (MathWorks, Inc.). All statistical tests used the Student's paired t-test; all reported values and error bars on plots were in mean \pm SD. For each six minute epoch of each dataset, the EPI data from the first three minutes or the first two B_0 maps were discarded to allow the intravascular levels of oxygen to reach a steady state (37). For the first experiment described, data from all normoxia and hyperoxia epochs were averaged and compared. For the experiment comparing elevated FiO_2 levels, the baseline values of the first

hyperoxic epoch were obtained from the mean of the first and second normoxia epochs, and, in the same manner, the second and third were used for the second hyperoxic epoch. This was done to mitigate signal drift effects. The unwrapped phase datasets were subtracted and divided by the echo time difference and converted to relative B_0 maps in ppm. The coregistered tissue segmentation masks were multiplied by the unwrapped EPI data to obtain values for CSF, gray matter, and white matter regions across the brain.

2.3.5 Calculation of Regional Cerebral Blood Volume

Regional capillary-venous CBV values were calculated according to the method from Bulte, et al. (36), whereby the signal enhancement in tissue is normalized to the signal from a pure vein voxel:

$$CBV = \frac{h}{n\rho} \sum_{j=0}^n \frac{\ln\left(\frac{S_{tissue}(j)}{S_{tissue,0}}\right)}{\ln\left(\frac{S_{vein}(j)}{S_{vein,0}}\right)} \quad [3.1]$$

where n is the number of signal voxel ratios measured after reaching the steady state; $h=(1 - Hct) / (1 - 0.85 \times Hct)$ accounts for the difference in the hematocrit between the large and small vessels; $\rho = 1.04 \text{ ml/g}$ is the tissue density; $S_{tissue,j}$ and $S_{vein,j}$ are the signal measurements made in tissue voxels and a pure vein voxel during hyperoxia; $S_{tissue,0}$ and $S_{vein,0}$ are the baseline signals from each tissue voxel and a pure vein voxel.

2.4 Localization of Hyperoxia-Induced Positive and Negative EPI Signal Changes

Figure 2.1 provides an example of typical positive (Fig. 2.1b) and negative (Fig. 2.1c) percent signal change from baseline with 100% oxygen inhalation, along with coregistered structural images. Positive contrast can be seen across gray matter, with large veins showing the most contrast. Well-defined regions of negative signal change can be seen in regions around the frontal sinus as well as in superior slices, but do not seem to be associated with a particular tissue compartment. Coherent negative contrast is clearly visualized in the ventricles and large sulci, i.e. specific tissue compartments known to contain CSF (compare visually to segmentation of CSF in Fig. 2.3, below). Figure 2.1d shows the clear negative modulation upon oxygen inhalation of the signal in voxels near the frontal sinuses and in the CSF.

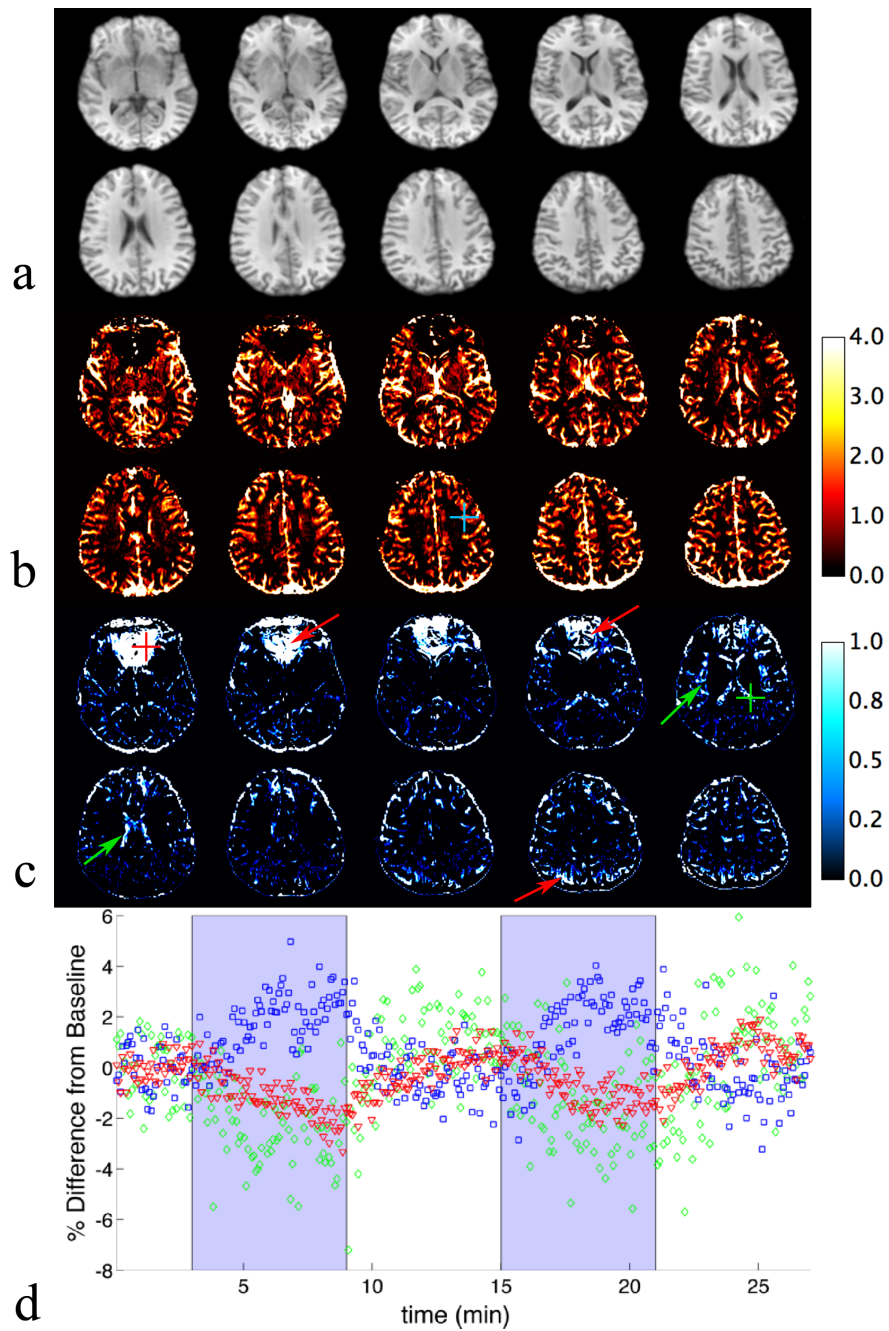


Figure. 2.1. Percent signal change from baseline upon $\text{FiO}_2=1.0$. Both positive (b) and negative (c) percent signal changes from baseline occur coherently in specific compartments of the brain, shown clearly in the coregistered MP-RAGE images (a).

The red arrows point to the negative T_2^* -contrast effect of the disruption of the B_0 field in the frontal lobes from gaseous oxygen in the sinuses and nasal cavity, along with associated long range static field disruptions in superior-posterior parietal lobes. The green arrows illustrate the effects of the reduction in transverse relaxation times from dissolved molecular oxygen in the CSF; major ventricles and sulci are clearly outlined in the negative signal change images. Voxels at the blue, red, and green crosses represent tissue, B_0 -affected, and CSF regions, respectively; signal values at these voxels are plotted as percent difference from baseline versus time at the blue squares (tissue), red triangles (B_0 -affected), and green diamonds (CSF) (d). The blue regions represent the two 100% oxygen inhalation epochs. The values of the B_0 -affected voxel have been scaled down by a factor of 0.1 for clarity.

2.5 Hyperoxia-Induced Negative EPI Signal Changes versus FiO_2

Figure 2.2b, c shows the percent negative contrast from baseline upon inhalation of $FiO_2 = 1.0$ and 0.5 , respectively, from five contiguous slices chosen to cover the ventricles and the frontal lobe regions just superior to the frontal sinus and nasal cavity. The signal intensities in these images are scaled in the same manner. In addition to substantial negative contrast centered around the frontal lobes and regions of high CSF, there are significant (although less coherent) negative signal changes across the brain in white and gray matter. A distinct reduction in the negative contrast is visualized in all regions at the lower FiO_2 level. Figure 2.3 shows a representative slice of coregistered tissue

segmentation masks from each tissue type along with the associated EPI slice. As shown, the high T_1 contrast between these tissue types allows robust segmentation.

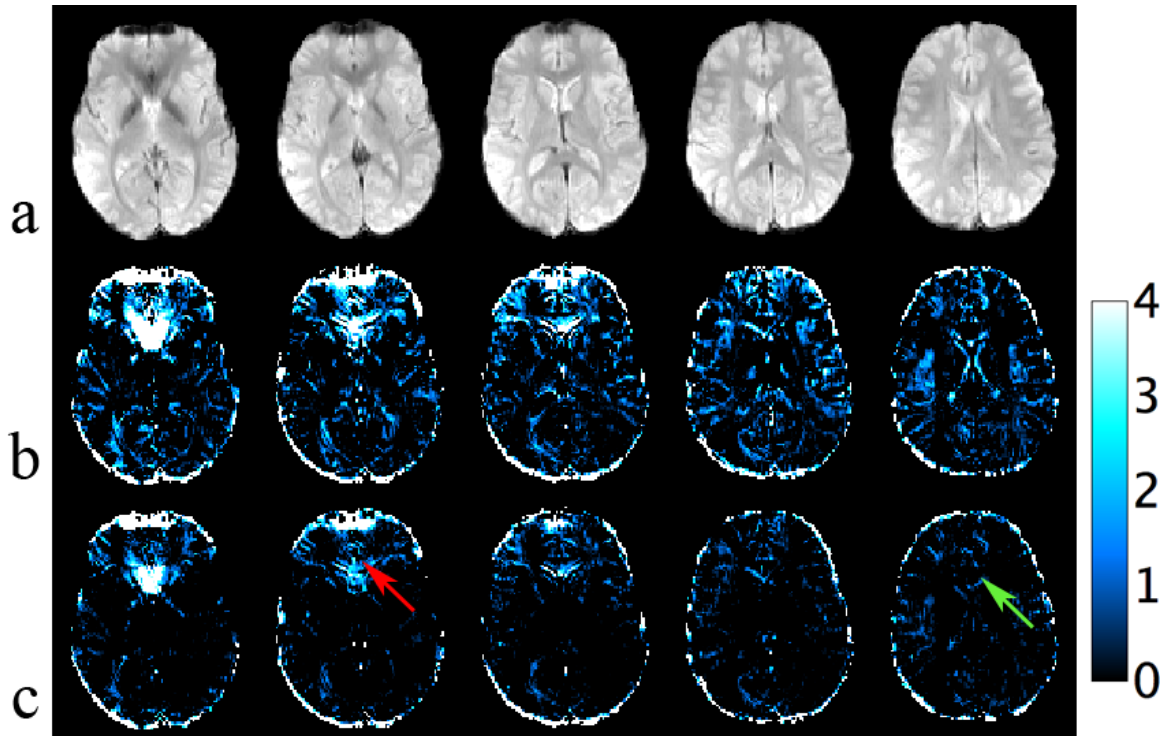


Figure 2.2. Comparison of percent negative signal change from baseline for $FiO_2 = 1.0$ (b) and 0.5 (c) with their associated EPI images (a). Note the significant reduction in negative contrast across the brain, particularly in the frontal lobe regions (red arrow) and in the ventricles and major sulci (green arrow).

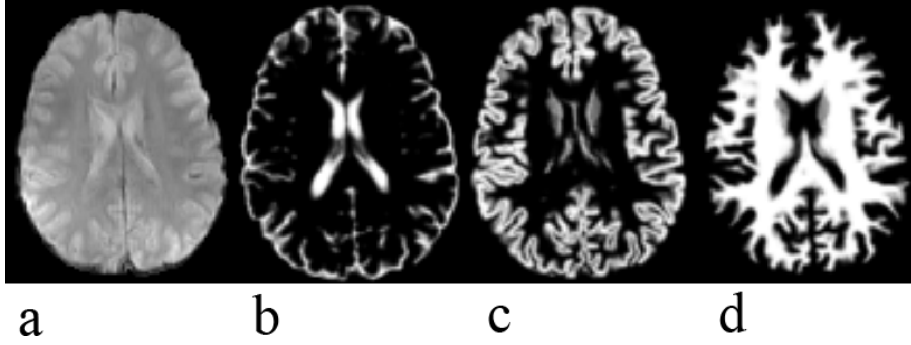


Figure 2.3. Tissue masks of cerebrospinal fluid (b), gray matter (c), and white matter (d) with a registered, unwarped EPI image (a). Tissue segmentation was performed using an automated tissue segmentation algorithm with a high resolution T_1 -weighted image. The tissue masks were then registered to unwarped EPI data with an automatic affine registration algorithm.

2.6 Measurement of Hyperoxia-Induced B_0 field Perturbation versus FiO_2

Figure 2.4 shows results from the subject imaged at 3T and 7T field strengths. Figure 2.4a shows a sagittal cut from 3D relative B_0 maps in parts-per-million (ppm) at baseline at 3T and 7T. The difference in the relative B_0 maps between the hyperoxic states at 3T and 7T is shown in Fig. 2.4b,c. In the frontal lobes near the nasal cavity, more than 0.1 ppm increase in the B_0 field was observed during 100% oxygen inhalation at 3T. Similar changes in the B_0 field were measured at 3T in the other two subjects (data not shown). In the dataset shown, additional static field changes were observed during $FiO_2 = 1.0$ in superior, posterior, and inferior brain regions far from the nasal cavity (Fig. 4b, top). Negative signal changes were observed in the EPI acquisitions in the same subject (Fig.

1c) near these same superior and posterior brain regions showing these additional static field changes. However, these static field effects were not observed in all subjects. During 100% oxygen inhalation at 7T, a large region of more than 0.1 ppm increase in the static field extends past the frontal lobes into the parietal and temporal lobes. At each field strength, these effects remain present during 50% oxygen inhalation, but to a much lesser extent (Fig. 4c). The relative change in the static field at different oxygen levels and field strengths is shown in Fig. 2.4d,e as a change in the normalized relative B_0 . This shows that the B_0 values superior to the nasal and oral cavities changed approximately twice as much in $FiO_2 = 1.0$ versus 0.5 at each field strength, and that relative B_0 changes are approximately twice as high at 7T versus 3T. It should be noted, however, that the results shown here are not from a representative subject, but rather from the one subject tested at both field strengths. Table 2.1 quantifies the negative contrast in each tissue type for all ($N = 6$) subjects as the mean percent of the total voxels in that region that show a negative (< 0) percent change from baseline. Statistically significant reductions in the percent of negative voxels for all tissue types are produced at the lower FiO_2 level, with an average overall reduction of 14.1%.

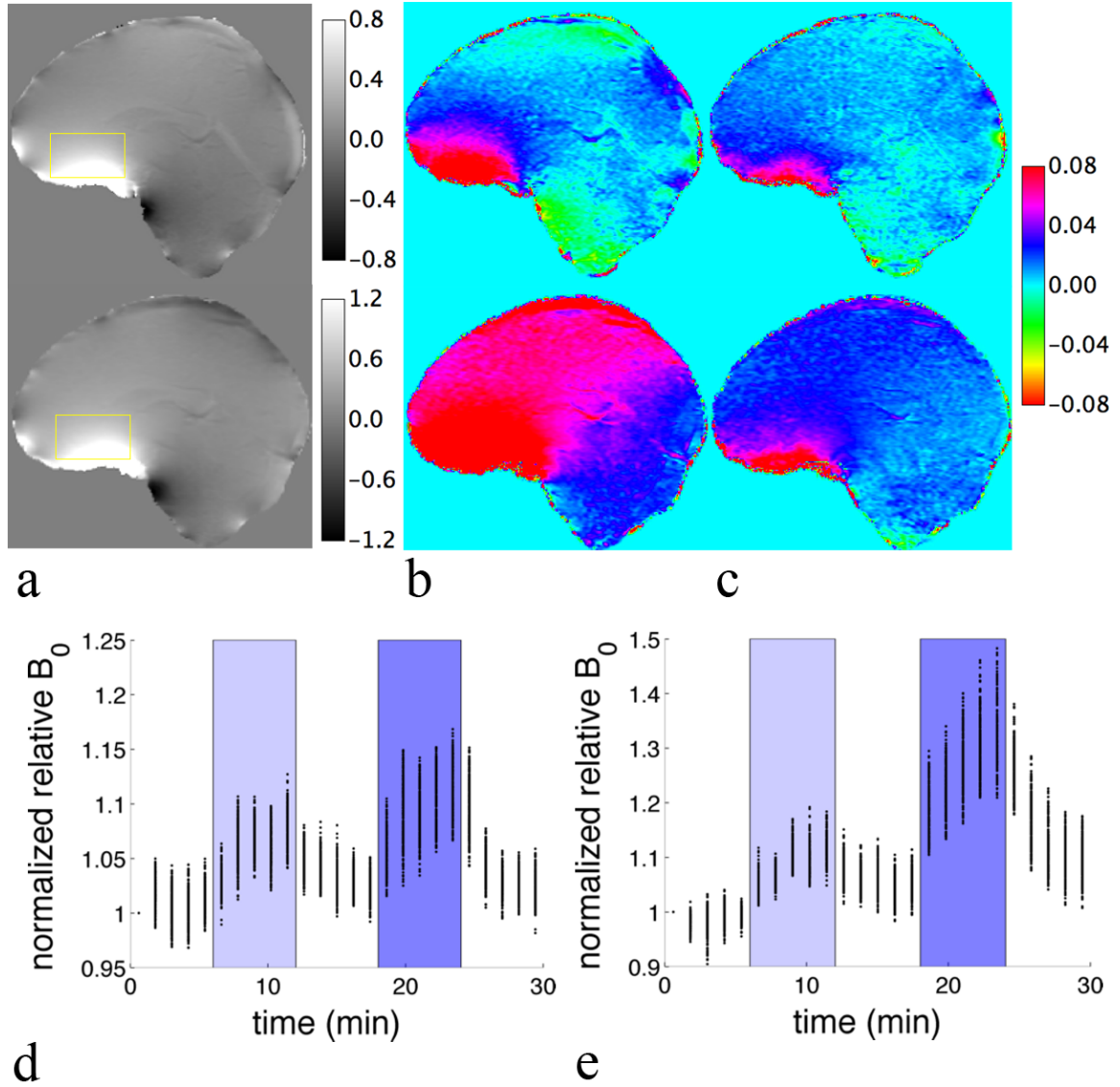


Figure 2.4. Baseline B_0 maps and change in B_0 after different levels of oxygen inhalation at 3T and 7T. Baseline relative B_0 maps (ppm) (a) during air breathing at 3T (top row) and 7T (bottom row). Change in the relative ΔB_0 (ppm) maps from baseline during $FiO_2 = 1.0$ (b) and 0.5 (c) at 3T (top row) and 7T (bottom row). Note that the effects of the static field extend beyond the frontal lobe region at both field strengths. The yellow boxes in the top and bottom rows of (a) mark rectangular regions of interest that are plotted in (d) and (e), respectively, as normalized relative B_0 values versus time for $FiO_2 = 0.5$ oxygen (light blue region) and 1.0 (dark blue

region) epochs. Normalized B_0 values are normalized voxel-by-voxel division of every B_0 map by the value of the first B_0 map. Note the substantially larger static field disruptions at 7T.

Table 2.1. Mean Percent Negative Voxels for All Subjects within Specified Tissue Regions for $\text{FiO}_2=1.0$ and 0.5

	$\text{FiO}_2=1.0$	$\text{FiO}_2=0.5$	p-value
CSF	36.5 ± 5.3	$24.1 \pm 3.4^*$	<0.001
White Matter	41.2 ± 7.9	$25.0 \pm 3.4^*$	<0.002
Gray Matter	26.4 ± 6.0	$12.9 \pm 2.3^*$	<0.01
All Regions	34.7 ± 7.6	$20.6 \pm 8.8^*$	<0.001

2.7 CBV Measurement Accuracy at Low FiO_2

Figure 5a,b demonstrates that the BOLD contrast is lower in $\text{FiO}_2 = 0.5$, but the final values of CBV computed in Figure 5c,d are very close to those calculated $\text{FiO}_2 = 1.0$. The values in Table 2.2 confirm this, with the mean global CBV values at $\text{FiO}_2 = 0.5$ being somewhat higher than those at $\text{FiO}_2 = 1.0$, although this difference was not found to be statistically significant. The values of CBV in gray matter and white matter measured here are in close agreement with those found in the previous implementation of this technique (36).

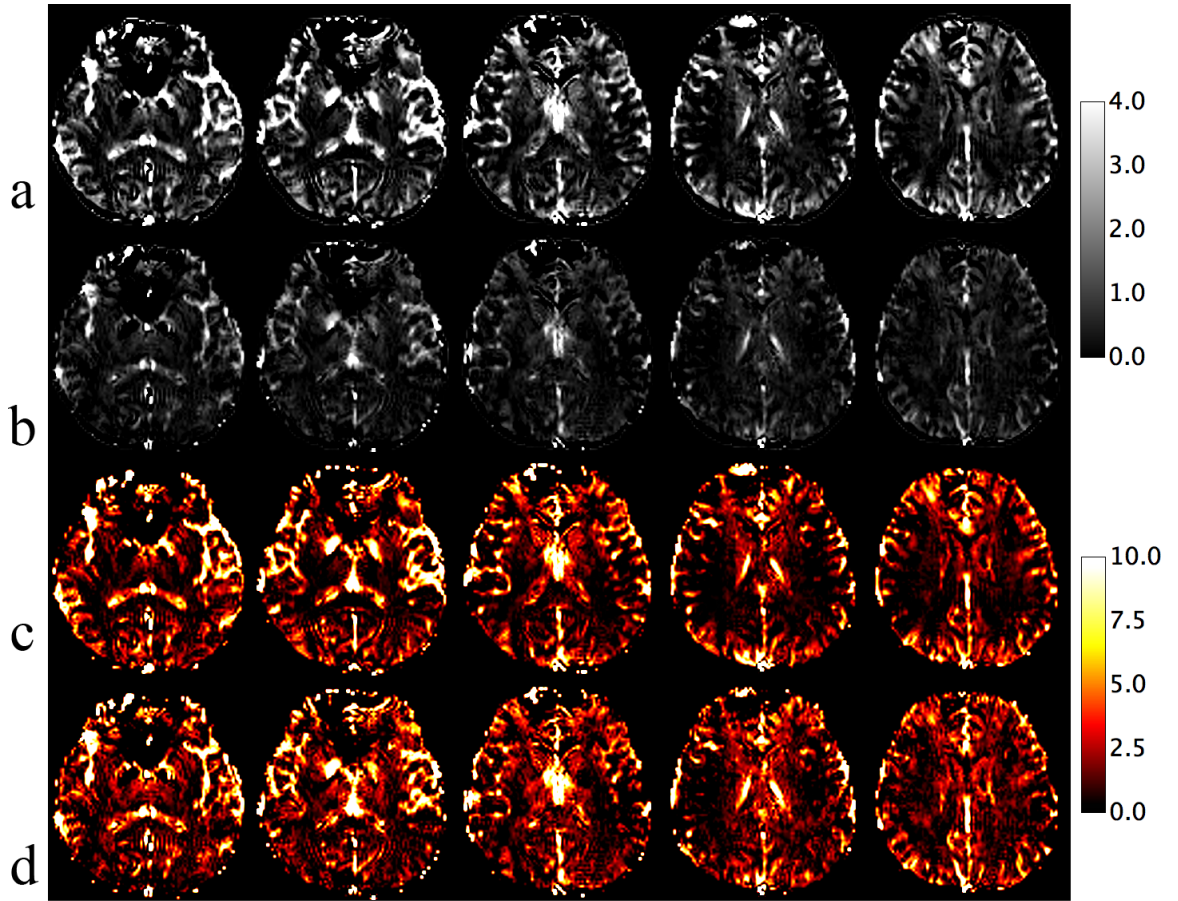


Figure 2.5. Percent difference and CBV maps in mL/100 g tissue calculated according to Eq. 1. Positive percent difference from baseline is shown for $\text{FiO}_2=1.0$ (a) and 0.5 (b). Despite the reduced signal enhancement of the lower FiO_2 , there still remains adequate BOLD contrast to allow for very similar CBV values for $\text{FiO}_2 = 1.0$ (c) and 0.5 (d), made possible by the process of normalization to a pure vein voxel (sagittal vein) in each dataset.

Table 2.2. Mean Global CBV Values (mL / 100 g) for All Subjects Measured with 100% and 50% Inhaled Oxygen

	FiO ₂ =1.0	FiO ₂ =0.5
Gray Matter	3.87 ± 0.43	3.95 ± 0.62
White Matter	2.41 ± 0.36	2.49 ± 0.58

2.8. Chapter Discussion

In this study, the paramagnetic effects of molecular oxygen in T₂^{*}-weighted hyperoxic contrast studies at different FiO₂ levels have been characterized. Of particular importance, we have characterized the effect of increased FiO₂ on static field inhomogeneity, and we have demonstrated the field strength dependence of this phenomenon. These effects can produce signal changes that are equal to or greater than the expected BOLD changes; therefore, it is not accurate to assume that hyperoxia is a purely intravascular source of image contrast in all brain regions. It may have been difficult to observe these effects in other studies of hyperoxic contrast because of the use of lower resolution EPI data, spatial filtering in post-processing, or because the slices acquired avoided the frontal sinuses or the ventricles (6,36,38). Also, since large voxels and spatial blurring kernels are commonly used, any negative changes may have been obscured, since BOLD contrast dominates in most brain regions.

It should be noted that the strength of the conclusions concerning the field-dependent effects are limited, since only a single subject was studied at both field strengths. However, the static field measurements made were found to be very stable during normoxia in all subjects studied, and the B_0 changes observed during hyperoxia at both field strengths were demonstrably large. Altogether, this provides reasonable grounds for confidence in the accuracy of these results.

There are several potential non-BOLD sources of signal changes during hyperoxia that present potential confounding variables in BOLD-modulated hyperoxic contrast studies of the brain. Substantial changes in B_0 in the frontal lobes during hyperoxia suggest an increase in the paramagnetism of the upper airway directly underneath the brain from increased local molecular oxygen concentration. Oxygen gas in other nearby spaces, such as in the mask itself, is also likely to have contributed to the observed effect. The paranasal sinuses may also play a role, but are less likely to substantially change their oxygen concentrations during the short inhalation epochs used in this study, as gas exchange between the nasal cavity and sinuses is slow (81). It is also possible that oxygen in the lower airway, including the lungs, played a role in changing the static field during hyperoxia, despite its relatively large distance from the brain (82). Gas in the lower airway would be expected to produce static field changes that are poorly localized and affect the entire brain. However, the large (> 0.1 ppm) B_0 changes observed in this

study were well-localized to the anterior and inferior brain regions near the nasal and oral cavities. Static field changes in other parts of the brain were found to be substantially smaller, and consistent effects were not observed across subjects. Although it seems reasonable to conclude that the effects of oxygen in the upper airway dominate the static field changes in the brain over contributions from the lower airway in the frontal lobes, it is possible that smaller static field changes occur across the brain during hyperoxia from oxygen gas in the lungs.

Increased static field inhomogeneity significantly increases intravoxel phase dispersion in all directions in T_2^* -weighted EPI acquisitions, which is most likely the main mechanism of the observed decrease in the signal in the frontal lobes. Static field changes also create significant image distortions and shifts in EPI acquisitions in the phase encode and through-slice directions. It has been shown in prior studies that changes in lung magnetic susceptibility can create image distortions and shifts that cause either negative or positive signal changes (depending on image orientation), with the most significant effects occurring at the edges of image intensity (82). These effects are very sensitive to small changes in the static field, and may be a significant source of signal changes observed at a distance from the frontal lobes, especially the periphery of the brain in the EPI acquisitions (see Figs. 1 and 2).

The CSF also appears to show reduced signal intensity in the EPI acquisitions. The reason for these changes is somewhat less clear. If dissolved oxygen was present in these regions, increased signal intensity would be expected from reduced T_1 . Based on the arguments in Chapter 1, the transverse relaxivity of molecular oxygen is likely to be extremely small, even if oxygen were interacting with large proteins. However, it is possible that this could affect the measured signal intensities near the ventricles and sulci if the oxygen concentration were very high during hyperoxia, as CSF constitutes a very large percentage of the voxel signal intensity. Although the transverse relaxation of arterial blood also decreased with hyperoxia (73), arterial cerebral blood constitutes less than 3% of tissue voxel volume (83) and signal reductions due to this effect are likely to be much less significant. It should be noted that B_0 shifts may contribute substantially to any signal changes measured in the CSF-filled spaces in the frontal lobes or at the periphery of the brain. Furthermore, for the reasons discussed in the previous paragraph, CSF regions across could show negative contrast due to global field shifts from changing in the oxygen concentration in the lungs, since CSF represents an image intensity boundary (82). We observed consistent signal reductions in the lateral ventricles in the center of the brain during hyperoxia (see Fig. 2.1), away from substantial image intensity edges and where B_0 shift effects are likely to be minimal, lending support to the idea that there is a subtle global effect from hyperoxia inhalation.

Reduced FiO_2 levels have been shown here to be effective in reducing the non-BOLD relaxation effects of inhaled oxygen. This adds further support to the physiological arguments for the use of lower FiO_2 (37) to reduce effects not related to BOLD-based signal modulation. Although the total percent of voxels showing negative signal change decreased with a lower level of hyperoxia, the percent signal increase from the BOLD effect in capillaries and veins decreased with lower FiO_2 . Therefore the beneficial effect of the decrease in negative contrast with lower FiO_2 is mitigated somewhat by the decreased BOLD response. However, despite the reduced BOLD contrast, the correspondence between values of CBV for $\text{FiO}_2 = 0.5$ and 1.0 measured in this study indicates that 50% oxygen inhalation exceeds the contrast-to-noise threshold necessary to produce precise and accurate CBV values. The relative effectiveness of $\text{FiO}_2 = 0.5$ may also be because a significant fraction of the excess oxygen carried to the capillaries under hyperoxia is from the increase in the saturation of the arterial hemoglobin, since it is not completely saturated under normal physiologic conditions (84). Furthermore, oxygen is known to modestly decrease the cerebral blood flow as a function of increased FiO_2 (37), which acts to reduce some of the expected increase in BOLD signal from the use of a higher FiO_2 . It should also be noted that accurate results for CBV measurement may be produced at an FiO_2 less than 0.5. The practical minimum FiO_2 for a given experiment will likely depend on the required contrast-to-noise ratio, which in turn will depend on several experimental parameters, including the duration and number of the inhalation epochs, the static field strength, and the signal-to-noise ratio of the imaging approach.

Several additional strategies could be pursued to reduce or eliminate the non-BOLD effects of hyperoxic contrast. It is theoretically possible to significantly reduce the distortion and dephasing effects due to static field alterations by acquiring a three dimensional B_0 map and additional reference scans to characterize the in-plane and through-plane EPI point spread function in both the normoxic and hyperoxic states (85). However, these correction methods require substantial increases in the scan time, are computationally intensive, and are themselves prone to many artifacts and errors, making their implementation in brief hyperoxia protocols impractical. Although it is not physically possible to recover signal from spins that is completely lost due to intravoxel dephasing, it is possible to deconvolve the contribution to T_2^* of a through-slice gradient with a detailed fit of the T_2^* decay curve (86). However, this approach is not possible in this context because this approach is too noisy given the small signal changes induced by hyperoxia. Higher resolution and thinner slices can also reduce the static field dephasing effects, but the penalty of reduced signal-to-noise ratio would likely be unacceptable given the relatively low levels of signal enhancement that can be obtained from BOLD contrast. Fully refocused fast spin echo approaches to BOLD imaging (87) would be insensitive to changes in the static magnetic field, but these approaches reduce BOLD contrast and are often limited by specific absorption rate, especially at high fields. Furthermore, they may be undesirable in certain hyperoxic contrast studies (e.g. CBV calculations) since T_2 -weighted BOLD contrast is dependent on vessel diameter. The T_2^* effects due to molecular oxygen in the CSF may be reduced or eliminated by the addition of saturation, inversion recovery, or long- T_2 suppression pulses to the EPI sequence that

null the signal from spins with long T_1 or T_2 values. Care must be taken with these approaches, however, since molecular oxygen reduces the longitudinal relaxation time in CSF, and T_1 -weighting of these sequences could result in artifactual increases in signal intensity if CSF signals are not suppressed adequately.

In conclusion, we have demonstrated that the paramagnetic effects of molecular oxygen significantly complicate the analysis of BOLD-modulated hyperoxic contrast studies of the brain. Negative signal changes were observed in T_2^* -weighted images in the frontal lobes, and B_0 maps suggest this effect is due to increased intravoxel dephasing from increased static field inhomogeneity from oxygen-induced susceptibility changes in and around the upper airway. Additional negative signal changes were observed in the ventricles and brain periphery, suggesting the effect of image distortions from oxygen-induced static field shifts, along with possible increased transverse relaxation rate in the CSF due to dissolved oxygen. Static field changes during oxygen inhalation were shown to scale with the main magnetic field strength, and the use of $FiO_2 = 0.5$ was shown to reduce negative signal changes while maintaining adequate BOLD contrast for accurate CBV calculation.

Chapter 3: *In Vivo* Measurement of Longitudinal Relaxation Time of Arterial Blood During Hyperoxia

3.1 Overview

ASL measurements of CBF during hyperoxia are confounded by the reduction in longitudinal relaxation time of arterial blood (T_{1a}) from paramagnetic molecular oxygen dissolved in blood plasma. The aim of this study is to accurately quantify the effect of arbitrary hyperoxic levels on T_{1a} . To mitigate artifacts, including the inflow of fresh spins, partial-voluming, pulsatility, and motion, a pulsed ASL approach was implemented for *in vivo* measurements of T_{1a} in the rat brain at 3 Tesla. After accounting for the effect of deoxyhemoglobin dilution, the relaxivity of oxygen on blood was found to closely match phantom measurements.

3.2 Introduction

Although it is well-known that inhaled oxygen creates a significant reduction in the T_1 of arterial blood (T_{1a}) (73,88), and that T_{1a} has a substantial effect on CBF measurements using ASL (89), only a small number of studies using arterial spin labeling (ASL) approaches to investigate the regional CBF changes during hyperoxia have incorporated T_{1a} changes in their CBF calculations (37,46). For some of these studies, the T_{1a} changes during hyperoxia were assumed from results of prior studies of arterial blood at 100%

oxygen inhalation (46). Other studies modeled the expected change in T_{1a} during hyperoxia at intermediate hyperoxia levels, since there are no established values of T_{1a} in the literature for various oxygen concentration levels (37). These approaches may be problematic for several reasons. First, the methods used in these studies (73,88) to measure T_{1a} are prone to several artifacts and errors. These include the inflow of fresh, un-inverted spins from outside the transmit coil, partial-voluming, pulsatility, and motion. Second, even under equivalent conditions of hyperoxia, T_{1a} changes may vary significantly between individuals due to physiologic variations in the blood. Third, it is not clear how to effectively model the expected T_{1a} changes at arbitrary oxygen concentration levels, since T_{1a} may be influenced by various factors other than the concentration of molecular oxygen in the plasma (e.g., dHb concentration). All of these issues point to the necessity the measurement of T_{1a} on a per subject and per gas condition basis that is free from significant artifacts.

To achieve these measurements, we implemented pulsed ASL (PASL) approaches for the measurement of T_{1a} (90), which allowed for accurate isolation of arterial blood and minimized partial-voluming and pulsatility artifacts. Due to the requirement that the transmit coil be larger than the subject to avoid the contamination of the measurement from inflowing spins (90), in addition to the long scan times inherent to inversion-recovery measurements of T_1 , adult rats were chosen as a model organism, since they are

substantially smaller than the transmit coil and will experience hematologic changes in response to hyperoxia that are similar to humans.

3.3 Material and Methods

3.3.1 Phantom Study of Oxygen Longitudinal Relaxivity

To characterize T_1 as a function of dissolved oxygen concentration, a phantom study was performed by bubbling a mixture of nitrogen and oxygen into phosphate-buffered saline (PBS) in a centrifuge tube held at 37⁰ C in a water bath. After ten minutes, to allow the gas to fully dissolve in the solution, an airtight lid was secured, and the tube was immediately transferred to a foam-insulated holder positioned inside the magnet. Since the measurement of T_1 lasted only approximately three minutes, it was not necessary to heat the phantom while it was in the magnet. An inversion-prepared single-shot FSE sequence was used with ten inversion times (90, 200, 400, 800, 1200, 1600, 2400, 4000, 6000, 1000 ms) with a TR = 20 s. Temperature measurements were performed before and after the imaging experiment, and all temperature decreases were found to be less than 0.5⁰ C. This process was repeated for 0 to 100% oxygen (0 to 760 mm Hg) in steps of 10%. To investigate the possible influence of blood proteins on the relaxivity of molecular oxygen, this experiment was repeated with 5% bovine serum albumin in PBS. All measurements were repeated five times using separate samples.

3.3.2 Animals

All experiments performed were part of an approved protocol by our Institutional Animal Care and Use Committee. All data were obtained using adult male Sprague-Dawley rats (n=5; 434-467 g; Charles River, MA, USA). Anesthesia was induced with 3% isoflurane in oxygen for approximately five minutes, and the animals were then maintained on spontaneous inhalation anesthesia consisting of 1.5% isoflurane in 30% oxygen delivered at 1.5 L/min through a close-fitting nose cone. If the animal showed any signs of movement during the data acquisition, the anesthesia was increased to 1.7-1.8% isoflurane for the remainder of the experiment. The fraction of inhaled oxygen (FiO_2) was kept at a minimum of 0.3 instead of 0.21 (air) to ensure that physiologic stability was maintained and to prevent oxygen desaturation. Normoxia in this context refers to $\text{FiO}_2 = 0.3$, and hyperoxia refers to $\text{FiO}_2 = 1$. All gases were delivered to the animal with a manually controlled oxygen and nitrogen flowmeters, which were then mixed, and run through an inline isoflurane vaporizer. A temperature-controlled water blanket was placed under the rat to maintain body temperature at 37.0 ± 0.2 °C; temperatures were measured continuously with an optical probe inserted in the rectum. Head movement was restricted during imaging using a custom built MR-compatible animal cradle with attached earbars. To draw arterial blood gases, an arterial catheter was surgically inserted using a cut down of the ventral surface of tail. All blood gas samples were measured using disposable cartridges and a hand-held blood gas analyzer (i-STAT System; Abbott Laboratories, Abbott Park, IL, USA).

3.3.3 Hyperoxia Challenge Paradigm

Each rat underwent a series of hyperoxic challenges lasting twenty minutes each. After a five minute baseline period, gases were manually switched from 30% O₂ to 100% O₂ for ten minutes of hyperoxia, and then were switched back to 30% for a five minute baseline. Data acquired during the first two minutes after switching gases was not analyzed to allow for physiological adjustment to the new gas condition. Hyperoxic challenges were repeated continuously without a rest period.

A second imaging experiment was done to determine the degree of T_{1a} change with hyperoxia. All animals were subjected to graded hyperoxia levels of 40%, 60%, 80%, and 100% (in order) during continuous measurement of T_{1a}. As before, data acquired during the first two minutes after switching gases was not analyzed, and there was no rest period between gas conditions.

3.3.4 MRI Hardware

All imaging experiments were performed using a whole-body clinical 3T MRI scanner (Siemens Trio; Siemens Healthcare, Erlangen, Germany). RF excitation pulses were transmitted with the scanner body coil, and MR signals were received with a custom built single loop (35 mm ID) receive-only head coil passively decoupled during transmit. The head coil was fixed firmly over the dorsal aspect of the head of the animal.

3.3.5 Measurement of Arterial Blood T_1 (T_{1a})

A pulsed ASL method based on the work of Thomas, et al. (90) was used to measure T_{1a} in each animal. A schematic of the pulse sequence is shown in Fig. 3.1. The same PICORE inversion described above was used to label arterial blood. The inversion was preceded by an in-plane saturation pulse to limit the interaction of the inversion pulse with the static tissue spins in the imaging region. The approach used by Thomas, et al. (90) employed a global saturation pulse to prepare the magnetization along with a flow-sensitive alternating inversion recovery (FAIR) ASL sequence. We used a global inversion pulse instead of a saturation pulse to prepare the magnetization, which has the advantage of increased dynamic range. Furthermore, the use of the PICORE ensures that there is no contamination with venous blood in the measurement, as is possible when using FAIR. It is important to note that because the transmitter coil is much larger than the rat, there is no potential for error in the measurement due to the inflow of uninverted blood into the imaging region. Image acquisition was performed with a single-slice, single-shot FSE sequence. Imaging parameters were: TE/TR: 25/8000 ms, slice thickness = 8 mm, FOV = 64×64 mm, matrix size = 64×64 , and phase encode direction = left-to-right.

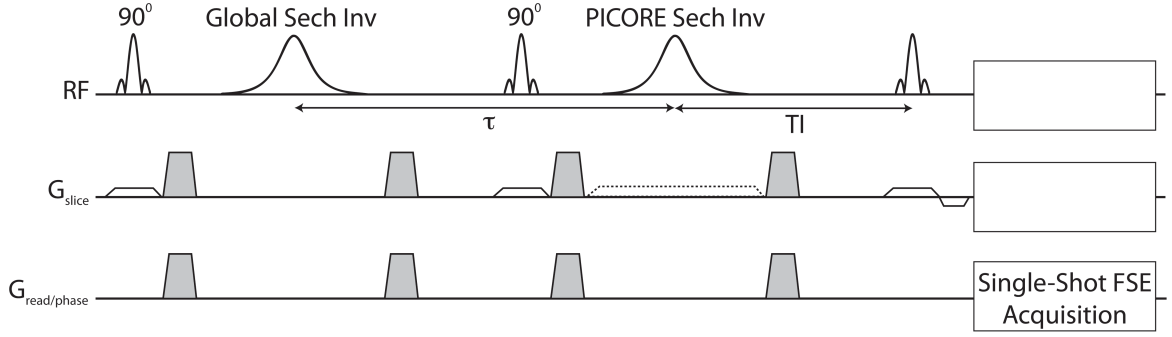


Figure. 3.1. Pulse sequence diagram of the PICORE sequence with a global inversion preparation. An in-plane presaturation pulse was followed by a global hyperbolic secant inversion pulse. After a variable inversion preparation time, τ , a second in-plane saturation pulse was followed by either a slab-selective hyperbolic secant pulse inferior to the imaging slice (tag) or the same pulse without the slab-selective gradient (control). Control and tag pulses were interleaved for each acquisition. After an inversion time TI, a single-shot FSE acquisition was performed. By keeping TI fixed (1.5 s) and using a series of values of τ , a value of the T_1 of arterial blood (T_{1a}) was obtained.

If TI is kept at a constant value while the inversion preparation time τ is varied, the PICORE signal difference can be expressed as:

$$\Delta M = A \cdot (1 - 2 \cdot \alpha \cdot e^{-\tau/T_{1a}}) \quad [3.1]$$

where A is a voxel-specific constant independent of τ . To allow for a robust, overdetermined fit to Eq. [3.1] in each animal, ten values of τ (65, 400, 800, 1200, 1600,

2000, 2400, 3200, 4000, and 6000 ms) were used with a constant TI of 1500 ms. A randomized acquisition order was used, and tag and control images were interleaved for each value of τ . Ten repetitions of each value of τ were obtained with a total imaging time of 27 min. To increase the number of T_{1a} measurements during hyperoxic challenges, the same approach was used, except only four values of τ (65, 900, 2500, and 6000 ms) were obtained. To increase the robustness of the fit, these data were only fit for A and T_{1a} , with the value α taken from the fit from the previous experiment.

3.3.6 Data Analysis

All images were analyzed using routines and scripts written in MATLAB (MathWorks, Inc.). For analysis of the T_{1a} data, whole brain ROIs were drawn on the PICORE signal difference images (see Fig. 3.2) and the mean values were determined. The acquisition using ten values of τ was fit to Eq. [3.1] for α , A , and T_{1a} using a non-linear least squares fit (MATLAB function, `lsqcurvefit`). The value of α determined from this fit was used in the fit of data from the acquisition using four values of τ , so that only A and T_{1a} were fit to Eq. [3.1]; also, the values from the prior fit were input as starting values for the subsequent fit. This approach yielded a stable and fast converging fit for all the data. Before this analysis, the T_{1a} data obtained from all three hyperoxia challenges was separated into normoxic and hyperoxic periods and averaged. The difference in T_{1a} between normoxic and hyperoxic states across all animals was compared with a paired Student's t-test.

To analyze the difference in T_{1a} in the blood versus arterial partial pressure of oxygen (PaO_2), the effects of molecular oxygen and deoxyhemoglobin (dHb) were considered. R_1 ($1 / T_1$) is known to increase linearly with increasing dHb concentration (21). Therefore, the R_1 of blood versus PaO_2 (longitudinal relaxivity of blood as a function of PaO_2 , or $r_1^{PaO_2}$) was modeled as the addition of the linear longitudinal relaxivities of blood as a function of molecular oxygen concentration ($[O_2]$; determined by blood gas PaO_2) and dHb concentration ($1-Y$, where Y is the fraction of oxyhemoglobin to total hemoglobin; determined by P_{50} and blood gas PaO_2), which can be expressed simply as:

$$r_1^{PaO_2} = r_1^{[O_2]} + r_1^{dHb} \quad [3.2]$$

The experimental R_{1a} values were fit to this model using a non-linear least squares fit in MATLAB (function `lsqcurvefit`).

3.4 Inversion-Prepared ΔM as a Function of Preparation Time

A representative set of ΔM images during normoxia with ten values of τ is shown in Fig. 3.2. As predicted from the model, the signal increased exponentially from an initial negative value of ΔM and changed globally to the final expected positive value of ΔM as τ increased. The values of ΔM around the periphery of brain are reduced due the partial voluming from the large voxel size. However, these effects remain the same across all values of τ and do not affect the calculation of T_{1a} . The experimental data from the

whole-brain ROIs from each animal, along with the fits to Eq. [3.1] are shown in Fig. 3.3. By visual inspection, the magnetization is well described by a monoexponential recovery. The average value of α was found to be 0.94 in the T_{1a} experiment, which (although still high) was lower than that found experimentally for a single inversion (0.97).

3.5 Baseline T_{1a} Values and T_{1a} Response to Hyperoxia

The numerical values from the fits of these data are shown in Table 3.1, along with the fit values obtained from T_{1a} measurements made during the hyperoxic challenges. The baseline T_{1a} measured with ten values of τ was in very close agreement with the T_{1a} measured with four values of τ during the baseline normoxic phase measured before, between, and after the hyperoxic challenges. The baseline normoxia values of T_{1a} measured were found to be consistent over time in the same animal, but varied between animals. The measured values of T_{1a} during hyperoxia were found to decrease significantly compared to normoxia ($p < 0.01$). During hyperoxia, T_{1a} decreased by -89 to -170 ms or -5.6 to -9.4% from normoxia, with an average decrease of -125 ms or -7.4% . Figure 4 shows the values of T_{1a} calculated for increasing levels of FiO_2 . Values of T_{1a} were found to decrease consistently with increasing FiO_2 , with the relative decrease in T_{1a} each animal approximately equal.

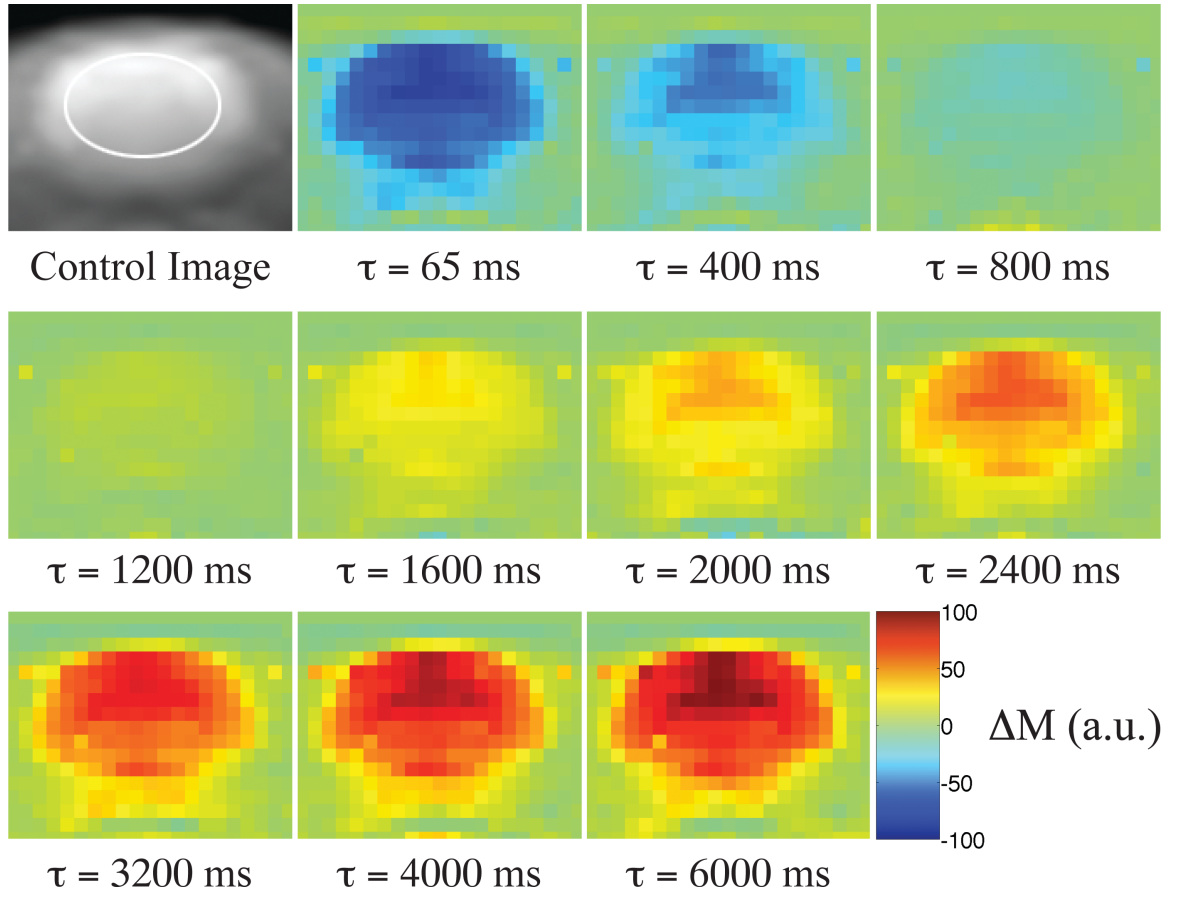


Figure. 3.2. A representative set of PICORE signal difference ΔM (control minus tag) images in arbitrary units (a.u.) from the pulse sequence shown in Fig. 1. Note that the ΔM signal recovered globally through zero from an initial negative value as the inversion preparation time τ increased. The mean value from a whole brain ROI (outlined in white in the control image) was used to analyze the signal behavior.

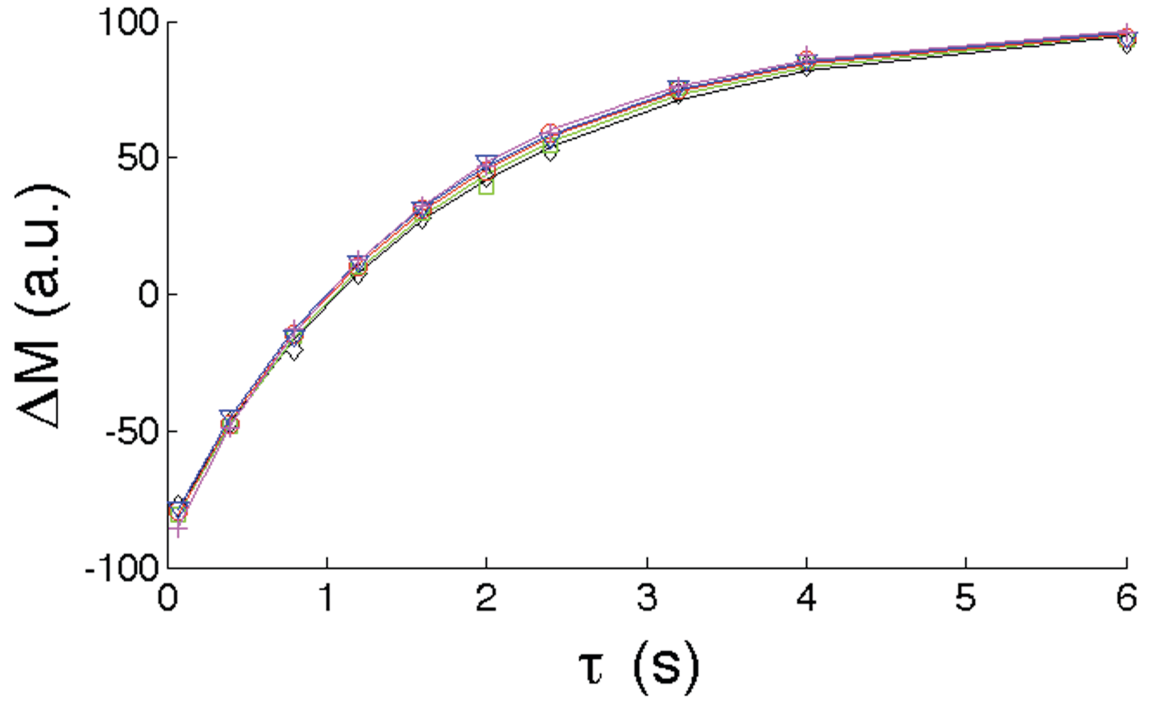


Figure. 3.3. PICORE signal difference (ΔM) in arbitrary units (a.u.) versus inversion preparation time τ in a whole brain ROI (see Fig. 2) during normoxia ($\text{FiO}_2=0.3$) in five rats. Ten different values of τ were used, and the data was fit to Eq. [3.1] for each animal using a non-linear least squares regression. The data fits are shown as solid lines and experimental data are shown as symbols.

Table 3.1. Measured T_{1a} Values in Whole Brain ROIs During Normoxia ($FiO_2 = 0.3$) and Hyperoxia ($FiO_2 = 1.0$)

Animal no.	Baseline T_{1a} (s) [†]	Normoxia T_{1a} (s) [‡]	Hyperoxia T_{1a} (s) [‡]
1	1.713	1.70	1.54
2	1.651	1.64	1.49
3	1.603	1.58	1.48
4	1.524	1.54	1.45
5	1.609	1.62	1.53
Mean \pm SD	1.620 \pm 0.069	1.621 \pm 0.063	1.496 \pm 0.035 [*]

[†] Values calculated from measurement performed with 10 inversion preparation times, τ .

[‡] Values calculated from measurement performed with 4 inversion preparation times, τ .

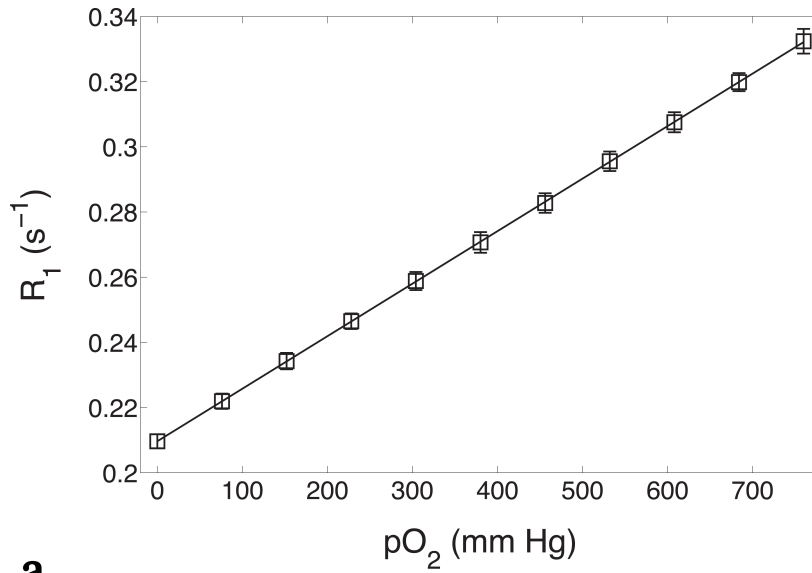
^{*} $P < 0.01$ from normoxia.

3.6 Longitudinal Relaxivity of Oxygen in PBS and Arterial Blood *In Vivo*

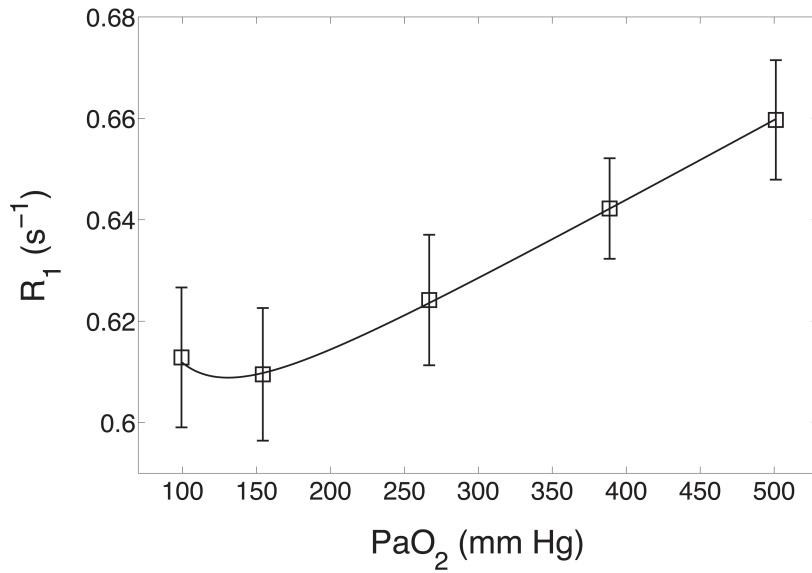
Figure 3.4a shows R_1 versus pO_2 in the PBS calibration phantom. Using a linear regression, the longitudinal relaxivity of molecular oxygen in PBS was found to be $1.61 \pm 0.02 \times 10^{-4} \text{ s}^{-1} \text{ mm Hg}^{-1}$, with $R^2 = 0.99$. No statistically significant difference was found in the relaxivity of the phantom containing bovine serum albumin.

Fig. 3.4b shows R_1 versus PaO_2 . The PaO_2 was measured for each case using arterial blood gas. Using the fit to the model shown in Eq. [3.2] above, the $r_1^{[O_2]}$ was determined to be $1.59 \pm 0.21 \times 10^{-4} \text{ s}^{-1} \text{ mm Hg}^{-1}$, while the $r_1^{[dHb]}$ was found to be $0.246 \pm 0.051 \text{ s}^{-1} (1-Y)^{-1}$. There was found to be a clear influence of dHb on T_{1a} values measured between

FiO₂ = 0.3 and 0.6, with the T_{1a} at FiO₂ = 0.4 actually showing a slight increase. At higher FiO₂ levels, the longitudinal relaxivity with PaO₂ appeared to be linear. The values of T_{1a} were found to be 1.632 ± 0.037 ms, 1.641 ± 0.035 ms, 1.606 ± 0.033 ms, 1.549 ± 0.024 ms, and 1.514 ± 0.027 ms for FiO₂ = 0.3, 0.4, 0.6, 0.8, and 1.0, respectively. There was no statistically significant difference between the T_{1a} measured during FiO₂ = 1.0 during the first experiment (rapidly alternating oxygen levels) and the second experiment (gradual hyperoxia).



a



b

Figure 3.4. Effect of oxygen concentration on R_1 in a phosphate-buffered saline (PBS) phantom (a) and effect of arterial oxygen tension on R_1 of arterial blood (b). The marker indicates the experimental data, and the lines indicate the fits to the data. The effect of oxygen on R_1 in (a) was shown to be well-described by a linear fit to the data. The data were well described by a model incorporating the linear

relaxivity effect of both molecular oxygen and deoxyhemoglobin. Values shown are mean \pm SD.

3.7 Chapter Discussion

In this study, we have measured T_{1a} *in vivo* at 3T during normoxia and hyperoxia using a novel PASL approach. This particular approach is notable for avoiding several artifacts and the requirement for physiological gating. Compared to a similar approach in the literature, it approximately doubled the dynamic range with the use of an inversion preparation, avoided possible venous signal contamination with a PICORE inversion, and maximized the signal-to-noise ratio (SNR) in the presence of static field inhomogeneities by using a FSE readout. We have accurately measured the longitudinal relaxivity of oxygen at physiologic temperature at 3T. Additionally, our model of the relaxivity of arterial blood accurately describes the situation *in vivo* by incorporating the effect of the longitudinal relaxivity deoxyhemoglobin. Given that the longitudinal relaxivity was not effected by albumin, it is likely that the interaction of molecular oxygen with blood proteins is too rapid to affect T_{1a} . Therefore, the measured relaxivity of oxygen in blood is likely to be independent of B_0 , and these relaxivity values can be used for experiments at different field strengths.

The average value of T_{1a} measured during normoxia shows close agreement to values from previous studies *in vivo* (1623 ms; (91)) and *in vitro* (1664 ms; (92)). The measured value of T_{1a} in response to oxygen was shown to closely agree with phantom data after

accounting for the effect of changing dHb concentration on T_{1a} . The measured relaxivity of dHb was found to be in agreement with previous results (21,92). Additionally, the reduction in T_{1a} due to oxygen was observed to be rapid and consistent across large differences in the duration of oxygen exposure. The observed T_{1a} changes of our *in vivo* data very closely approximated the more robust phantom data.

Although not a trivial operation, the measurements of T_{1a} in rat blood made in this study can be translated to human studies. Given the similarity in the constitution of blood between the two species, the longitudinal relaxivity from dissolved molecular oxygen is likely to be very similar. The most important difference between species is effect of deoxyhemoglobin, which will exist in different concentrations at the same PaO_2 (due to the difference in P_{50}) and will likely exhibit different longitudinal relaxivity. However, if these effects can be characterized and accounted for, it should be possible to accurately estimate the change in T_{1a} during any oxygen challenge, given knowledge of PaO_2 during normoxia and hyperoxia. To this end, it is possible to estimate PaO_2 from end-tidal oxygen concentration, given normal lung physiology (6).

In conclusion, using measurements of in phantoms and *in vivo* arterial blood, we have demonstrated that T_{1a} is well described by the linear combination of longitudinal relaxivities of molecular oxygen and deoxyhemoglobin. By comparing brief and graded hyperoxic inhalation paradigms, we have shown that T_{1a} changes rapidly and remains stable with changing FiO_2 .

3.8 Future Directions

Given the challenges of making *in vivo* T_{1a} measurements in humans, the use of small animal model may be the most practical method for T_{1a} calibration for human experiments. However, a direct measurement of T_{1a} on a per subject and per condition basis is still a desirable goal, given the relatively large inter- and intrasubject variability in T_{1a} in baseline normoxia as well as in response to oxygen challenge. Although such an approach may be feasible, we found a consistent underestimation of T_{1a} by several hundred milliseconds when applying the above method to humans using the same clinical scanner. Several changes from the present approach are likely to be necessary to obtain this goal, including minimizing the number of acquired inversion preparation times, and the application of the constraint on the duration of the inversion preparation times to values short enough to avoid contamination of spins flowing in from outside the transmit coil.

Chapter 4: Absolute Quantification of Cerebral Perfusion with Pulsed Arterial Spin Labeling During Hyperoxia

4.1 Overview

As discussed in Chapter 1, quantitative arterial spin labeling estimates of cerebral perfusion during oxygen inhalation are important in several contexts, including functional experiments calibrated with hyperoxia and studies investigating the effect of hyperoxia on regional perfusion. The aim of this study is to accurately quantify the effect of arbitrary levels of hyperoxia on CBF on a per-subject basis using ASL by correcting for T_{1a} with a simultaneous measurements on a per subject, per gas condition basis. The results of this study suggest that measured ASL signal changes are dominated by reductions in T_{1a} for brief hyperoxic inhalation epochs, while physiologic effects of oxygen on vasculature account for most of the measured reduction in CBF for longer hyperoxic exposures.

4.2 Introduction

Hyperoxic gas inhalation, through increases in the arterial partial pressure of oxygen and hemoglobin saturation (SaO_2), exerts significant effects on the vasculature and is not physiologically inert. Many studies have shown that oxygen reduces cerebral blood flow (CBF) due to at least one independent vasoconstrictive mechanism, including the

attenuation of the effect of nitric oxide, an endogenous vasodilator (5,49,50,93). While the vasoconstrictive effect of oxygen is well known, the degree to which CBF changes occur during hyperoxia remains the subject of ongoing research. Moreover, if inhaled oxygen is to be used as a quantitative contrast agent, precise characterization of its changes to the underlying physiology is crucial.

Several studies have used arterial spin labeling approaches to investigate the regional CBF changes during hyperoxia (5,37,46,48,93,94), but only a small number of these studies have incorporated T_{1a} changes in their CBF calculations (37,46). As mentioned in Chapter 3, the reduction of T_{1a} will significantly affect measured values of CBF using ASL, as preparation times of ASL inversion pulses are on the order of the T_1 of the tagged spins (89). In this study, our aim was to simultaneously measure CBF and T_{1a} *in vivo* during various levels of hyperoxia using the method outlined in Chapter 3. In particular, we wanted to explore the previously reported finding (37,46) that CBF change as measured by ASL during hyperoxia is primarily artifactual, since it is dominated by a reduction in T_{1a} (37,46). We implemented a pulsed ASL (PASL) approach for CBF that was similar in implementation to the arterial spin tagging method outlined in Chapter 3. Using this method, we were able to simultaneously measure these parameters in the brain without moving the subject. As discussed in Chapter 3, although there is no reason in theory that these measurements cannot be done *in vivo* in humans, technical issues require that a smaller experimental animal be used. The rat was chosen due to its

physiologic stability under anesthesia and the relative similarity of its physiologic blood responses to humans.

4.3 Material and Methods

4.3.1 Animals

All experiments performed were part of an approved protocol by our Institutional Animal Care and Use Committee. All data were obtained on adult male Sprague-Dawley rats (n=13; 429-472 g; Charles River, MA, USA). Inhalation anesthesia was induced and maintained in the same manner as described in Section 3.3.2. All arterial blood gases were drawn from tail artery catheter. Again, to ensure that physiologic stability was maintained and to prevent oxygen desaturation, animals were maintained with a minimum FiO_2 of 0.3 (normoxia in this study). Gases were delivered and altered, temperature was maintained constant, and head movement was restricted as described in above in Chapter 3.

4.3.2 Hyperoxia Challenge Paradigms

The response of CBF to oxygen was studied under two different hyperoxia paradigms: (1) a brief hyperoxic challenge (Group I) and (2) an increasing, graded hyperoxic challenge (Group II), as illustrated in Fig. 4.1. All data acquired during the first two minutes after switching gases were not analyzed to allow for physiological adjustment to the new gas condition. To investigate possible effects unrelated to variations in inspired

oxygen (e.g. scanner drift, duration of anesthesia, etc.), data were collected for control animals (n=2) using the same measurement protocols of Group I and II described below without switching gas conditions (i.e., under continuous normoxia).

In Group I (n=7), each rat underwent a baseline – stimulation – rest paradigm. After a five minute baseline period, gases were switched from 30% O₂ to 100% O₂ for ten minutes of hyperoxia, and then were switched back to 30% for a five minute baseline. This paradigm was repeated three times during continuous measurement of T_{1a} and CBF (detailed below). In addition, a second experiment was performed in Group I animals to determine the degree of T_{1a} change with hyperoxia. Animals underwent graded hyperoxic inhalation epochs of 40%, 60%, 80%, and 100% (in increasing order) lasting approximately ten minutes each during which continuous measurements of T_{1a} were made.

In Group II (n=6), both T_{1a} and CBF were measured with graded hyperoxic inhalation epochs of 30%, 40%, 60%, 80%, and 100% (in increasing order). Each measurement of T_{1a} or CBF lasted approximately ten minutes, with two measurements of CBF occurring between two measurements of T_{1a} to minimize temporal effects. After gases were switched, approximately ten minutes elapsed before the start of the measurements to allow for physiological equilibration to the new gas condition.

For Group II, arterial blood gases were drawn from a subset of animals (n=4) during the imaging experiment immediately after each inhalation epoch. For Group I, blood gases were also analyzed from a subset of animals (n=4), but samples were drawn on a subsequent day to eliminate possible effects of the blood draw on the imaging experiment (95). Arterial blood gas measurements were not considered to be a significant issue for Group II animals, as there was adequate recovery time after each blood withdrawal (8-9 min). All blood gas samples were measured using the technique described previously (Section 3.3.2).

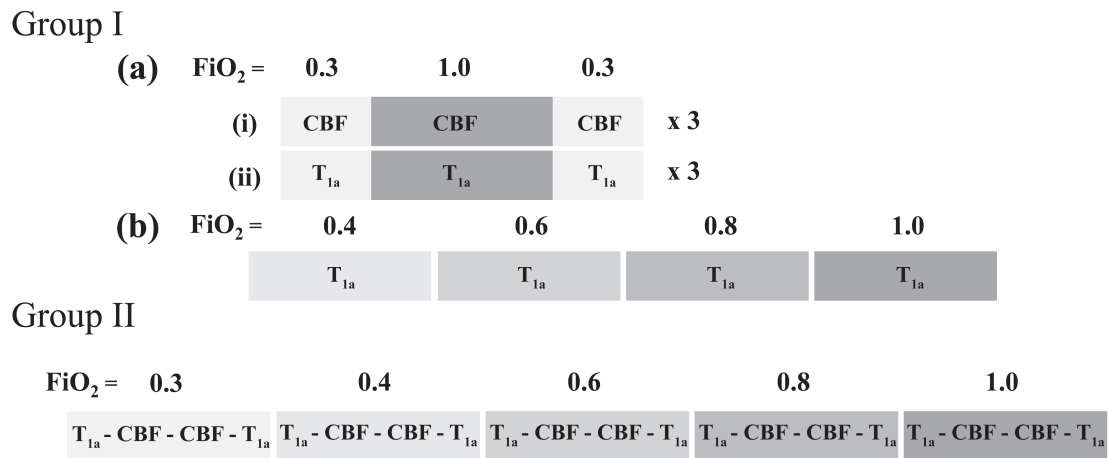


Figure 4.1. Hyperoxic challenge paradigms used for Group I and II animals. Group I animals underwent a baseline – stimulation – rest paradigm (5 – 10 – 5 min) to assess the effects of a brief hyperoxic inhalation challenge on CBF and T_{1a} . Group II animals experienced a graded hyperoxic challenge to test the effects of longer oxygen exposures on CBF and T_{1a} . Each gas inhalation period lasted approximately 40 minutes. To minimize temporal effects, two CBF measurements

were placed between two T_{1a} measurements. In addition, in Group I animals, a graded hyperoxic inhalation was used to assess T_{1a} at different oxygen concentrations.

4.3.3 Measurement of Cerebral Blood Flow (CBF) with Pulsed ASL

All imaging experiments were performed using the same MRI scanner and custom RF hardware as described in Section 3.3.4. The measurement of arterial blood T_1 was performed in the same manner as described previously. Briefly, a dataset was collected initially with ten inversion preparation times (τ) to allow for a robust fit to Eq. 3.1 to determine T_{1a} and α . When hyperoxic gas changes were implemented, a shorter approach was used with four values of τ to increase signal-to-noise of the T_{1a} measurement. Data from these shorter acquisitions were only fit to A and T_{1a} of Eq. 3.1.

To quantify CBF, a pulsed ASL technique developed by Wong and Luh (96,97), was used in this study for regional quantification of CBF (shown in Fig. 4.2). This technique involves quantitative imaging of perfusion using a single subtraction with thin-slice T_1 periodic saturation (Q2TIPS) based on proximal inversion with control for off-resonance (PICORE) tagging. This method is insensitive to spatially varying transit delay (δt) and flow-through effects (98), which have been shown to be significant sources of systematic error in perfusion quantification in rats (99).

A multi-shot fast spin echo sequence (FSE) was used for data acquisition. This approach is insensitive to static field inhomogeneities, and therefore should be insensitive to the hyperoxia-induced B_0 shifts discussed in Chapter 2. The inversion pulse for tagging consisted of a 40 ms adiabatic hyperbolic secant pulse with a 100 mm slab thickness (gradient turned off for the control image) positioned 10 mm proximal to the inferior imaging slice. To saturate the tag, a series of 90° three-lobe sinc pulses with 20 mm slab thickness, positioned 10 mm proximal to the inferior imaging slice were used for periodic saturation. The inferior saturation pulses were 20 mm thick and spaced 25 ms apart, creating a cutoff velocity of 80 cm/s (97). This cutoff velocity was considered sufficient to saturate inflowing spins because peak systolic velocity in normal rat carotid arteries measured with ultrasound is typically found to be less than 60 cm/s (100). Periodic saturation was continued until image acquisition to ensure full saturation of intravascular spins during imaging. The imaging parameters were: $TI_1 = 900$ ms, $TI_{1S} = 1475$ ms, $TI_2 = 1500$ ms, $TE/TR = 6/4000$ ms, slice thickness = 2 mm, slice gap = 2 mm, no. of slices = 3, FOV = 40×40 mm, matrix size = 64×64 , no. of segments = 5, phase partial Fourier factor = $5/8$, echo spacing = 6.03 ms, and time between slice acquisitions = 54 ms. The phase encode direction was set left-to-right to avoid pulsation artifacts from the carotid arteries beneath the brain. ASL tag/control pairs were obtained in 40 s ($TR = 4$ s \times 5 segments \times 2). The equilibrium magnetization scan was acquired with the exact same imaging parameters, except there were no saturation or inversion pulses, and TR was set to 15 s.

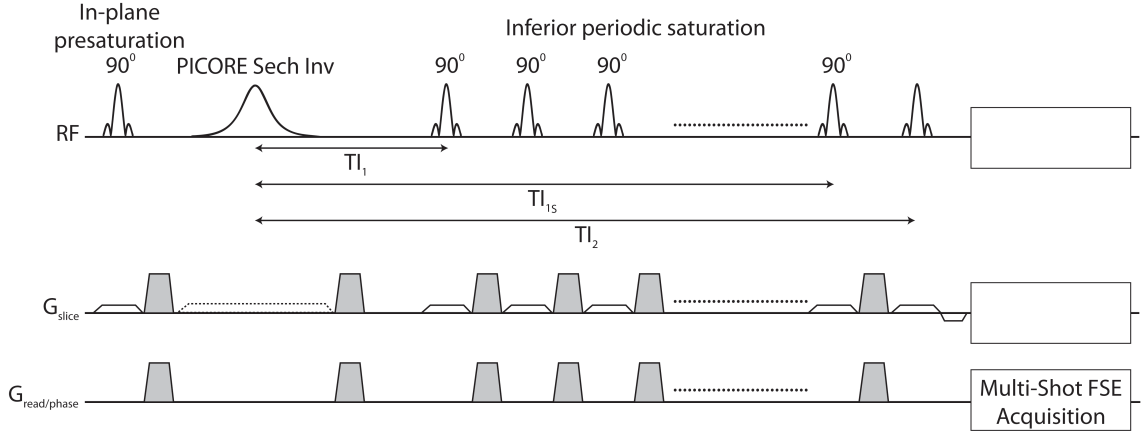


Figure 4.2. A multi-shot fast spin echo sequence (FSE) quantitative imaging of perfusion using a single subtraction with thin-slice TI_1 periodic saturation (Q2TIPS) based on proximal inversion with control for off-resonance (PICORE) tagging. By saturating the end of the tag using a series of 90° three-lobe sinc pulses, this method is insensitive to spatially varying transit delay (δt) and flow-through effects

The ASL signal difference ΔM is independent of δt (96) and the signal can be expressed by:

$$\Delta M = 2 \cdot \alpha \cdot M_{0a} \cdot f \cdot TI_1 \cdot e^{-TI_2/T_{1a}} \quad [4.1]$$

$$\text{for } TI_1 < \sigma \quad \text{and} \quad TI_2 > TI_1 + \delta t \quad [4.2]$$

where α is inversion efficiency (=1 for perfect inversion), M_{0a} is the fully relaxed longitudinal magnetization of arterial blood, f is cerebral blood flow in ml blood/g tissue/min, T_{1a} is the longitudinal relaxation time of arterial blood, and σ is the time duration of tag. Since the inversion pulse covered the entire rat heart and lungs, the tag did not have an end; typical values of δt for vessels of the rat neck to the brain are less than 400 ms (99). Therefore, the parameters used here should meet the conditions of Eq. [4.2] for all imaging regions. Using an agarose phantom, the inversion efficiency was determined experimentally to be approximately 0.97. Although changing oxygen concentrations along the vascular tree and spin exchange with different tissue compartments make the use of a single value T_{1a} a somewhat oversimplified approach (101), the model in Eq. [4.1] is a reasonable approximation since the tagged spins will spend the majority of TI in the arteries and arterioles. Furthermore, this model is important to consider since it represents the maximum degree of change in measured CBF that could be expected from a change in T_{1a} (see Chapter Discussion).

The value of magnetization of arterial blood was estimated on a per voxel basis using the local transverse magnetization of the reference scan and scaling it to the blood-brain partition coefficient (89,102). This method of estimating local M_{0a} has the advantage of simultaneously correcting for inhomogeneities of the receive coil (103). Correcting for the proton density and the relaxation rate of the local transverse magnetization and arterial blood, the magnetization of arterial blood can be expressed as:

$$M_{0a} = R \cdot M_0 \cdot e^{(1/T_{2LT} - 1/T_{2a}) \cdot TE} \quad [4.3]$$

where R is the signal ratio of local transverse magnetization to blood in a proton-density weighted image, M_0 is the voxel signal intensity, T_{2LT} is the T_2 of the local transverse magnetization, and T_{2a} is the T_2 of arterial blood. An approximate value of $R=0.98$ was taken from human studies (104). The T_2 of human gray matter at 3T (80 ms; (105)) was used to estimate a value of T_{2LT} , and an approximate value of T_{2a} (100 ms) was determined from the literature (22). Because of the minimal T_2 -weighting of our sequence ($TE = 6$ ms), the expected oxygenation changes occurring at the arteriole and capillary spaces during hyperoxia are expected to yield changes in T_{2a} that would change the measured signal by less than 1% (22,73,88). Therefore, we assumed a single estimate of T_{2a} for normoxic and hyperoxic states.

T_2 -weighted anatomical images were acquired with a multi-shot FSE sequence with the same slice prescription as the ASL sequence, with the following parameters: TE/TR : 81/4000 ms, slice thickness = 2 mm, slice gap = 2 mm, no. of slices = 3, FOV = 40×40 mm, matrix size = 192×192 , no. of segments = 24, and no. of averages=6.

4.3.4 Data Analysis

All images were analyzed using routines and scripts written in MATLAB (MathWorks, Inc.). Analysis of the T_{1a} data was performed in the same manner as previously described in Section 3.3.6. Before this analysis, the T_{1a} data for each animal and gas condition in Group I and Group II were compiled. For Group I T_{1a} data, the difference in T_{1a} between normoxic and hyperoxic states across all animals was compared with a paired Student's t -test. A one-way analysis of variance (ANOVA) was used to compare the difference in T_{1a} values between different gas conditions pooled from Groups I and II.

CBF maps were generated for each gas condition for all animals in Group I and II using the T_{1a} measured during normoxia (T_{1a} uncorrected), and another CBF map was generated for the hyperoxic condition using the value of T_{1a} measured in that animal for the given level of hyperoxia (T_{1a} corrected). CBF data were analyzed regionally for normoxia and hyperoxia ($FiO_2 = 0.3$ and 1.0) and whole brain averages for all gas conditions in both experimental groups. Regional analysis was performed because several studies have suggested that there are significant regional variations in the reduction of CBF during hyperoxia (37,46,49). Using the anatomical images, regions-of-interest (ROIs) were manually drawn using a standard rat brain atlas (106) and were then transferred to the perfusion maps. The differences across all ROIs between the two gas conditions were measured using a two-way ANOVA with replication. If the ANOVA showed significant differences in the means between the two gas conditions across all ROIs, analysis of the source of the differences using paired Student's t -test between

individual ROIs was considered to be warranted. In all cases, a value of $p < 0.05$ was considered a statistically significant difference.

4.4 Arterial Blood Gas and Blood Pressure Analysis

The arterial blood gas parameters from Group I and Group II are shown in Tables 4.1 and 4.2, respectively. Data in Group I show a statistically significant increase in PaO_2 (402.3 mm Hg), producing a 7% increase in SaO_2 . Data from Group II were in close agreement with Group I, showing a very similar increase in PaO_2 (401.9 mm Hg), with increase in PaO_2 in the intermediate steps closely approximating the relative change in FiO_2 . A mild but significant increase in the arterial partial pressure of carbon dioxide (PaCO_2) was measured from $\text{FiO}_2 = 0.3$ to 1.0 in Group I (2.3 mm Hg) and Group II (3.2 mm Hg). Mean arterial blood pressure (MABP) (measured in Group I only) and pH were not found to change significantly.

Table 4.1. Arterial Blood Gas Parameters for Normoxia and Hyperoxia in 1.5% Isoflurane Anesthesia (Group I)

FiO_2	pH	PaCO_2 (mm Hg)	PaO_2 (mm Hg)	SaO_2 (%)	MABP (mm Hg)
0.3	7.44 ± 0.03	45.3 ± 1.8	97.0 ± 8.3	92.9 ± 1.3	73.5 ± 4.9
1.0	7.43 ± 0.04	$47.6 \pm 1.6^*$	$499.3 \pm 32.2^*$	$99.9 \pm 0.1^*$	73.9 ± 5.3

* $P < 0.05$ from normoxia.

Table 4.2 Arterial Blood Gas Parameters for Graded Levels of Hyperoxia in 1.5% Isoflurane Anesthesia (Group II)

FiO ₂	pH	PaCO ₂ (mm Hg)	PaO ₂ (mm Hg)	SaO ₂ (%)
0.3	7.45 ± 0.03	44.7 ± 1.2	99.3 ± 11.6	93.0 ± 2.1
0.4	7.44 ± 0.03	45.3 ± 1.0	154.3 ± 13.6	97.7 ± 0.6
0.6	7.44 ± 0.02	46.1 ± 0.8	266.8 ± 16.8	99.4 ± 0.1
0.8	7.44 ± 0.01	46.7 ± 0.6	388.8 ± 13.4	99.8 ± 0.0
1.0	7.43 ± 0.02	47.9 ± 0.8	501.2 ± 23.0	99.9 ± 0.0

4.5 Cerebral Blood Flow Mapping with Correction for T_{1a}

An anatomic dataset from a representative animal from Group I is shown in Fig. 4.3, along with outlines of ROIs used in the analysis of the perfusion maps. Quantitative CBF maps during normoxia and hyperoxia are shown below. A reduction in calculated CBF values in several regions across the brain can be clearly visualized. Correcting for T_{1a} measured during hyperoxia clearly reduced the degree of the differences between normoxia and hyperoxia, but reduced CBF values can still be visualized. To demonstrate the degree of CBF reduction due to hyperoxia in our experimental setup, Fig. 4.4 shows the time course of average ΔM across all the ROIs during the hyperoxic challenges for a

representative animal. The signal intensity of the control image was modulated by the BOLD signal; although the signal change was small due to the short TE, it clearly shows the effects of inhaled oxygen across the experiment. Overlays of the measured reduction (in percent decrease) on anatomical images of the CBF maps corrected for T_{1a} from Group II are shown in Fig. 4.5a. The observed CBF reduction seems to be somewhat regional in nature, with a larger effect in the cortex compared to other regions. The effect of FiO_2 on whole brain CBF measured from Group II animals is shown in Fig. 4.5b. CBF shows a consistently decreasing trend with time and increasing FiO_2 .

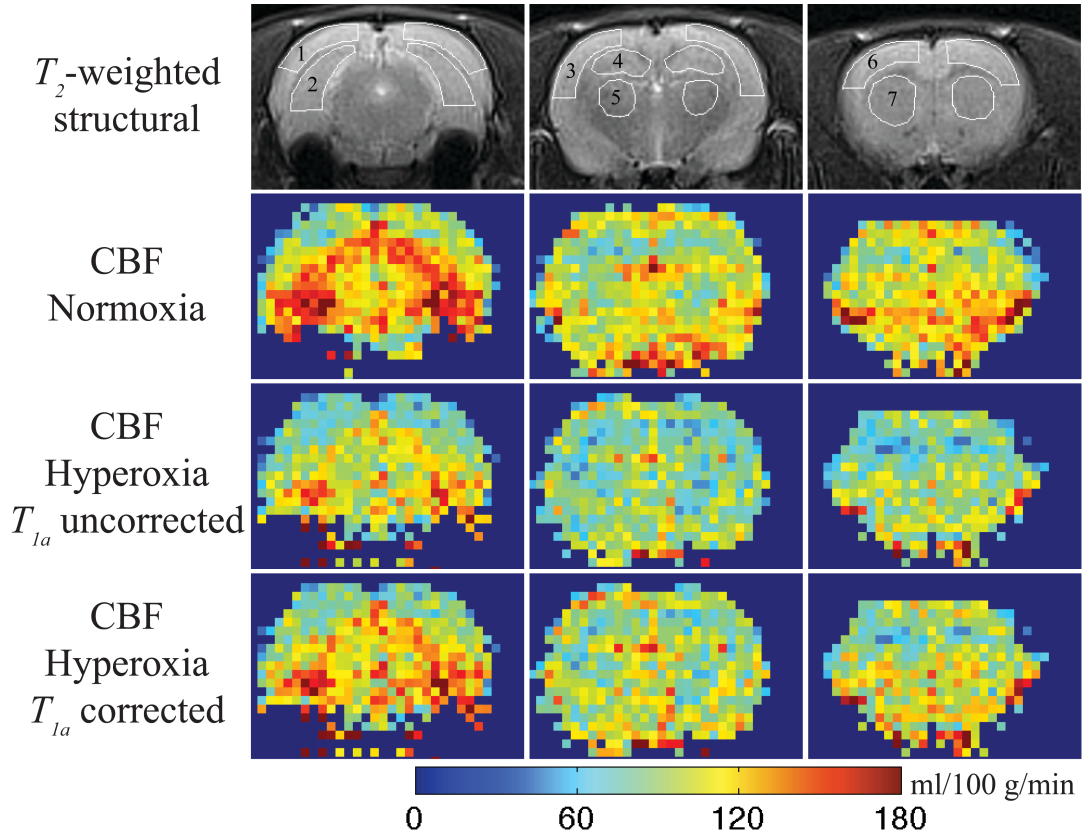


Figure 4.3. T_2 -weighted structural images with ROIs (outlined in white) for analysis of regional CBF values (corresponding columns below), from a representative animal. ROI values from both hemispheres were averaged. In the left column, the inferior slice (bregma -6.5 mm) contains (1) visual/auditory cortex and (2) hippocampus/subiculum. In the middle column, the middle slice (bregma -2.5 mm) contains (3) sensory/auditory cortex, (4) hippocampus, and (5) thalamus. In the right column, the superior slice (bregma 1.5 mm) contains (6) motor/sensory cortex and (7) caudate putamen. CBF values (in ml/100 g/min) in the second row were calculated during normoxia ($\text{FiO}_2 = 0.3$) from Eq. [1] using T_{1a} value measured during normoxia, while CBF values in the in third and fourth row were calculated

during hyperoxia ($\text{FiO}_2 = 1.0$) using the T_{1a} measured during normoxia (uncorrected) and hyperoxia (corrected).

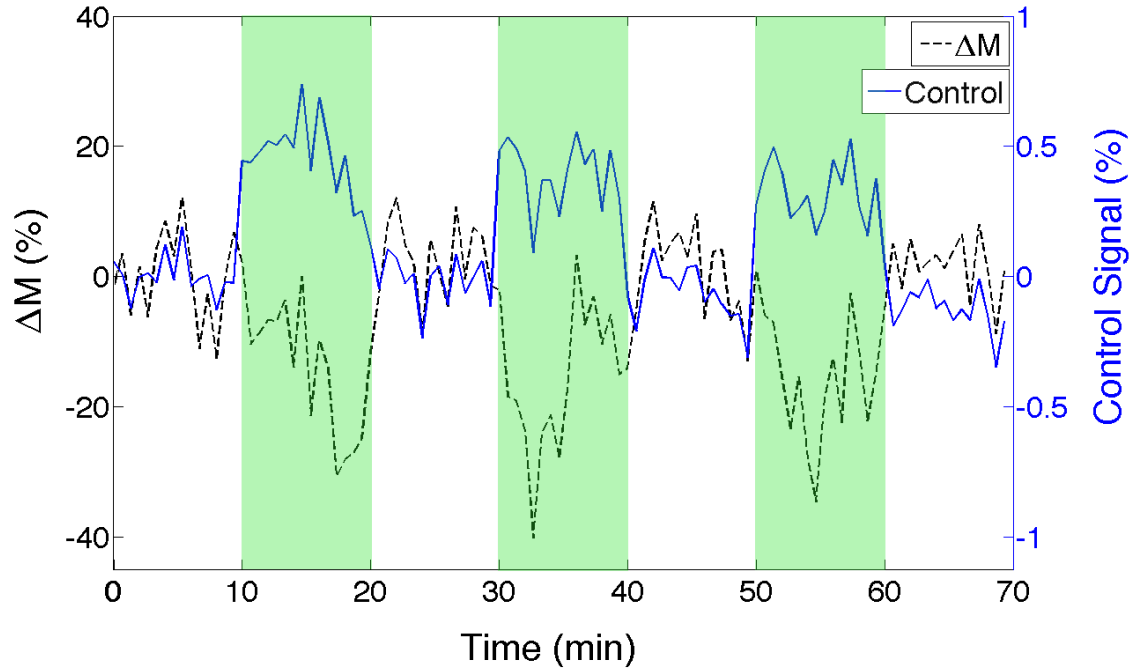
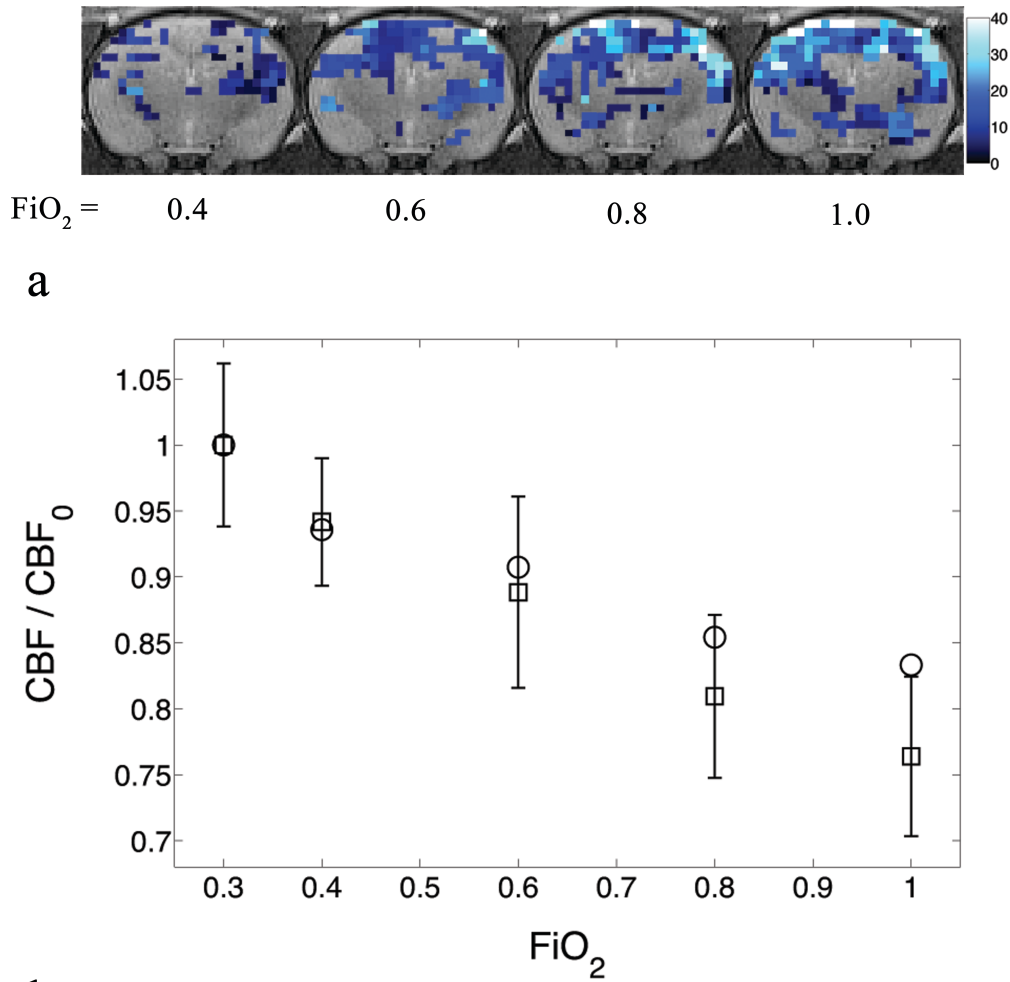


Figure 4.4. Representative signal time course of ΔM (control minus tag) and control image signal intensity during normoxia ($\text{FiO}_2 = 0.3$; white regions) and hyperoxia ($\text{FiO}_2 = 1.0$; green regions). Signal values were calculated at each time point from the mean of all ROIs (see Fig. 4). Units were calculated as the percent difference from starting baseline. Control image signal intensity is increased during hyperoxia due to BOLD response; percent signal change is low ($\sim 0.5\%$) due to the degree of T_2 -weighting ($\text{TE} = 6$ ms).

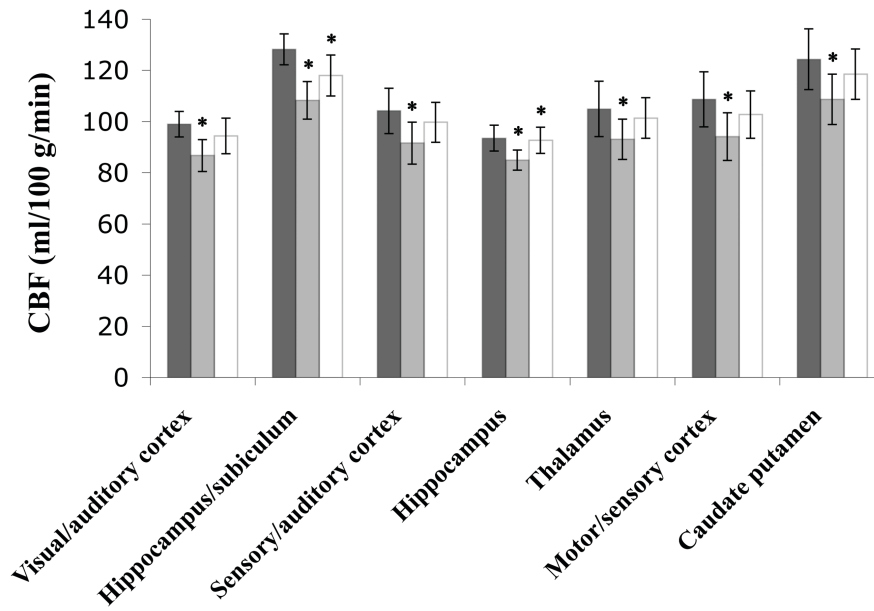


b

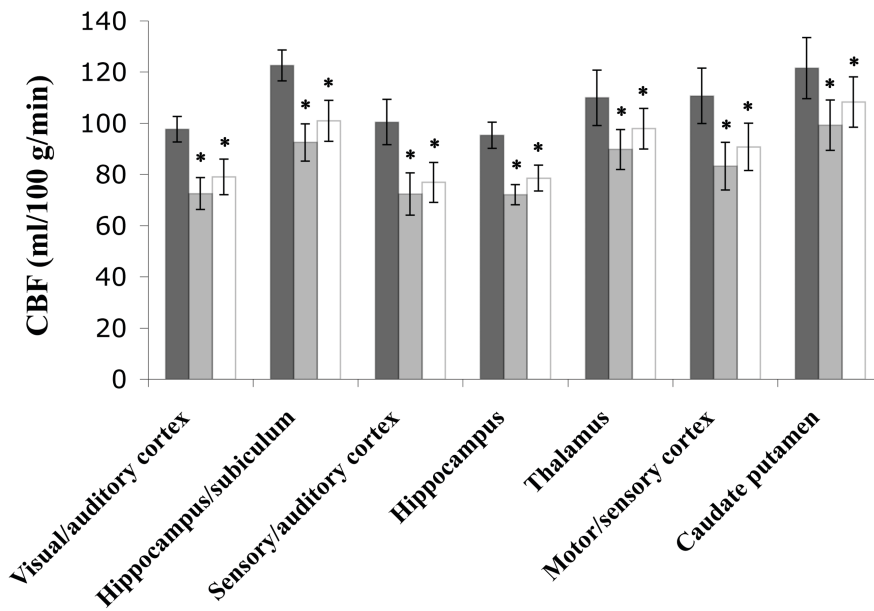
Figure 4.5. Overlays of the measured reduction (% decrease) on anatomical images of the CBF maps from a representative animal (a) and the effect of FiO_2 on whole-brain relative CBF. Both sets of data come from Group II animals. The data shown (a) have been corrected for the per subject change in T_{1a} ; the observed CBF reductions appears to be regional in nature, with the largest effects observed in the cortex. Relative CBF in (b) shows a consistently decreasing trend with time and increasing FiO_2 . The squares and circles represent the data uncorrected and corrected for the change in T_{1a} , respectively. Values are mean \pm SD.

4.6 ROI Analysis of Hyperoxia-Induced CBF Reduction

ROI analysis of mean calculated CBF across animals for normoxia and hyperoxia ($\text{FiO}_2 = 1.0$) in Groups I and II is shown in Figs. 4.6a and b, respectively. CBF was significantly reduced across all ROIs before and after correction for T_{1a} in both Groups I and II, as determined by ANOVA. CBF decreases were larger in the Group II animals, with all regions still showing statistically significant reductions in CBF after correction for T_{1a} . There appeared to be some regional nature to the CBF reduction, particularly in Group II animals where, after correction for T_{1a} , the sensory/auditory cortex region showed a 23.5% reduction, while the caudate putamen region only showed a 10.9% reduction. After T_{1a} correction, whole brain values of CBF exhibited a normoxia to hyperoxia reduction of 109.2 ± 12.9 ml/100 g/min to 103.9 ± 10.4 ml/100 g/min in Group I and 108.3 ± 11.0 ml/100 g/min to 90.2 ± 12.5 ml/100 g/min in Group II. The correction for the change in T_{1a} dominated the Group I correction, accounting for 63% of the increase in the observed reduction in CBF. In Group II, the T_{1a} change contributed significantly less, accounting for 28% of the increase in the observed reduction in CBF.



a



b

Figure 4.6. Mean calculated CBF values (ml/100 g/min) in seven ROIs (both hemispheres; see Fig. 4.3) during normoxia ($\text{FiO}_2 = 0.3$; dark gray bars) and

hyperoxia ($\text{FiO}_2 = 1.0$) uncorrected (light gray bars) and corrected (white bars) for T_{1a} during hyperoxia. Data are were taken from Group I (a) and Group II (b). Values are mean \pm SD. * $P < 0.05$ from normoxia.

4.7 Chapter Discussion

In this study, T_{1a} and quantitative CBF were measured in vivo at 3T during normoxia and hyperoxia using PASL approaches. The measured T_{1a} values were used to correct the calculated CBF in each experimental animal under a brief hyperoxic inhalation and graded hyperoxic inhalation paradigms. As discussed in Chapter 3, the reduction in T_{1a} due to oxygen is rapid and consistent across large differences in the duration of oxygen exposure. The changes in CBF, however, were found to be significantly different depending on the oxygen exposure duration. The longer exposures of the slow, graded hyperoxic inhalation paradigm of Group II produced significantly more reduction in CBF. This is in agreement with established effects of hyperoxia on cerebral blood flow, as the attenuation of effects of nitric oxide effects have been shown to depend on the duration of hyperoxic exposure (50). Overall, the results of this study suggest that the observed reduction in CBF measured by ASL is dominated by T_{1a} reduction during short term inhalation epochs, but physiologic effects become the primary source of the reduction over longer hyperoxic exposures.

Although the measured longitudinal relaxivity of T_{1a} as function of PaO_2 , and therefore the CBF correction, determined in this study were found to be significantly smaller than those used in previous studies (37,46), we have grounds to be confident in the findings of our study. As discussed in Chapter 3, we found that the observed T_{1a} changes of our *in vivo* data very closely approximated the more robust phantom data. Perhaps more significantly, the correction made in this study most likely represents the maximum degree to which the reduction in T_{1a} would decrease the measured CBF reduction. We have assumed that spins measured in the ASL experiment have spent the vast majority of TI (inversion time) in a compartment that approximates arterial blood. However, toward the end of TI, a significant portion of tagged spins will enter the capillary and tissue spaces. In these regions, the change in pO_2 during hyperoxia will be substantially lower (47), yielding a smaller change in T_1 . In addition, in the capillary space, the mild dilution of deoxyhemoglobin is likely to yield a slight increase in T_1 . In order to accurately account for these effects, it will be necessary to develop a model of the average change in pO_2 experienced by the tagged spins over the duration of TI. Such a model would need to incorporate the temporal characteristics of inflowing blood water and describe the relative amount of spins in each tissue compartment as a function of time. For these reasons, the ASL signal model used in this study is not complete, and the effective reduction in the T_1 experienced by the tagged spins is likely to be significantly less than the measured reduction in T_1 of arterial blood. However, the use of this model is important, since it represents the upper bound to which the reduction in CBF measured can be attributed to a reduction in T_1 of the spins measured by the ASL experiment.

Baseline mean values of CBF across the rat brain during normoxia were in close agreement to literature values (93,94). In agreement with previous studies in humans and mechanically ventilated animals (37,46,48,93), a reduction in regional CBF with hyperoxia was observed. The response to brief inhalation epoch was more uniformly global and appeared to demonstrate less regional variance compared to the longer hyperoxic exposure of the graded inhalation. As mentioned above, this may have physiologic foundation, since T_{Ia} changes produce only a global effect, but it remains unclear whether local physiologic effects, like nitric oxide attenuation, exhibit variations that are more regional in nature. Contrary to the results of a previous study of hyperoxia in free-breathing rats that showed a mild increase in CBF (5), we found that CBF consistently decreased with hyperoxia. The presumed source of the increase in CBF in the previous study was mild hypercapnia caused by hyperoxia-induced hypoventilation, and we also observed a slight increase in $p\text{CO}_2$ during hyperoxia. However, very short hyperoxic epochs (~2 min) were used in the previous study (5), which are likely too short to observe the vasoconstrictive effects of hyperoxia (37,48,93). Furthermore, the levels of isoflurane used in the present study were significantly higher (1.15-1.25% versus 1.5-1.8%), and isoflurane is known to substantially suppress the effects of CO_2 on the vasculature (94). We believe these factors explain why the effects of elevated $p\text{O}_2$ on CBF were dominant in the present study. However, the elevation in $p\text{CO}_2$ is a likely confounding factor in this experiment, and if normocapnia was maintained, it is likely that a larger reduction in CBF would have been observed.

In conclusion, simultaneous in vivo measurements of T_{1a} and CBF were performed using PASL approaches during normoxia and hyperoxia in rat brains at 3T under a brief hyperoxic inhalation and graded hyperoxic inhalation paradigms. The results of this study suggest that the measured reduction in CBF using ASL is dominated by T_{1a} reduction during short term inhalation epochs, but physiologic effects become the primary source of the ASL signal reduction for longer hyperoxic exposures. Furthermore, the inter- and intrasubject variability during normoxia and in response to hyperoxia observed in this study underscores the importance of the accurate measurement of T_{1a} in quantitative ASL studies.

Chapter 5: Hyperoxic Calibrated Quantitative fMRI for the Measurement of Regional Cerebral Metabolic Rate of Oxygen in a Hypermetabolic Swine Model

5.1 Overview

The aim of this study is to quantify relative metabolic changes using hyperoxic calibrated BOLD/ASL fMRI in a hypermetabolic swine model. Metabolic changes using this large animal model were previously studied by our group using gas that is isotopically-enriched with $^{17}\text{O}_2$. We sought to cross-validate these measurements with hyperoxic dHb dilution methods of relative metabolism and to compare the results of hyperoxia and hypercapnia calibration methods using this animal model.

5.2 Introduction

Significant progress has been made in developing quantitative approaches to measure relative changes in metabolism in normal brain tissue with MRI, using calibrations of simultaneous BOLD and ASL data with inspired gases (6),(107). Although these studies generally show agreement in producing the same relative changes in CMRO_2 under similar stimuli as compared with quantitative measurements such as PET (107), there have been no studies cross-validating these MRI techniques with simultaneous absolute measurements of metabolism. Part of the reason these studies have not been performed

is the extreme technical difficulty in performing these experiments, as dual-mode PET/MRI scanners have only recently come into existence (108). However, a method measuring absolute metabolic rates using MRI would allow for these simultaneous cross-validation studies to be performed much more easily.

To date, the only MRI methods capable of measuring absolute metabolic rates are those using the inhalation of gas isotopically-enriched with $^{17}\text{O}_2$ (109). These methods work by detecting the increase in the transverse relaxation rate created by (i) exchange modulation of J-coupling between ^{17}O and ^1H in H_2^{17}O formed by the metabolism of $^{17}\text{O}_2$ immediately after its inhalation and (ii) exchange of ^1H between this newly formed H_2^{17}O with H_2^{16}O (3). While extensive studies of $^{17}\text{O}_2$ inhalation have been performed in animal models, human experiments have been limited to small studies by a few groups. This fact is due primarily to regulatory issues, but it is also because of the expense and technical difficulty of the experiment, including the need for rapid delivery and recovery of the exhaled $^{17}\text{O}_2$ gas (3).

Our group has recently developed an approach that is capable of performing $^{17}\text{O}_2$ inhalation experiments in humans using an apparatus to deliver brief $^{17}\text{O}_2$ pulses (110). We tested it with a large animal model of elevated metabolism using 2,4-dinitrophenol (3). This hypermetabolic model in swine was devised to generate a stable metabolic increase across the entire brain by at least a factor of two. By comparison, stimulation of

brain metabolism by other methods such as peripheral motor stimulation are transient, highly localized, and generally increase metabolism by less than 30% (5). In this model, hypermetabolism is induced by administering 2,4-dinitrophenol (DNP), which disrupts the mitochondrial proton gradient that is used by ATP synthase to generate ATP (111). This disruption causes the cell to respond by using additional energy resources to re-establish a normal proton gradient. This additional energy expenditure dramatically increases total metabolism and oxygen consumption. Using these approaches, our group has measured substantial whole brain CMRO₂ increases of approximately 17% per mg/kg DNP in this animal model (3).

In this study, we set out to determine the feasibility of measuring the change in CMRO₂ in this hypermetabolic swine model using simultaneous BOLD and ASL acquisitions calibrated with isometabolic dHb dilution using hyperoxia (6) and hypercapnia (107). The goal of this study was twofold: (1) to cross-validate the results of the change in CMRO₂ with the prior study using ¹⁷O₂ and (2) to compare the results of hyperoxic and hypercapnic calibration methods. To this end, we carried out the experiment in the same manner as the prior ¹⁷O₂ inhalation study and performed an analysis of CMRO₂ at the same time point after administration of the same dose of DNP.

5.3 Materials and Methods

5.3.1 *Animal Preparation*

All experiments performed were part of an approved protocol by our Institutional Animal Care and Use Committee. Juvenile Yorkshire pigs (n=8; 23-30 kg) were anesthetized with an intramuscular injection of ketamine (25 mg/kg), medetomidine (0.1 mg/kg), and glycopyrrolate (0.02 mg/kg). Anesthesia was maintained with a continuous IV infusion of ketamine (20-80 mg/kg/hr) and was increased incrementally if the animal exhibited motion or response to stimuli. Animals were mechanically ventilated through an endotracheal tube using a custom-built precision delivery breathing circuit (110). Diazepam (0.02-0.08 mg/kg) was delivered by IV infusion as needed to reduce any ventilation resistance. Ventilator settings were set at a respiratory rate (RR) of 8-12 breaths per minute with a tidal volume of 20-25 mL/kg and were constantly monitored and adjusted to keep oxygen saturation by pulse oximetry (SpO₂) and end-tidal CO₂ at normal levels (>98% and <40 mm Hg, respectively). After the experiment was completed, all animals were euthanized with pentobarbital administered under anesthesia. Normal temperature ($38 \pm 1^{\circ}\text{C}$) was maintained throughout the experiment with a water warming blanket. To draw arterial blood gases, an arterial catheter was inserted in the medial aspect of the hind limb using ultrasound guidance in the large animal fluoroscopy suite. All blood gas samples were measured using disposable cartridges and a hand-held blood gas analyzer (i-STAT System; Abbott Laboratories, Abbott Park, IL, USA). Arterial oxygen saturation and heart rate were constantly monitored throughout the experiment with a veterinary pulse oximeter (Nonin 8600V, Nonin Medical, Inc.,

Plymouth, MN, USA) attached to the ear. End-tidal CO₂ (EtCO₂) was continuously monitored with a capnograph (Capnostream 20, Oridion Capnography Inc., Needham, MA), which was sampled using a port at the expiratory side of the ventilator close to the mouth.

5.3.2 Preparation and Administration of 2,4-Dinitrophenol

DNP solutions were prepared in the same manner as our group's prior ¹⁷O inhalation studies (109). Briefly, the DNP solution prepared within 1 day of use by combining 2.5 mg/mL of DNP (Sigma-Aldrich D198501) and 5 mg/mL of sodium bicarbonate to 0.9% saline. The solution was brought to approximately 70°C with constant stirring to dissolve all solutes. The solution was then allowed to cool to room temperature and filtered through a 0.1 µm vacuum filter (Millipore SCVPU02RE).

After all gas calibrations (described below) were performed, 9 mg/kg of DNP were administered to the animal by slow IV infusion as described previously (109). Animals were monitored for approximately sixty minutes before euthanasia. Two pigs became very physiologically unstable after DNP injection, so their datasets were removed from the final analysis.

5.3.3 Hyperoxia and Hypercapnia Challenge Paradigms

The swine were given a single, ten minute hyperoxia ($\text{FiO}_2 = 1.0$) and hypercapnia (6% CO_2 in air) challenge in a baseline – stimulation – rest paradigm (5 min baseline, 10 min stimulation, 10 min rest). Data acquired during the first five minutes were discarded to allow time for physiologic adjustments to the new gas condition. At the very end of the gas challenge, an arterial blood gas sample was drawn.

5.3.4 MRI Hardware

All imaging experiments were performed using a whole-body clinical 1.5T MRI scanner (Siemens Sonata; Siemens Healthcare, Erlangen, Germany). RF excitation pulses were transmitted with the built-in scanner body coil. MR signals were received with a custom-built single loop (80 mm ID) receive-only head coil, which was actively decoupled during transmit. The animal was firmly secured to a custom-built head holder with a bite plate to minimize motion during the study. The head coil was firmly fixed close to the brain, over the dorsal aspect of the head.

5.3.5 MRI Sequences

An interleaved BOLD/ASL sequence was implemented to acquire T_2 -weighted images and CBF simultaneously. A single-shot fast spin echo (FSE) readout was used with a pseudocontinuous arterial spin labeling (PCASL) preparation without background suppression (112,113). Although it produces lower BOLD contrast than T_2^* -weighting, a fully-refocused T_2 -weighted FSE sequence was used to produce a very temporally stable signal. The RF refocusing reduces sensitivity to main magnetic field drift, which can be substantial over the long time periods (> 1 hour) used in this experiment. Furthermore, complete RF refocusing of the signal also has the benefit of being insensitive to any B_0 shifts induced by hyperoxia, as discussed in Chapter 2. The PCASL approach uses a rapid pulsed method to produce spatially-varying effective B_1 field along the direction of the artery, similar to continuous ASL. This approach is preferred to the continuous method since it has a superior approach for generating the control image (112), producing higher overall efficiency and signal-to-noise ratios.

The FSE readout parameters were: $TE/TR = 118$ ms/ 4000 ms, $FOV = 180 \times 180$ mm², Matrix = 64×64 , BW = 130 Hz/Px, excitation flip angle = 90° , refocusing flip angle = 180° , slice thickness = 8 mm. PCASL parameters were: labeling duration = 1500 ms, post-label delay = 1000 ms, label plane offset = 60 mm, $B_{1avg} = 1.7$ μ T, $G_{avg} = 6$ mT/m. The PCASL control and tag images were interleaved one-to-one.

5.3.6 BOLD and Arterial Spin Labeling Analysis

All images were motion corrected before analysis with FSL tools (77) using a software package designed to process intramodal MRI time series data (FEAT) (78). PCASL controls were used as the BOLD images. Given that TR is about four to five times the T_1 of tissue at 1.5T, T_1 weighting will be minimal and the images can be considered entirely T_2 -weighted.

The control and tag images were subtracted, and the resulting PCASL ΔM data were converted to CBF according to Eq. 5.1 (114):

$$CBF = \frac{\Delta M}{2 \alpha M_{0a} T_{1a} \left(e^{-\frac{PLD}{T_{1a}}} - e^{-\frac{PLD+\tau}{T_{1a}}} \right) e^{-\frac{TE}{T_{2a}}}} \quad [5.1]$$

where α is the inversion efficiency (assumed to be 0.9), M_{0a} is the equilibrium magnetization of blood, T_{1a} is the longitudinal relaxation time of arterial blood, PLD is the post-label delay time (time between the end of tagging pulse and beginning of the readout), τ is the labeling duration, and T_{2a} is the transverse relaxation time of arterial blood. As discussed in Section 4.3.3, M_{0a} was calculated based on the local magnetization using Eq. [4.3], with $R = 0.98$, $T_{2a} = 200$ ms, and $T_{2LT} = 120$ ms (23). T_{1a} under normoxia was taken to be 1350 ms (21), while the T_{1a} during hyperoxia was determined by the application of Eq. [3.2] based on the discussion in Chapter 3. It was

assumed that relaxivity of both deoxyhemoglobin and molecular oxygen were independent of field strength (21).

Final analysis of the BOLD and ASL data was performed using custom scripts written in MATLAB. Due to the lower Boltzmann distribution, longitudinal relaxation time, and deoxyhemoglobin relaxivity at low field, both the ASL and BOLD data were relatively noisy. Given the limited signal-to-noise ratio of our measurements, we analyzed all values using whole brain regions-of-interest that were manually drawn to cover both the gray and white matter regions. Baseline values were calculated using a five minute average before the stimulation, and stimulation values were a five minute average at the end of the stimulation period. DNP stimulation values were calculated over five minutes and centered at thirty minutes post-DNP administration.

5.3.7 Calculation of Regional Cerebral Metabolic Rate of Oxygen: Hyperoxic and Hypercapnia Calibration Methods

We calculated relative CMRO₂ changes in this study using the formalism introduced by Hoge, et al. (107), which is based on the use of simultaneous BOLD and CBF data. This method requires a known isometabolic dilution of deoxyhemoglobin (dHb). An isometabolic reduction in the concentration of dHb can be achieved with a gas inhalation of hypercapnic or hyperoxic gas. The former dilutes dHb via an increase in flow, while the latter dilutes dHb by raising the oxygen content of arterial blood. To calculate

changes in $CMRO_2$, it is necessary to develop a detailed physical model of the interaction between CBF, CBV, and blood oxygenation their effects on the BOLD signal. A brief derivation is provided below for the models of both hypercapnia and hyperoxia as first shown by Hoge, et al. (107) and Chiarelli, et al. (6).

As discussed previously, the regional concentration of dHb is proportional to the transverse relaxation time:

$$R_{2,tissue} = R_{2,dHb} + R_{2,other} \quad [5.2]$$

As Boxerman et al. (115) have shown, $R_{2,dHb}$ is proportional to the cerebral blood volume and the concentration of venous dHb:

$$R_{2,dHb} = A \cdot CBV \cdot [dHb]_v^\beta \quad [5.3]$$

where A is a constant depending on field strength and local tissue properties; β is a constant between 1 and 2 that depends on average blood volume. Consider a reduction in $R_{2,Hb}$ from dHb dilution secondary to an increase in flow (via CO_2 inhalation). The change in $R_{2,Hb}$ versus non-baseline values can be expressed as:

$$\Delta R_{2,dHb} = A(CBV[dHb]_v^\beta - CBV_0[dHb]_{v_0}^\beta) \quad [5.4]$$

where the subscript ‘0’ defines the baseline steady state. The relationship between the change in $R_{2,Hb}$ and the change in the measured BOLD signals is:

$$\frac{\Delta BOLD}{BOLD} = e^{-TE\Delta R_{2,dHb}} - 1 \quad [5.5]$$

If we assume that changes in $R_{2,Hb}$ are sufficiently small, we can make Eq. [5.5] linear, so that:

$$\frac{\Delta BOLD}{BOLD_0} \simeq -TE \cdot \Delta R_{2,dHb} \quad [5.6]$$

Substitution of Eq. [5.4] into [5.6] yields:

$$\frac{\Delta BOLD}{BOLD_0} \simeq TE \cdot A(CBV_0 [dHb]_{v_0}^\beta - CBV [dHb]_v^\beta) \quad [5.7]$$

Rearranging yields:

$$\frac{\Delta BOLD}{BOLD_0} \simeq TE \cdot A \cdot CBV_0 \cdot [dHb]_{v_0}^\beta \left(1 - \left(\frac{CBV}{CBV_0} \right) \left(\frac{[dHb]_v}{[dHb]_{v_0}} \right)^\beta \right) \quad [5.8]$$

The term $(TE \cdot A \cdot CBV_0 \cdot [dHb]_{v0})$ represents the fractional BOLD attenuation that occurs from the dHb at baseline. Importantly, it also represents the maximum possible BOLD response if all dHb was removed from tissue in its baseline state. For clarity, this constant is expressed as M:

$$M = TE \cdot A \cdot CBV_0 \cdot [dHb]_{v0}^{\beta} \quad [5.9]$$

This model will assume a consistent relationship between the change in CBV and the change in CBF. This relationship is also referred to as the Grubb relationship, where:

$$\frac{CBV}{CBV_0} = \left(\frac{CBF}{CBF_0} \right)^{\alpha} \quad [5.10]$$

where α is a constant equal to approximately 0.38 (116). Based on this relationship, the relative CBV term from Eq. [5.8] can be measured by the change in the relative CBF alone.

If we assume that the arterial blood has a negligible concentration of dHb, then the concentration of dHb in a given tissue volume must be dependent entirely on $CMRO_2$ and CBF such that, according to mass conservation (Fick's principle):

$$[dHb]_v = \frac{1}{4} \frac{CMRO_2}{CBF} \quad [5.11]$$

where the factor of four is due to the fact that one molecular of dHb delivers four O₂ molecules. In the case of isometabolism, the baseline-normalized change in [dHb]_v can be expressed as:

$$\frac{[dHb]_v}{[dHb]_{v_0}} = \frac{CBF_0}{CBF} \quad [5.12]$$

Substituting in Eqs. [5.10] and [5.12] into Eq. [5.8] yields an expression for the change in the BOLD signal from baseline for a given change in the CBF from its baseline at a constant rate of oxygen metabolism:

$$\frac{\Delta BOLD}{BOLD_0} = M \left(1 - \left(\frac{CBF}{CBF_0} \right)^{\alpha - \beta} \right) \quad [5.13]$$

Since α is larger than β , there is a monotonic increase in the BOLD signal with perfusion.

In the case where metabolism is not constant, Eq. [5.12] is not valid, and the following expression must be used instead:

$$\frac{[dHb]_v}{[dHb]_{v_0}} = \left(\frac{CMRO_2}{CMRO_{2,0}} \right) \left(\frac{CBF_0}{CBF} \right) \quad [5.14]$$

When substituting this expression into Eq. [5.8], we get an expression relating the relative BOLD, CBF, and CMRO₂:

$$\frac{\Delta BOLD}{BOLD_0} = M \left(1 - \left(\frac{CMRO_2}{CMRO_{2,0}} \right)^\beta \left(\frac{CBF}{CBF_0} \right)^{\alpha-\beta} \right) \quad [5.15]$$

In this way, we have an expression to relate the change in BOLD and CBF signals to the change in CMRO₂, which depends only on α and β values. We can obtain a value of the calibration factor M by using an isometabolic change in flow, which can be achieved with an increase in the arterial partial pressure of CO₂. However, the accuracy of the calculated M value will primarily depend on whether hypercapnia does, in fact, leave the metabolic rate unchanged.

Since inhaling CO₂ gas for calibration of Eq. [5.15] has its drawbacks, including the potential alteration of metabolism, there has been interest in calculating M with oxygen inhalation. This is known to produce far fewer physiologically effects. Chiarelli et al. outlined a method to accomplish this, which requires the calculation of the relative change in [dHb]_v, as Eq. [5.11] is no longer valid during hyperoxia. To make this measurement, we must know the degree of excess oxygen content in the arterial blood during hyperoxia. We must also make some assumptions about baseline oxygen extraction fraction (OEF), which will be discussed below.

As discussed in Chapter 4, short hyperoxic inhalation epochs produce an approximately 5% decrease in CBF after we correct for reduction in T_{1a} . Therefore, reduction in CBF with hyperoxia will directly affect $[dHb]_v$ change and produce a secondary effect on CBV, both of which must be accounted for. To do this, we must add additional terms to Eq. [5.8]:

$$\frac{\Delta BOLD}{BOLD_0} = M \left(1 - \left(\frac{CBV + \Delta CBV}{CBV_0} \right) \left(\frac{[dHb]_v + \Delta[dHb]_v}{[dHb]_{v_0}} \right)^\beta \right) \quad [5.16]$$

where the additional CBV and $[dHb]_v$ are due to oxygen. Since CBV is not changed by a change in $[dHb]_v$, the additional term is equal to CBV_0 . Noting that:

$$\frac{\Delta[dHb]_v}{[dHb]_{v_0}} = \frac{[dHb]_v}{[dHb]_{v_0}} - 1 \quad [5.17]$$

we can express Eq. [5.8] as:

$$\frac{\Delta BOLD}{BOLD_0} = M \left(1 - \left(\frac{CBF}{CBF_0} \right)^\alpha \left(\frac{[dHb]_v}{[dHb]_{v_0}} + \frac{CBF_0}{CBF} - 1 \right)^\beta \right) \quad [5.18]$$

To calculate the baseline-normalized $[dHb]_v$ we must have knowledge of the arterial blood saturation (SaO_2) and the arterial partial pressure of oxygen (PaO_2). The PaO_2 can either be calculated from the end-tidal oxygen level or directly measured via arterial blood gas. The SaO_2 can then be calculated from that PaO_2 (84), or it can be measured

directly via pulse oximetry. In this study, we calculated SaO_2 with pulse oximetry and PaO_2 with blood gases. The oxygen content of arterial blood can be expressed as:

$$CaO_2 = \phi [Hb] SaO_2 + PaO_2 \varepsilon \quad [5.19]$$

where ϕ is the oxygen carrying capacity of Hb, assumed to be 1.34 mL_{O2}/g_{Hb}, ε is the solubility coefficient of oxygen in blood, assumed to be 0.0031 mL_{O2}/ dL_{blood}/mm Hg (84), and $[Hb]$ is assumed to be 15 g_{Hb} / dL_{blood} (117), in lieu of a direct measurement. The first term represents the amount of oxygen carried by hemoglobin, while the second term is the excess oxygen dissolved in the plasma. The outflow of arterial oxygen to the venous system can be calculated again, analogous to the hypercapnia case above, by assuming that hyperoxia is isometabolic and using Fick's principle:

$$CBF \cdot CVO_2 = CBF \cdot CaO_2 - CBF_0 \cdot CaO_{2,0} \cdot OEF_0 \quad [5.20]$$

where the baseline OEF_0 is assumed to be approximately equal to 0.3 from $^{15}O_2$ -labeled radiotracer studies in humans (117). This is considered to be a good approximation, because while CBF and $CMRO_2$ change across the brain, OEF is remarkably stable (6). Rearranging the terms, we can show:

$$CVO_2 = CBF \cdot CaO_2 - \frac{CaO_{2,0} \cdot OEF_0}{\left(\frac{CBF}{CBF_0} \right)} \quad [5.21]$$

Similar to arterial oxygen content, the venous oxygen content can be expressed as:

$$CvO_2 = \phi [Hb] SvO_2 + PvO_2 \cdot \varepsilon \quad [5.22]$$

Since only a negligible amount of oxygen in venous blood is not bound to Hb (even at high FiO_2), the second term can be ignored so that:

$$SvO_2 = \frac{CvO_2}{\phi \cdot [Hb]} \quad [5.23]$$

The baseline-normalized expression for $[dHb]_v$ can be expressed as a ratio of SvO_2 values:

$$\frac{[dHb]_v}{[dHb]_{v_0}} = \frac{1 - SvO_2}{1 - SvO_{2,0}} \quad [5.24]$$

Again, to summarize, the calibration value M can be determined using hyperoxia by the expression:

$$M = \frac{\frac{\Delta BOLD}{BOLD_0}}{\left(1 - \left(\frac{CBF}{CBF_0} \right)^\alpha \left(\frac{[dHb]_v}{[dHb]_{v_0}} + \frac{CBF_0}{CBF} - 1 \right)^\beta \right)} \quad [5.25]$$

where the baseline-normalized change in CBF is measured and corrected according to the Chapter 4, and baseline-normalized expression for $[dHb]_v$ is calculated as shown above. For the $[dHb]_v$ calculation of the hyperoxia calibration, SaO_2 was determined from the PaO_2 measured by arterial blood gas.

M can also be obtained from hypercapnia calibration according to the expression:

$$M = \frac{\frac{\Delta BOLD}{BOLD_0}}{\left(1 - \left(\frac{CBF}{CBF_0}\right)^{\alpha-\beta}\right)} \quad [5.26]$$

In this study, we assumed that $\alpha = 0.38$ and that $\beta = 1.5$ for both calibrations, in accordance with previous studies (6,107). Both of these expressions for M can be placed in the original equation for calculating the change in $CMRO_2$ proposed by Hoge et al. (107):

$$\left(\frac{CMRO_2}{CMRO_{2,0}}\right) = \left(1 - \frac{\frac{\Delta BOLD}{BOLD_0}}{M}\right)^{1/\beta} \left(\frac{CBF}{CBF_0}\right)^{1-\alpha/\beta} \quad [5.27]$$

Relative changes in $CMRO_2$ were calculated using both hyperoxia and hypercapnia calibrations using custom MATLAB scripts with Eq. [5.27] and the processed BOLD and ASL data (as described above).

5.4 Physiologic Responses to Hyperoxia, Hypercapnia, and DNP

Traces of the end-tidal CO₂ (EtCO₂), pulse oximetry arterial saturation (SpO₂), and heart rate (HR) from a representative animal are shown in Fig. 5.1. During hyperoxia, the SpO₂ clearly rose to complete saturation (99.7 ± 0.1 %). During both hypercapnia and DNP administration, SpO₂ typically stayed above approximately 95%. Hypercapnia caused a substantial increase in EtCO₂ from a baseline of approximately 40 (41.2 ± 3.4 mm Hg) to >60 mm Hg (66.2 ± 4.6 mm Hg). DNP caused an immediate and steady increase in EtCO₂ after infusion. Before DNP injection, HR typically stayed constant at approximately 80 beats per minute (bpm). After DNP injection, HR increased steadily and was approximately 130 bpm thirty minutes after DNP infusion.

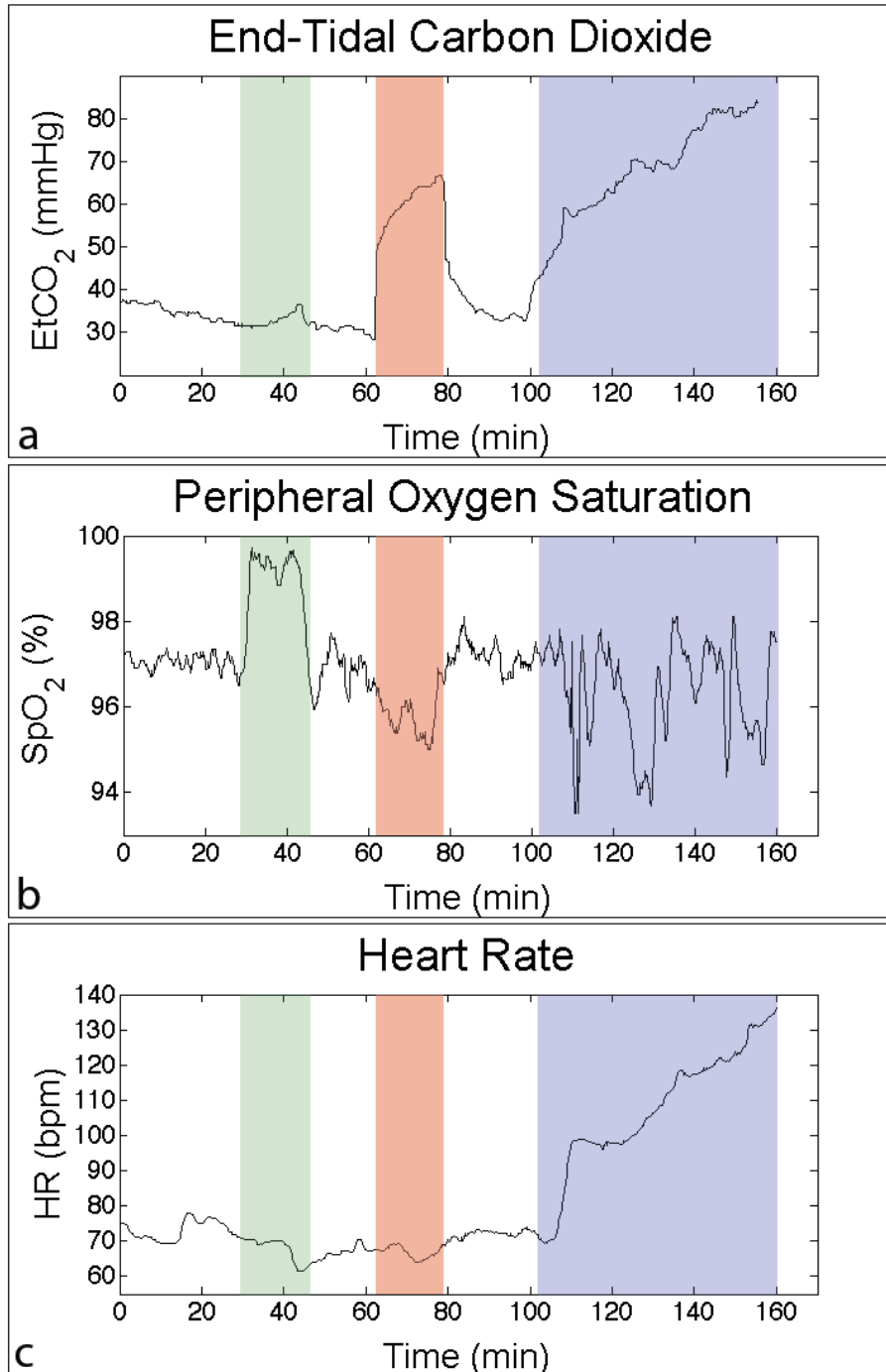


Figure 5.1. Physiological monitoring traces from a representative animal over the entire experiment. The shaded green area represents hyperoxia, the red area represents hypercapnia, and the blue area represents post-DNP injection. End-tidal

CO₂ increased significantly during CO₂ breathing and after DNP injection. Oxygen saturation measured with pulse oximetry was increased to maximum values during hyperoxia, and otherwise remained in the normal physiological range (~93-98%) at all times. There was a consistent trend toward some slight desaturation during hypercapnia and saturation level instability after DNP injection. This is most likely due to the animal resisting mechanical ventilation from high arterial levels of CO₂. Note that oxygen consistently displayed faster wash-in and wash-out times compared to carbon dioxide. The heart rate remained relatively stable during gas challenges, but increased steadily after administering DNP.

5.5 Arterial Blood Gases

The results of the arterial blood draws taken during the experiment are shown in Table 5.1. The blood draws for gas challenges were taken at the very end of the inhalation epoch, while post-DNP draws were taken at approximately thirty minutes after the DNP was infused. All values were tested against the baseline using a two-tailed, paired Student *t*-test. Hyperoxia had a statistically significant increase only in PaO₂, while both hypercapnia and DNP injection produced a significant increase in PaCO₂ and decrease in pH.

Table 5.1. Arterial Blood Gas Parameters for Hyperoxia, Hypercapnia, and Post-DNP Infusion

	pH	pO ₂ (mm Hg)	pCO ₂ (mm Hg)	SaO ₂ (%)
Baseline	7.48 ± 0.08	102 ± 10	38.1 ± 6.6	98.1 ± 1.1
Hyperoxia	7.49 ± 0.12	524 ± 42*	42.2 ± 5.1	100 ± 0*
Hypercapnia	7.31 ± 0.05*	101 ± 9	62.3 ± 4.6*	96.2 ± 2.5
DNP	7.22 ± 0.11*	108 ± 9	81.7 ± 17.2*	96.6 ± 0.9

* $P < 0.05$ from baseline

5.6 BOLD and CBF Responses to Hyperoxia, Hypercapnia, and DNP

Absolute values of CBF were calculated according to Eq. [5.1] and Section 5.3.7. The baseline state across the brain was found to be 39.4 ± 7.8 mL/100 g tissue/min. Relative changes are reported below, as they are the focus of this study. Where indicated, CBF has been corrected for T_{1a} according to the approach in Chapter 4, assuming a baseline $T_{1a} = 1350$ ms (21).

The regional changes from baseline in BOLD and CBF from a representative animal are shown in Fig. 5.2, with overlays onto the structural images. Change in the CBF after correction for T_{1a} was found to be a small reduction, in agreement with findings in Chapter 4. Hyperoxia increased the BOLD response, but less than hypercapnia, which is in agreement with prior studies showing significantly smaller BOLD responses in similar

experiments (38). Hypercapnia increased the CBF by at least a factor of two, which is in agreement with the widely measured relationship of approximately 5% increase in CBF per mm Hg of CO₂ (118). Similar to hypercapnia, DNP showed an increase in flow at thirty minutes that is greater than two-fold, but showed a substantially lower BOLD change. This response is predicted by the biophysical model of the BOLD signal given above. As the CMRO₂ increases substantially with DNP, the local concentration of dHb also increases, decreasing T₂ and counteracting the T₂ increase from the increase in CBV (107).

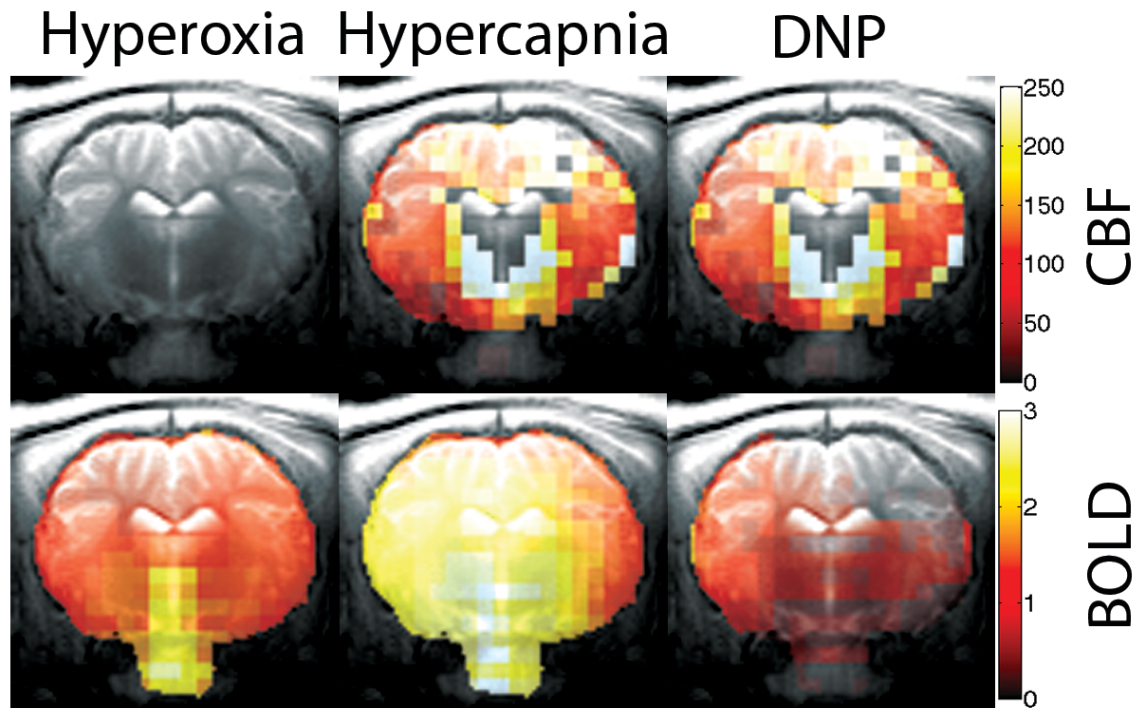


Figure 5.2. Baseline-normalized changes in BOLD and CBF for each experimental condition. The color scales represent the percent signal change from baseline. Hyperoxia showed a mild reduction in CBF and an increase in the BOLD, which was less than that for hypercapnia. Hypercapnia yielded an approximately two-fold increase in CBF. DNP measurements were taken approximately thirty minutes after drug infusion. The CBF increase during DNP was approximately equivalent to that after the ten minute hypercapnia challenge, while the BOLD signal was approximately around baseline levels.

Fig. 5.3 shows MRI signal responses of an ROI that is drawn over the whole brain from a representative animal (same as in Fig. 5.1), using the control and control – tag images.

The relative BOLD (control) signal yielded very good stability over the course of the initial baseline period. This is likely due to the use of the FSE sequence, which is insensitive to B_0 changes, thereby making it much more temporally stable than other acquisition approaches. The BOLD signal increased approximately half as much during hyperoxia as compared to hypercapnia. Again, a slight decrease in the relative CBF (control – tag) images was observed during hyperoxia (Fig. 5.3 data not yet corrected for T_{1a}), although the extent of the change varied across animals. After DNP injection, the BOLD signal initially stayed approximately stable, but then decreased. The CBF signal showed a steady increase from baseline until the animal was euthanized.

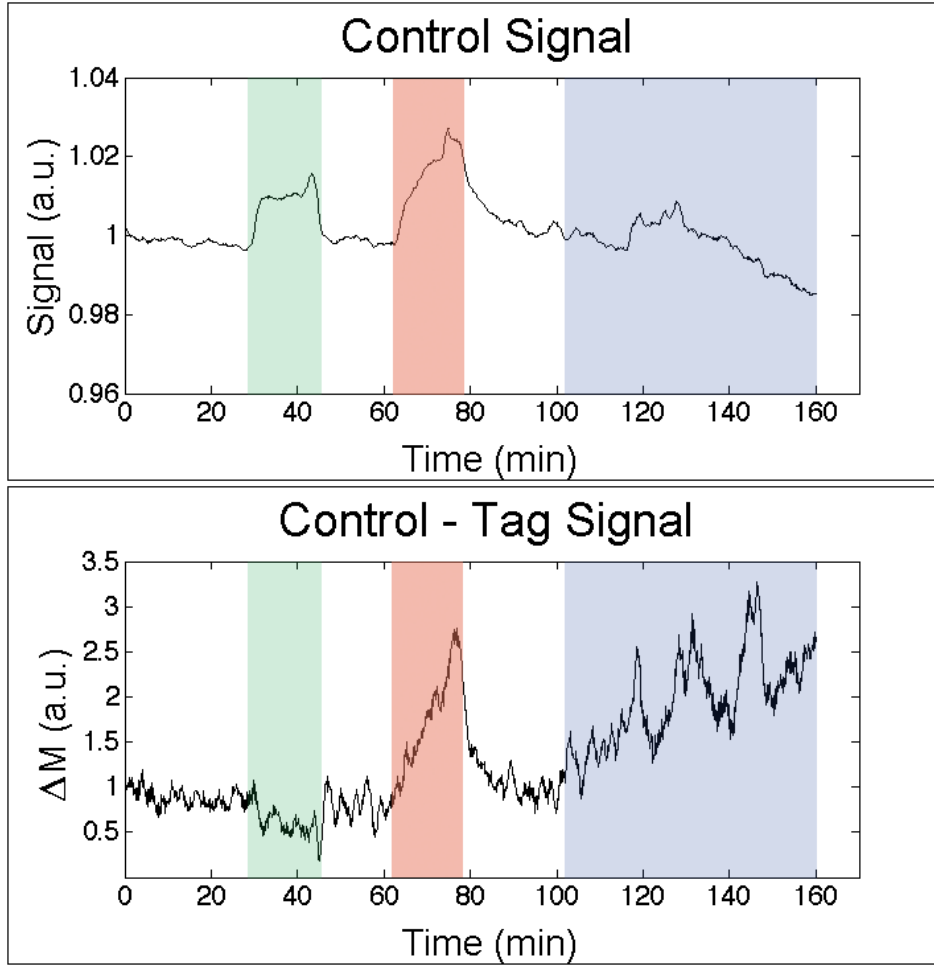


Figure 5.3. MRI signal traces from a whole brain ROI of a representative animal (same animal as Fig. 5.1). The shaded green area represents hyperoxia, the red area represents hypercapnia, and the blue area represents post-DNP injection. Hyperoxia resulted in a BOLD (control) signal increase, while showing a slight decrease in CBF (control – tag). Hypercapnia was increased in both BOLD and CBF. Post-DNP injection, the BOLD signal was stable and then decreased, while the CBF signal constantly increased until the end of the experiment.

5.7 Calculation of the Calibration Factor M for Hyperoxia and Hypercapnia

We calculated a value of M for each animal according to Eqs. [5.25] and [5.26]. The relative changes in the $\Delta\text{BOLD}/\text{BOLD}_0$, CBF/CBF_0 , $[\text{dHb}]_v/[\text{dHb}]_{v0}$ (for hyperoxia only), and M for all experimental animals are shown in Tables 5.2a and 5.2b. As mentioned above, hyperoxia had slightly more than half of the BOLD signal changes compared to hypercapnia. CBF was more than doubled during hypercapnia, while a slight decrease of approximately 5% occurred during hyperoxia after correcting for T_{1a} . The average value of M calculated with hyperoxia was determined to be significantly lower ($P < 0.001$) than that calculated during hypercapnia. The coefficients of variation for M were found to be higher for hyperoxia than hypercapnia.

Table 5.2a. Calculation of Calibration Factor M with Hyperoxia[†]

Animal	CBF/CBF ₀	Δ BOLD/BOLD ₀ (%)	dHb/dHb ₀	M
1	0.945	0.915	0.719	2.05
2	0.918	0.917	0.692	1.81
3	0.952	0.778	0.732	1.84
4	0.978	1.13	0.703	2.61
5	0.875	1.36	0.732	2.71
6	0.943	1.11	0.670	2.18
7	0.982	1.08	0.630	2.08
8	0.949	1.35	0.666	2.66
<i>m</i> ± SD	0.946 ± 0.038	1.13 ± 0.21	0.689 ± 0.041	2.35 ± 0.36
CoV (% <i>m</i> /SD)	4.06	18.8	5.94	15.4

[†]*m* is the mean, SD is standard deviation, and CoV is coefficient of variation

Table 5.2b. Calculation of Calibration Factor M with Hypercapnia[†]

Animal	CBF/CBF ₀	Δ BOLD/BOLD ₀ (%)	M
1	1.90	1.34	2.62
2	2.54	1.90	2.92
3	2.38	1.72	2.78
4	2.45	2.45	3.87
5	2.15	1.91	3.32
6	1.98	1.63	3.05
7	1.99	1.79	3.32
8	1.64	1.34	3.14
$m \pm \text{SD}$	2.10 ± 0.29	1.81 ± 0.37	3.24 ± 0.37
CoV (% m/SD)	14.1	20.5	11.3

[†] m is the mean, SD is standard deviation, and CoV is coefficient of variation

5.8 CMRO₂ Calculation with Hyperoxia and Hypercapnia

Fig. 5.4 shows traces of CMRO₂ changes versus time, immediately after DNP administration of a whole brain ROI for hyperoxia and hypercapnia. The traces were determined according to Eq. [5.27] and the values of M were calculated above. As is visible from the traces, the change in CMRO₂ is similar for both of the calibration methods despite the significant difference in calculated M values.

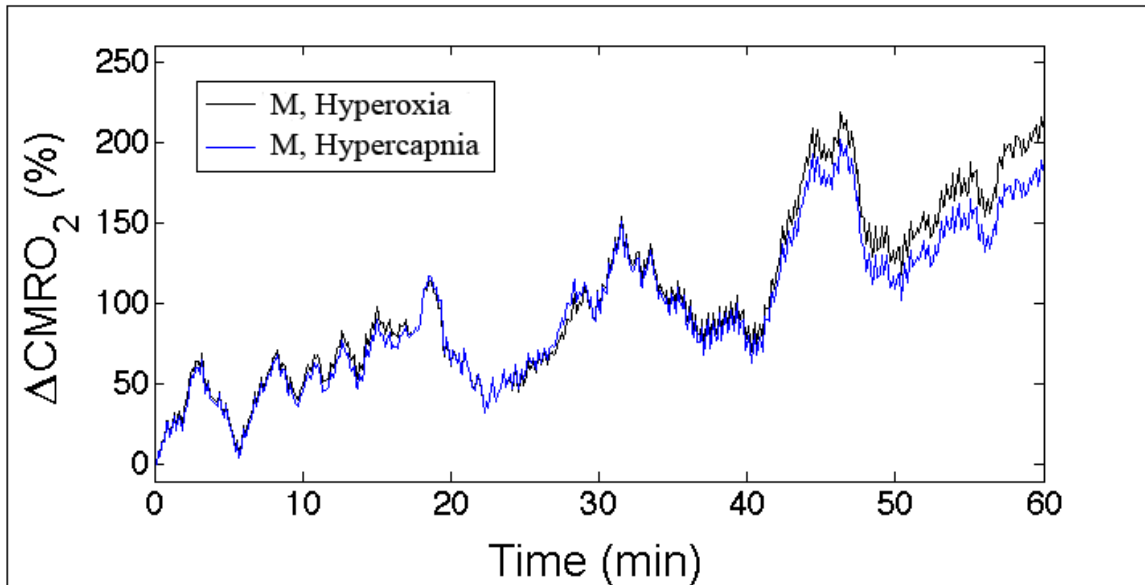


Figure 5.4. CMRO₂ signal traces from a whole brain ROI from a representative animal immediately after DNP infusion. Values are in percent difference from the baseline. The blue trace is calibrated from hyperoxia, and the black trace is from the hypercapnia calibration.

Fig. 5.5 illustrates regional changes in CMRO₂ from a representative animal approximately thirty minutes after DNP with the hyperoxia calibration. Increases in CMRO₂ were visualized mainly around the large increases in cortical flow, as shown in Figure 5.2. The average increase in CMRO₂ approximately thirty minutes after DNP is shown in Table 5.3 for both hyperoxia and hypercapnia calibrations.

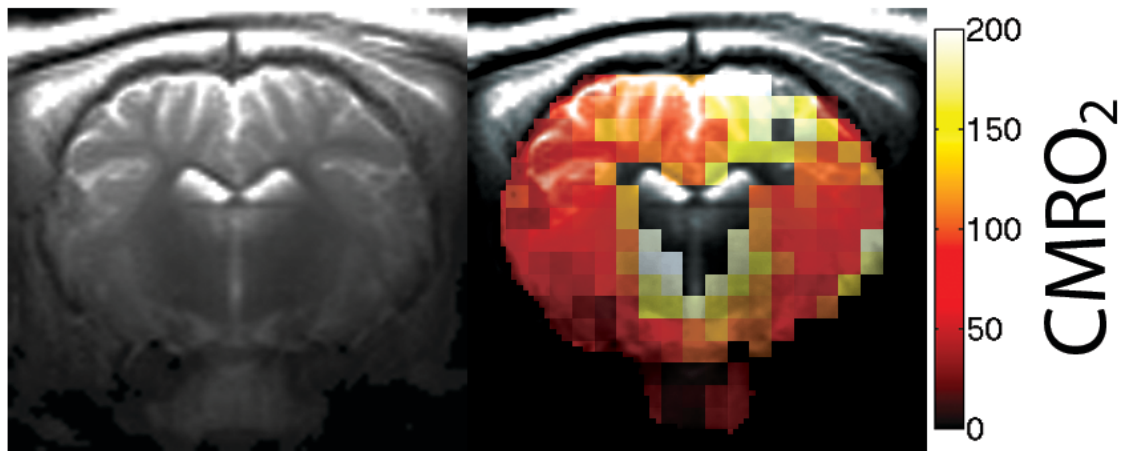


Figure 5.5. CMRO₂ change after thirty minutes of DNP administration in percent increase from baseline. A structural image (left) is shown with an overlay of CMRO₂ increase (right). CMRO₂ appears to increase globally across the brain, with the largest increases occurring in the cortex.

Table 5.3. Calculation of Relative CMRO₂ After DNP Infusion[†]

Animal	CBF/CBF ₀	ΔBOLD/BOLD ₀ (%)	HC CMRO ₂ (%)	HO CMRO ₂ (%)
1	—	—	—	—
2	4.13	0.474	156	135
3	2.51	-0.859	138	156
4	2.50	0.0597	96.4	95.4
5	2.06	-2.49	149	165
6	—	—	—	—
7	2.32	-1.51	141	170
8	3.03	-0.554	155	159
<i>m</i> ± SD	2.76 ± 0.74	0.814 ± 1.076	139 ± 22	147 ± 28

[†]*m* is the mean, SD is standard deviation, and CoV is coefficient of variation

5.9 Chapter Discussion

In this study, the relative CMRO₂ changes in a hypermetabolic swine model were measured using simultaneous BOLD and ASL data, calibrated with isometabolic dHb dilution using inhaled oxygen and carbon dioxide. Using this method, we observed rapid and steady increases in CMRO₂ after administering DNP. The CMRO₂ increase at thirty minutes was found to be slightly less than that from a prior study using ¹⁷O₂ inhalation. However, both methods show an approximate 150% increase in CMRO₂ after thirty minutes of 9 mg/kg DNP.

We found that hyperoxic and hypercapnic approaches to calibration produced very similar final CMRO_2 estimations. However, there were important observed inconsistencies between the methods. First, the calculated M values were significantly different between the methods, a finding consistent with prior studies (6,38,39). The M calculated here were lower for hyperoxia than for hypercapnia, which is same trend seen in prior studies (39). There are several potential explanations for this discrepancy. The difference may be caused by a change in OEF during anesthesia from the assumed value of 0.3. The hyperoxic calculation of M is known to be very sensitive to this parameter (6), and an underestimated OEF will significantly decrease the calculated M value (Eq. [5.20]). Another reason for this difference may be the uncertainty of the value of alpha (39), since hypercapnic calculation M is sensitive to this parameter while the hyperoxic calculation is not.

Second, the coefficients of variation were higher for hyperoxia than for hypercapnia which is the opposite finding compared to prior studies (39). The reason for the difference may lie in the determination of PaO_2 . Prior studies inferred PaO_2 from the end-tidal oxygen concentration (EtO_2), which may yield artifactually consistent results whereas arterial blood gas is far more sensitive and accurate measurement of PaO_2 . Also, since this study involved mechanical ventilation and anesthesia, it may have produced a far more consistent CO_2 increase and response compared to free breathing humans (39).

There are several distinct advantages to using hyperoxia over hypercapnia. First, as we observed in our experiment, oxygen exhibits much faster wash-in and wash-out times as compared to carbon dioxide. This is most likely because excess oxygen has much lower solubility in blood and tissue compartments compared to carbon dioxide (37). Also, in many animals, the wash-in of CO₂ was so slow that the plateau period of MRI signal response was not reached during the ten minute hypercapnic epoch. This is important because a dynamically changing signal can introduce additional error into the calibration. Furthermore, the slow wash-out times mean that hypercapnia requires more rest time to return to physiologic baseline, substantially increasing the time required for the calibration measurement compared to hyperoxia.

Second, there is significantly less controversy in the literature that hyperoxia is isometabolic (5) compared to hypercapnia (119,120). It is crucial to this calibration model that hyperoxia and hypercapnia produce isometabolic changes in dHb concentration; any metabolism changes during the gas inhalation would invalidate a central assumption of the calibration model. Third, the hypercapnia model depends on an accurate measurement of flow changes during gas inhalation. Perfusion measurements with ASL, especially when resolved for regional analysis, are much noisier than BOLD measurements at the same resolution. Since hyperoxia calibration results in only small reductions in flow, it is insensitive to perfusion data and its associated noise. Fourth, compared to hyperoxia, the hypercapnia calibration is much more sensitive to the

assumed value of alpha from the Grubb relationship, which is a matter of controversy (39).

It should be noted that BOLD/ASL data like this is typically used for fMRI experiments with repeated stimulation paradigms at a relatively high frequency (on the order of around a minute). The experiment done here is more challenging, because it uses a single stimulation occurring over a much longer period of time. In this case, the results are much more sensitive to low frequency noise because the data cannot be passed through a high-frequency filter that is typically employed in repeated stimulation paradigm fMRI experiments (38). This limitation was successfully overcome, however, by reducing low frequency noise using a fully refocused FSE acquisition. This dramatically reduced our sensitivity to B_0 shift over time, which is the main source of low frequency noise in standard T_2^* -weighted BOLD experiments.

Although a regional analysis was not performed in this study, studies performed at high field should allow for higher resolution measurements due to higher overall signal-to-noise and higher BOLD contrast. Furthermore, it should be noted that swine have smaller brains for their body size compared to humans or primates. Experiments using an animal with a larger brain would likely allow for a low-resolution regional analysis, even at this field strength.

In conclusion, we have shown that it is feasible to measure CMRO₂ changes using simultaneous BOLD/ASL data, as calibrated with hyperoxia or hypercapnia. Both hyperoxia and hypercapnia calibrations produced very similar CMRO₂ changes, despite producing slightly different measurements of the calibration constant M. Hyperoxia exhibited substantially faster wash-in and wash-out times than hypercapnia, allowing for a much more rapid establishment of equilibrium conditions. Compared to measurements using ¹⁷O₂ inhalation in the same animal model and experimental conditions, we showed comparable increases in CMRO₂ with this calibrated BOLD/ASL method. A superior experiment for cross-validation would be to simultaneously use both methods in the same animals. Due to the need to first determine the feasibility of relative CMRO₂ measurements using calibrated BOLD/ASL data in this context, as well as the expense of ¹⁷O₂ gas, this was not done for these initial studies. However, given that we have shown the feasibility of this approach, this will be the goal of future work. Moreover, the advancements made in this study will allow for more accurate cross-validation studies using simultaneous MRI measurements of CMRO₂ using ¹⁷O₂ and BOLD/ASL data.

Chapter 6: Dependence of Cerebral Blood Flow and Oxygen

Consumption on Hyperoxia-Induced Changes

in the Longitudinal Relaxation Time

6.1 Overview

This chapter aims to develop a biophysical model that relates blood flow and oxygen consumption to the observed T_1 decrease in tissues during hyperoxia. Showing opposite trends compared to hyperoxic effects on R_2 (BOLD), hyperoxic R_1 enhancement increases as CBF increases and metabolism decreases. Using hypercapnia to induce an isometabolic increase in CBF, our model captures effects on R_1 due to this physiological parameter during hyperoxia. Since a comprehensive validation of this model requires measuring hyperoxia as a function of metabolism, future work will focus on altered metabolic states.

6.2 Introduction

Tumor oxygenation and the methods to improve it are important in clinical oncology, because tumor hypoxia modulates radiation responsiveness and limits the effectiveness of radiation therapy (121). Hyperoxic contrast is an attractive method of studying tumor oxygenation because other methods capable of imaging oxygen, such as PET (122), electron paramagnetic resonance imaging (EPRI) (123), and ^{19}F compounds (124), are

much more expensive, are much more difficult to use, and/or are restricted to animal studies. While most studies of tissue lesions, including ischemic stroke and tumors, have focused on the ability of oxygen to dilute dHb and increase T_2 (67,125), there have been several recent studies using hyperoxia primarily to decrease T_1 with dissolved molecular oxygen in order to study tissue oxygen delivery to normal tissue and tumors (31,32,67).

Studies using hyperoxic R_1 enhancement have shown large heterogeneities between tissue types in the ability of oxygen to increase R_1 (32,33). Although qualitative means to explain these differences have been proposed, such as differences in blood flow rate and/or blood volume (31), no attempts have been made to develop a quantitative understanding of the relationship between hyperoxic R_1 enhancement and major physiologic parameters including blood flow, blood volume, and oxygen consumption. An understanding of these relationships is crucial to a more rigorous interpretation of hyperoxic R_1 enhancement and a more rational approach to its clinical use.

In this study, we set out to take the first steps toward developing a detailed quantitative biophysical model of R_1 relaxation enhancement *in vivo*. To accomplish this, we followed a line of reasoning that is similar to the one used in the development of quantitative models of deoxyhemoglobin concentration with hyperoxia (6,39). Our central premise is that dissolved oxygen R_1 contrast within a volume of tissue is dependent solely on the increase in plasma and tissue concentration of oxygen, which in

turn will depend primarily on the volume of blood and its concentration of oxygenated hemoglobin. This is because oxygenated blood is the only place where excess dissolved oxygen can exist. Therefore, we expect to see the increased hyperoxic R_1 enhancement where either blood volume or the concentration of oxygenated hemoglobin is elevated.

Although we focus our study on measurements made in the cerebral tissue (CBF, CBV, and $CMRO_2$), basic conclusions of our biophysical model could be applied to any tissue type exhibiting a similar flow, volume, and oxygen consumption relationship. We tested this model using an isometabolic increase in CBF using hypercapnia. To complete a test of this model, it will also be necessary to study the relationship of R_1 enhancement to changes in CBF and $CMRO_2$, examining whether they differ from the CBF response alone.

6.3 Theory

The biophysical model first developed by Hoge, et al. (107) establishes a relationship between R_2 , CBF and $CMRO_2$ based on the expected changes in dHb concentration and CBV. In a similar manner, we have attempted to produce a quantitative model relating R_1 changes during oxygen inhalation to CBF and $CMRO_2$, based on the expected change in oxyhemoglobin concentration (HbO_2) and CBV. Following a similar line of reasoning to Hoge, et al. (107), we developed an approach to determine the amount and distribution

of molecular oxygen in tissues. We can consider the longitudinal relaxation observed in tissues to be the sum of the components of R_1 caused by molecular oxygen and a contribution caused by other sources:

$$R_{1,tissue} = R_{1,O_2} + R_{1,other} \quad [6.1]$$

It is crucial to this model that we can describe an accurate relationship between the steady-state R_1 contribution of oxygen and the underlying physiological parameters. We argue that we can accurately model the effect of oxygen in following way:

$$R_{1,O_2} = r_{O_2} \cdot PaO_2 \cdot CBV \cdot [HbO_2] \cdot \lambda \quad [6.2]$$

where r_{O_2} is the relaxivity of molecular oxygen ($s^{-1} \text{ mm Hg}^{-1}$) and λ is a tissue specific constant relating the concentration of oxygen in the blood to its concentration in tissue. The constant λ will depend on several physical processes, including the ability of oxygen to diffuse into tissue and its absorption by dHb. Although it does not represent a complete physical picture, we argue that this relationship is approximately accurate, since the dominant source of molecular oxygen in tissues is from the plasma of oxygenated blood.

If we increase the concentration of oxygen only in the arterial blood, and we assume no changes in the CBV, CBF, $CMRO_2$, then:

$$\Delta R_{1,oxy} \simeq r_{0_2} \cdot CBV \cdot [HbO_2] \cdot \lambda \cdot PaO_{2,0} \cdot \left(\frac{PaO_2}{PaO_{2,0}} - 1 \right) \quad [6.3]$$

where the subscript ‘0’ takes its normal meaning as the initial state. We expect this quantity to be positive, since adding oxygen will reduce T_1 . It should be pointed out that this is only approximately correct for a few reasons. First, the excess oxygen will increase the concentration of HbO_2 . However, this change will be small under hyperoxic inhalation and only have a small effect on the measured R_1 . The contributions of local blood volume and λ are expected to dominate over the influence of HbO_2 in this context. Second, this treatment ignores the potential effect of dHb concentration on R_1 . The dilution of dHb is expected to decrease R_1 , because dHb is paramagnetic. However, this effect is again expected to be small in relation to the increase in R_1 from oxygen in the blood and tissue. Third, any the reduction in CBF during hyperoxia is also ignored, as the small effects it may have on R_1 through changes in CBV or $[HbO_2]$ are also dominated by the effects of dissolved oxygen.

We now want to relate the change in R_1 that occurs at a single hyperoxic inhalation where CBV, CBF, and $CMRO_2$ are held constant versus when these parameters are changed. We will refer to this process as $\Delta\Delta R_1$, since we are comparing the change (at different

physiological conditions) of the change (at the same physiological conditions with hyperoxia) in R_1 :

$$\Delta\Delta R_1 = r_{O_2} \cdot CBV_0 \cdot [HbO_2]_0 \cdot \lambda \cdot PaO_{2,0} \cdot \left(\left(\frac{CBV}{CBV_0} \right) \left(\frac{[HbO_2]}{[HbO_2]_0} \right) - 1 \right) \left(\frac{PaO_2}{PaO_{2,0}} - 1 \right) \quad [6.4]$$

It is important to remember that the fundamental measurement is ΔR_1 , which represents the difference in R_1 due to hyperoxia alone, without other changes. $\Delta\Delta R_1$ is the change in ΔR_1 , not at different levels of hyperoxia, but at different physiological conditions.

Similar to Eq. [5.11], if we assume a steady-state and Fick's principle, there exists a relationship between the local concentration of HbO_2 , $CMRO_2$, and CBF:

$$\frac{1}{[HbO_2]} = \frac{1}{4} \frac{CMRO_2}{CBF} \quad [6.5]$$

If we assume that the $CMRO_2$ does not change, then we can express the ratio of $[HbO_2]$ as:

$$\left(\frac{[HbO_2]}{[HbO_2]_0} \right) = \left(\frac{CBF}{CBF_0} \right) \quad [6.6]$$

and if we also assume Grubb's relationship (Eq. [5.10]), we can rewrite Eq. [6.4] as:

$$\Delta\Delta R_1 = E \cdot \left(\left(\frac{CBF}{CBF_0} \right)^{\alpha+1} - 1 \right) \left(\frac{PaO_2}{PaO_{2,0}} - 1 \right) \quad [6.7]$$

where E is:

$$E = r_{0_2} \cdot CBV_0 \cdot [HbO_2]_0 \cdot \lambda \cdot PaO_{2,0} \quad [6.8]$$

In the more general case where $CMRO_2$ is not constant, then Eq. [6.6] must be replaced with:

$$\left(\frac{[HbO_2]}{[HbO_2]_0} \right) = \left(\frac{CMRO_{2,0}}{CMRO_2} \right) \left(\frac{CBF}{CBF_0} \right) \quad [6.9]$$

Using Eq. [6.9], we can rewrite Eq. [6.7] to include the influence of $CMRO_2$:

$$\Delta\Delta R_1 = E \cdot \left(\left(\frac{CMRO_{2,0}}{CMRO_2} \right) \left(\frac{CBF}{CBF_0} \right)^{\alpha+1} - 1 \right) \left(\frac{PaO_2}{PaO_{2,0}} - 1 \right) \quad [6.10]$$

From studying Eq. [6.10], we can see that the behavior of change in R_1 is different than that observed for BOLD contrast during hyperoxia. In BOLD-modulated studies using hyperoxia, the degree of R_2 contrast that can be generated is directly proportional to the concentration of dHb in the voxel. As $CMRO_2$ increases or CBF decreases, the concentration of dHb will increase, as will the ability to generate BOLD contrast with

hyperoxia. With R_1 contrast, the opposite occurs, since the degree of contrast that can be generated depends on the concentration of HbO_2 . As CMRO_2 decreases or CBF increases, the degree of R_1 contrast generated with hyperoxia will also increase.

The relationships between ΔR_1 , CBF, and CMRO_2 as derived in Eq. [6.10] are illustrated in Fig. 6.1. It was assumed that the $(\text{PaO}_2/\text{PaO}_{2,0}) = 4$ in all cases. For the same CMRO_2 , an increase in the relative CBF increases the R_1 contrast from hyperoxia inhalation. Also, as can be seen from Eq. [6.10], this behavior is not asymptotic, since an increase in CBF increases the CBV and $[\text{HbO}_2]$ continuously. However, there is a physiological limit of CBV increases and $[\text{HbO}_2]$ that can occur in tissue, so this relationship will only hold over a certain set of physiologically determined bounds. For increases in CMRO_2 , we expect the concentration of $[\text{HbO}_2]$ to be reduced, which reduces the sensitivity of R_1 contrast. As CMRO_2 decreases for the same CBF, there will be increased concentrations of $[\text{HbO}_2]$, increasing the sensitivity of R_1 contrast. Again, this is also subject to a physiological limit, since there is a point beyond which no increase in $[\text{HbO}_2]$ will occur.

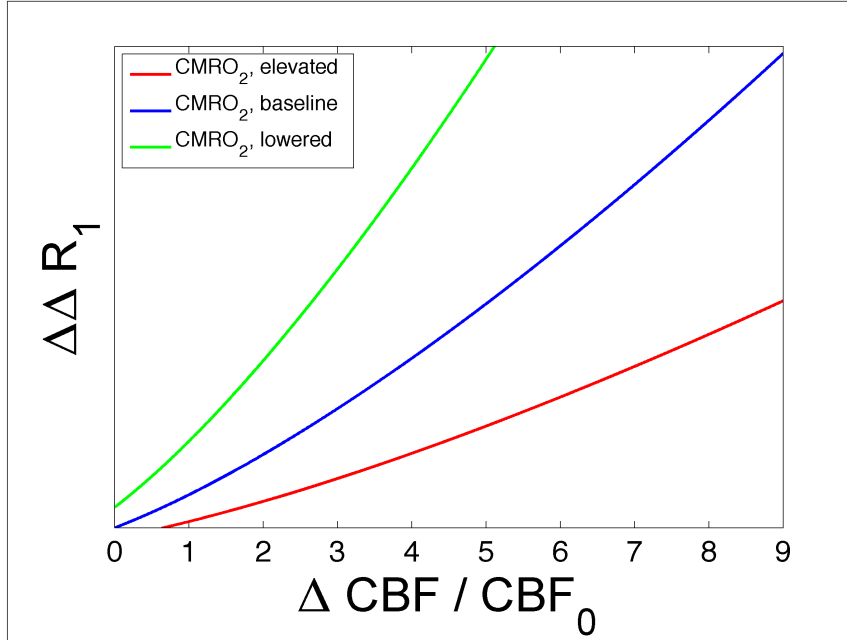


Figure 6.1. The relationships between $\Delta\Delta R_1$, CBF, and CMRO_2 as derived by Eq. [6.10]. There is increased hyperoxia-induced R_1 contrast at higher flow rates and lower levels of CMRO_2 .

6.4 Materials and Methods

The main purpose of this study was to determine if our model of hyperoxia-induced changes in T_1 accurately describes the contrast *in vivo*. We set out to measure the effect of an isometabolic increase in CBF using hypercapnia on the measured R_1 contrast. If our model is correct, we expect to see an approximately linear change in $\Delta\Delta R_1$ versus CBF.

6.4.1 Animals

All experiments performed were part of an approved protocol by our Institutional Animal Care and Use Committee. All data were obtained on adult male Sprague-Dawley rats (n=7; 370-440 g; Charles River, MA, USA). Inhalation anesthesia was induced and maintained in the same manner as described in Section 3.3.2. To ensure that physiologic stability was maintained and to prevent oxygen desaturation, animals were maintained with a minimum FiO_2 of 0.3 (normoxia in this study). Gases were delivered and altered, temperature was maintained constant, and head movement was restricted as described in Chapter 3.

6.4.2 Hyperoxia and Hypercapnia Inhalation Challenge Paradigms

To generate an isometabolic increase in CMRO_2 , animals were ventilated in a steady-state manner with increasing levels of hypercapnia. Starting at with normoxia, animals were ventilated with 5%, 10%, 15%, and 20% CO_2 to generate four increased isometabolic levels of perfusion. Five minutes was allowed after switching hypercapnia levels before data was collected to allow for physiological adjustment to the new gas condition. During each of these steady state levels of hypercapnia, two oxygen challenges from $\text{FiO}_2=0.3$ to 0.8 were delivered in a baseline (5 min) – stimulation (10 min) – rest paradigm. In this way, we sought to increase the arterial partial pressure of oxygen by approximately the same amount for each hypercapnic epoch. Data from the first two minutes of the oxygen challenge were discarded to allow time for the equilibrium of oxygen wash-in.

6.4.3 MRI Hardware

All imaging experiments were performed using a whole-body clinical 3T MRI scanner (Siemens Trio; Siemens Healthcare, Erlangen, Germany) as in Chapter 3.

6.4.4 Measurement of CBF During Hypercapnia

We assumed that the brief hyperoxia inhalation epochs would not cause significant decreases in CBF based on our prior work as outlined in Chapter 4. Furthermore, changes in CBF due to hypercapnia were expected to dominate these changes, making the correction of CBF during hyperoxia insignificant in this context. CBF was measured for a six minute period before and after two oxygen challenges. CBF values were measured using the PICORE-Q2TIPS method with a FSE readout as outlined in Section 4.3.3, with the only difference being that we used a higher spatial resolution single-slice FSE readout here, which also improved temporal resolution. This approach has the advantage of minimizing sensitivity to transit time, which is particularly important in this case since transit time will decrease substantially at higher flow rates. The imaging parameters were: $TI_1 = 900$ ms, $TI_{1S} = 1475$ ms, $TI_2 = 1500$ ms, $TE/TR = 21/4000$ ms, slice thickness = 2 mm, FOV = 40×40 mm, matrix size = 128×128 , and partial Fourier factor = 5/8.

6.4.5 Measurement of the Longitudinal Relaxation Time

The longitudinal relaxation time was measured with a single-slice fast gradient echo Look-Locker technique (also referred to as snapshot-FLASH (30)). A 15 ms adiabatic inversion pulse was used to invert the spins and was followed by fifteen low-angle fast gradient echo readouts each lasting approximately 400 ms each and 1500 ms for the signal to return completely to equilibrium. Magnitude and phase images were collected to allow for a zero-crossing fit. The slice was co-localized to the ASL slice and the sequence parameters were: flip angle = 4^0 , slice thickness = 2 mm, FOV = 40×40 mm, matrix size = 64×64 , TE/TR: 2.2/400 ms, BW: 260 Hz/Px, and Look-Locker repetition time = 8000 ms.

6.4.6 Data Analysis

All images were analyzed using routines and scripts written in MATLAB (MathWorks, Inc.). Relative CBF maps were generated for each hypercapnic gas condition according to Eq. [4.1]. We did not calculate absolute CBF values since only the relative changes in CBF were important for this study. We calculated T_1 values for each Look-Locker dataset according to the following equation:

$$M_z(t) = A - B \cdot e^{-t/T_1^*} \quad [6.11]$$

where T_1 can be calculated according to (126):

$$T_1 = T_1^* \left(\frac{B}{A} - 1 \right) \quad [6.12]$$

M_z was considered to have a positive or negative value depending on its relative phase. Look-Locker images were averaged for normoxia and hyperoxia at each level of hypercapnia. Per voxel T_1 fits were performed on these data. Using the CBF maps, a ROI was manually drawn to include the whole brain. Using these ROIs, we calculated whole brain change in R_1 between normoxia and hyperoxia. We calculated whole brain values primarily due to the low resolution of our T_1 data. We determined whole brain values for CBF using these same ROIs.

6.5 Cerebral Blood Flow versus Hypercapnia Level

Relative values of cerebral blood flow were calculated according to Eq. [4.1] and Section 4.3.3 and are shown in Fig. 6.2. The single slice acquisition improved signal-to-noise per unit time over previously acquired maps (Chapter 4), allowing for good regional analysis of CBF. Global increases in CBF were observed, with the largest increases occurring in the cortex, as expected. CBF increased approximately monotonically with the concentration of inspired CO_2 , without reaching a plateau. Hypercapnia increased CBF by $27 \pm 12 \%$, $63 \pm 14 \%$, $94 \pm 15 \%$, and $118 \pm 17 \%$, for 5%, 10%, 15%, and 20% CO_2 inhalations, respectively.

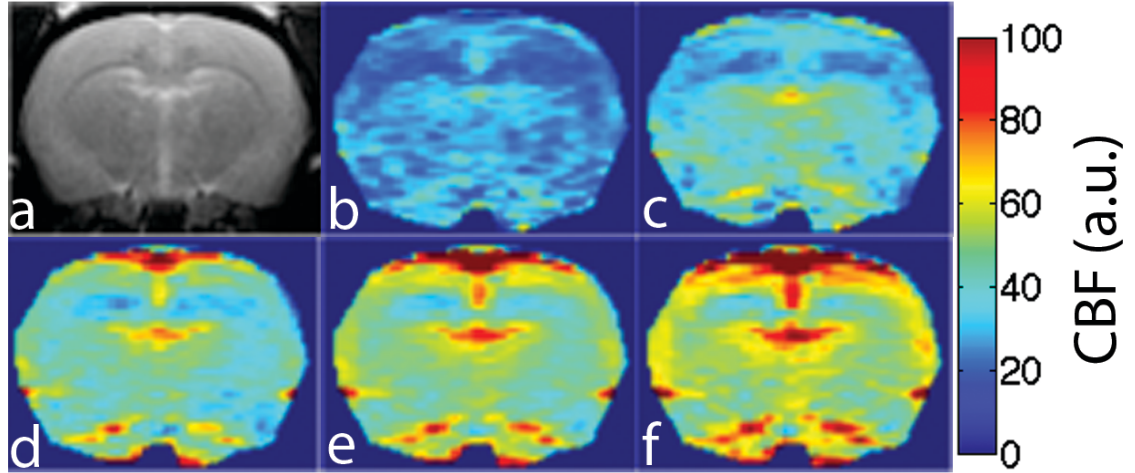


Figure 6.2. Relative CBF (in arbitrary units) at each hypercapnia level from a representative animal with a co-registered structural image (a). CBF maps correspond to baseline (b), 5% (c), 10% (d), 15% (e), and 20% (f) CO₂ inhalation.

6.6 T₁ Mapping

An example quantitative T₁ map calculated according to Eqs. [6.11] and [6.12] is shown in Fig. 6.3. This map was acquired during normocapnia and normoxia; T₁ values of 1200 to 1300 ms measured in the cortex are in agreement with published values (127,128). However, note that the noise for T₁ maps was substantially higher than for the ASL data, compromising our ability to perform regional analyses of the change in T₁ during hyperoxia.

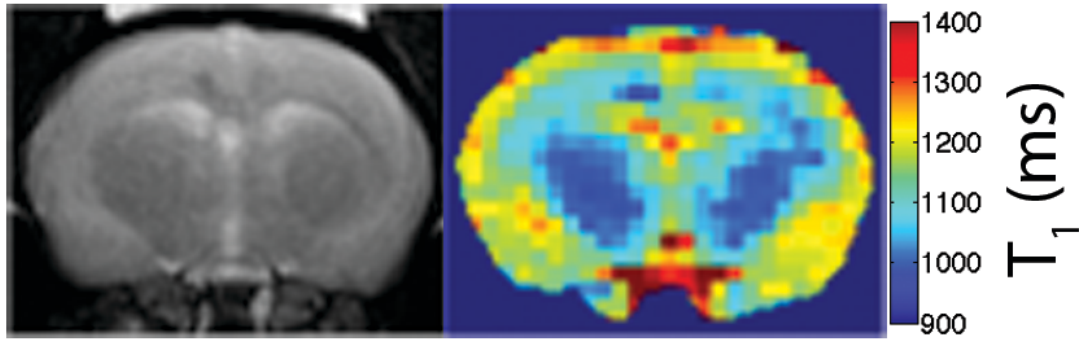


Figure 6.3. Quantitative T_1 map from a representative animal (right) with a co-registered structural image (left). T_1 maps were significantly noisier than CBF maps, but allowed for visualization of regional T_1 values.

6.7 Hyperoxia-Induced R_1 versus CBF

At baseline, oxygen inhalation induced a change in R_1 from baseline by approximately $7.2 \pm 1.8 \times 10^{-3} \text{ s}^{-1}$. Based on our previously determined relaxivity of oxygen as $1.61 \times 10^{-4} \text{ s}^{-1} \text{ mm Hg}^{-1}$, this change seems reasonable, since it is approximately 10% of the change we expected to measure in the arterial blood for an increase in PaO_2 from 100 mm Hg to 500 mm Hg. The ΔR_1 of hyperoxia was determined to be $10.2 \pm 2.1 \times 10^{-3}$, $14.4 \pm 1.5 \times 10^{-3}$, $18.2 \pm 1.9 \times 10^{-3}$, and $21.5 \pm 2.4 \times 10^{-3} \text{ s}^{-1}$ for 5%, 10%, 15%, and 20% CO_2 inhalations, respectively. Using previously measured oxygen relaxivity, we can determine that partial pressure of oxygen increased during hyperoxia by 43, 63, 89, 113, and 133 mm Hg for the baseline state and 5%, 10%, 15%, and 20% CO_2 inhalations, respectively. The trace of $\Delta \Delta R_1$ versus the percent change in CBF is shown in Fig. 6.4. A fit to the model using Eq. [6.7] showed very close agreement to the experimental data.

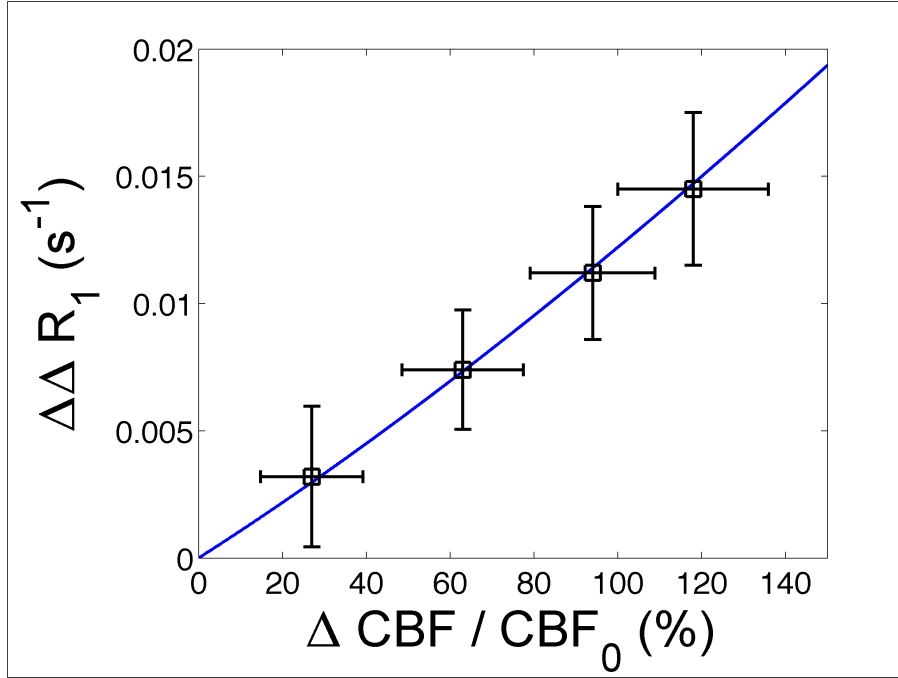


Figure 6.4. The change in hyperoxic longitudinal relaxation enhancement ($\Delta\Delta R_1$) versus relative change in the CBF (% increase from baseline). $\Delta\Delta R_1$ data appears to increase monotonically with CBF, and shows close agreement the proposed biophysical model.

6.8 Chapter Discussion

In this work, we have developed a biophysical model relating CBF, CBV, and CMRO₂ to the hyperoxic R₁ enhancement. Measurements made during an isometabolic increase in CMRO₂ were in close agreement to our model. Furthermore, we can conclude from this study that increasing the blood flow does increase the amount of excess oxygen delivered to tissues. This is an important finding since the relationship between tissue flow and oxygenation enhancement with hyperoxia is still somewhat controversial (31). Although this does not recommend the use of CO₂ for all tumors, as it does not vasodilate in all types of cancerous tissue, it highlights the importance of increasing blood flow to maximize tumor oxygenation.

It is important to note that the behavior of hyperoxic R₁ contrast is the opposite of hyperoxic R₂ (BOLD) contrast. As CMRO₂ increases at the same CBF, we expect the sensitivity of BOLD contrast to increase because the deoxyhemoglobin concentration increases (see Eq. [5.27]). Also, as CBF decreases at the same CMRO₂, we expect to see BOLD contrast sensitivity increase, since that will also increase deoxyhemoglobin concentration. In this way, in relation to physiological conditions, R₁ provides contrast that is complementary in sensitivity to BOLD.

To test our model completely, the response of R_1 to changes in CBF and $CMRO_2$ also should be examined. The model predicts that a decrease in metabolism will also increase the measured R_1 contrast. There are several ways to accomplish this using our current animal model, but the easiest protocol might be to induce moderate hypothermia, which is known to significantly decrease aerobic metabolism (129,130). The same experiment performed here could then be conducted during hypothermia, and, if our model is correct, the relationship between ΔR_1 and CBF should show a higher slope.

If our hypothesis is correct, this model also provides further explanatory power for why hyperoxic R_1 contrast is higher in some tumor regions. Tumors often undergo a switch to increased anaerobic metabolism as part of their path to malignancy (131). As tumors consume less oxygen, the model predicts that R_1 contrast will also increase due to higher concentrations of oxygenated hemoglobin. This can explain why significant hyperoxic R_1 enhancement occurs in some tumor regions despite relatively low levels of flow (33). Our model suggests that since these regions exhibit significantly lower aerobic metabolism, they may still show significant hyperoxic R_1 enhancement despite lower blood flow to the region.

It is important to note that the Bohr effect, which decreases the affinity of hemoglobin for oxygen at higher CO_2 levels, may be responsible for at least some of the observed increases in hyperoxic R_1 enhancement. If there is less oxygen bound to hemoglobin in

the tissue, we expect to see larger increases in R_1 enhancement due to the increase in dissolved oxygen. Unfortunately, we cannot determine how much of our observations are due to this effect. To eliminate the effect of Bohr shift on this experiment would require the use of another arterial vasodilator that does not affect tissue pH or interact with hemoglobin.

In conclusion, this study represents the first steps toward a complete biophysical model of the relationship between hyperoxic R_1 enhancement and blood flow, blood volume, and metabolism. The model shows that hyperoxic R_1 enhancement is expected to increase with higher blood volume, blood flow, and decreased tissue oxygen consumption, which is the opposite effect expected with BOLD contrast, providing complementary sensitivity in relation to physiological conditions. We have shown that this model provides an accurate description of the relationship between hyperoxic R_1 enhancement and isometabolic increases in CBF. A comprehensive test of this model will require examining the relationship of CBF and R_1 relaxation in the setting of altered metabolism.

Chapter 7: Summary and Future Directions

7.1 Future Directions

Although we have already mentioned several important future directions for this work in the preceding chapters, we summarize and expand on these thoughts here and supplement our discussion with some additional considerations.

The work in Chapter 2 of hyperoxic BOLD contrast can be improved by increasing the range of FiO_2 levels studied, particularly at ultra-high field. Susceptibility-induced distortions rise substantially as field strength increases, but the BOLD contrast also increases. Our work indicates that 50% oxygen is optimal for generating BOLD contrast at 3T with minimal oxygen susceptibility-induced errors. However, acceptable hyperoxia levels for BOLD contrast in these experiments are likely to be even lower at 7T. This is important, as it also reduces the physiologic effects of oxygen that can compromise the accuracy of data and reduce the likelihood of any adverse events.

The main future goal of studies described in Chapters 3 and 4 is to implement brief T_{1a} measurements in human subjects that can be added to ASL study protocols. As discussed, the major technical hurdle is the inflow of inverted spins from outside of the

transmit volume. Some approaches may circumvent this problem. If only early inversion preparation times are used, it is technically possible that inflow of fresh spins can be avoided. It is difficult, however, to determine the time it takes for fresh spins to enter the tagging region. One approach to estimate this time would be to use arterial spin labeling methods that sample the entire inflow curve (132) with the global inversion pulse preparation. If the end of the inflow curve can be determined, this time would correlate with the entry of uninverted spins. Using this information, it may be feasible to estimate the time it takes for uninverted spins to enter the tagging region. Since the acceptable inversion times before the arrival of uninverted spins are likely to be quite short, a more accurate method of determining the T_{1a} value may be to use these values to fit the zero-crossing point.

Future studies of hyperoxia calibrated BOLD/ASL experiments in our animal model will incorporate simultaneous $^{17}\text{O}_2$ inhalation measurement of metabolism. Although our hyperoxia calibrated measurements of relative metabolism compare favorably to metabolic increases previously measured in the same model with $^{17}\text{O}_2$ inhalation, minor differences in animal preparation, including the time course of DNP administration, depth of anesthesia, and other sources of physiological variation between animals will have significant effects. Simultaneous measurements can allow us to greatly reduce these variations, increasing the power of cross-validation of this study. Additionally, we are currently in collaboration with the Yodh Lab to implement simultaneous optical

spectroscopy of flow and metabolism in this animal model (133). Difficulty with light penetration through the skull has kept this technique from working accurately in the past. However, we recently have begun to drill through the skull to place fibers directly on the dura. This should allow for accurate studies and create the possibility of a three-way cross validation of optical data, BOLD/ASL data, and $^{17}\text{O}_2$ inhalation.

We plan to further analyze the proposed model in Chapter 6 with an animal model of altered metabolism. As mentioned above, a moderate hypothermia protocol may be ideally suited to this task. It also may be possible to perform this experiment in our hypermetabolic swine model, with the expectation that hyperoxic R_1 enhancement will be reduced upon DNP administration.

While many of these studies above have been performed in animal models, some of these can be translated to human studies. For example, the experiments performed using a swine model (Chapter 5) can be performed in humans, although metabolic alteration methods other than DNP must be used (such as visual stimulation). A cross-validation study using hyperoxic calibrated function MRI and $^{17}\text{O}_2$ inhalation would be ideal in humans, because of the ability to localize and repeat cerebral stimulation paradigms. Similarly, the experiments performed on rats in Chapter 6 can also be performed using human subjects. The use of lower levels of CO_2 would be necessary in this context, as high levels are not well-tolerated even by healthy subjects (107). This study in humans

may actually be easier than animal models, as testing our model against CMRO_2 changes can easily be achieved using functional MRI protocols. For the reasons discussed above, the one exception where animal studies may be necessary are studies measuring T_{1a} .

7.2 Summary of Dissertation

As presented in Chapter 1, interest in the use of inhaled oxygen as an intravascular contrast agent has increased due to a number of attractive features. These include wide availability, low cost, high tolerability, lack of contraindications, minimal physiologic effects, and rapid wash-in and wash-out times of this contrast agent. Although numerous applications using hyperoxia have emerged, its use as a quantitative MRI contrast agent continues to be hampered by the lack of a complete understanding of the nature and extent of its effects *in vivo*. This thesis has focused on several areas where crucial mechanisms of hyperoxia contrast need further elucidation *in vivo*: (1) the effects of gaseous and dissolved paramagnetic molecular oxygen on BOLD and ASL data, (2) the degree and temporal characteristics CBF reduction during hyperoxia, (3) the use of hyperoxia in quantitative measurements of metabolism with calibrated BOLD/ASL data, and (4) the biophysical mechanisms of hyperoxic T_1 contrast.

We have demonstrated that the paramagnetic effects of molecular oxygen significantly complicate the analysis of BOLD-modulated hyperoxic contrast studies of the brain in

Chapter 2. Negative signal changes that were observed in T_2^* -weighted images in the frontal lobes, ventricles, and brain periphery suggested the influence of image distortions and increased intravoxel dephasing from oxygen-induced susceptibility changes in and around the upper airway. Static field changes during oxygen inhalation were shown to scale with the main magnetic field strength and FiO_2 . Reducing FiO_2 was shown to reduce negative signal changes while still maintaining adequate BOLD contrast for accurate CBV calculation.

Using measurements of phantoms and arterial blood *in vivo*, we demonstrated in Chapter 3 that T_{1a} is well described by the linear combination of longitudinal relaxivities of molecular oxygen and deoxyhemoglobin. We also found that when comparing brief and graded hyperoxic inhalation paradigms, T_{1a} changes rapidly with changing FiO_2 and does not change over time. In Chapter 4, we showed with simultaneous *in vivo* measurements of T_{1a} and CBF that measured reductions in CBF using ASL during hyperoxia are dominated by T_{1a} reduction during short term inhalation epochs. For longer hyperoxic exposures, physiologic effects such as reduced action of nitric oxide seem to be the dominant source of ASL signal reduction.

In Chapter 5, we demonstrated the feasibility of accurate $CMRO_2$ measurements with hyperoxia calibrated simultaneous BOLD/ASL data in a hypermetabolic animal model. Although producing slightly different calibration measurements, hyperoxia and

hypercapnia were shown to produce very similar results in detecting changes in CMRO_2 . Finally, we found similar increases in CMRO_2 using our hyperoxia calibrated BOLD/ASL data as compared to measurements using $^{17}\text{O}_2$ inhalation in the same animal model.

We established a biophysical model of the relationship between hyperoxic R_1 enhancement and blood flow, blood volume, and metabolism in Chapter 6. Our model predicts that hyperoxic R_1 enhancement increases with faster blood flow and less tissue oxygen consumption, showing opposite behavior to BOLD contrast that is complementary for differing physiological conditions. Isometabolic increases in CBF were shown to be accurately described by the model, but testing this model in the setting of altered metabolism will be necessary for its complete validation.

In conclusion, we hope that this work provides valuable knowledge and insights that increase the accuracy and utility of hyperoxia as a quantitative MRI contrast agent. We anticipate that this contrast agent will continue to play an expanding and invaluable role in numerous clinical and research settings.

REFERENCES

1. Emsley J. The elements. Oxford New York: Clarendon Press; Oxford University Press; 1998. vii, 292 p. p.
2. Fleming I. Molecular orbitals and organic chemical reactions. Hoboken, N.J.: Wiley; 2010. xii, 515 p. p.
3. Mellon EA, Beesam RS, Baumgardner JE, Borthakur A, Witschey WR, II, Reddy R. Estimation of the regional cerebral metabolic rate of oxygen consumption with proton detected (17)O MRI during precision (17)O(2) inhalation in swine. *Journal of Neuroscience Methods* 2009;179(1):29-39.
4. Tornroth-Horsefield S, Neutze R. Opening and closing the metabolite gate. *Proceedings of the National Academy of Sciences of the United States of America* 2008;105(50):19565-19566.
5. Sicard KM, Duong TQ. Effects of hypoxia, hyperoxia, and hypercapnia on baseline and stimulus-evoked BOLD, CBF, and CMRO₂ in spontaneously breathing animals. *Neuroimage* 2005;25(3):850-858.
6. Chiarelli PA, Bulte DP, Wise R, Gallichan D, Jezzard P. A calibration method for quantitative BOLD fMRI based on hyperoxia. *Neuroimage* 2007;37(3):808-820.
7. Raichle ME, Gusnard DA. Appraising the brain's energy budget. *Proceedings of the National Academy of Sciences of the United States of America* 2002;99(16):10237-10239.
8. Perlmutter JS, Herscovitch P, Powers WJ, Fox PT, Raichle ME. Standardized Mean Regional Method for Calculating Global Positron Emission Tomographic Measurements. *Journal of Cerebral Blood Flow and Metabolism* 1985;5(3):476-480.
9. Bloembergen N, Purcell EM, Pound RV. Relaxation Effects in Nuclear Magnetic Resonance Absorption. *Physical Review* 1948;73(7):679-712.
10. Bloch F. Nuclear Induction. *Physical Review* 1946;70(7-8):460-474.

11. Bloembergen N, Morgan LO. Proton Relaxation Times in Paramagnetic Solutions Effects of Electron Spin Relaxation. *Journal of Chemical Physics* 1961;34(3):842.
12. Bloembergen N. Proton Relaxation Times in Paramagnetic Solutions. *Journal of Chemical Physics* 1957;27(2):572-573.
13. Solomon I. Relaxation Processes in a System of 2 Spins. *Physical Review* 1955;99(2):559-565.
14. Kubo R, Tomita K. A General Theory of Magnetic Resonance Absorption. *Journal of the Physical Society of Japan* 1954;9(6):888-919.
15. Gutowsky HS, Woessner DE. NUCLEAR MAGNETIC SPIN-LATTICE RELAXATION IN LIQUIDS. *Physical Review* 1956;104(3):843-844.
16. Pauling L, Coryell CD. The Magnetic Properties and Structure of Hemoglobin, Oxyhemoglobin and Carbonmonoxyhemoglobin. *Proc Natl Acad Sci U S A* 1936;22(4):210-216.
17. Chen H, Ikeda-Saito M, Shaik S. Nature of the Fe-O₂ Bonding in Oxy-Myoglobin: Effect of the Protein. *Journal of the American Chemical Society* 2008;130(44):14778-14790.
18. Koenig SH, Spiller M, Brown RD, Wolf GL. Relaxation of Water Protons in the Intracellular and Extracellular Regions of Blood Containing Gd(DTPA). *Magnetic Resonance in Medicine* 1986;3(5):791-795.
19. Thulborn KR, Waterton JC, Matthews PM, Radda GK. Oxygenation Dependence of the Transverse Relaxation-Time of Water Protons in Whole-Blood at High-Field. *Biochimica Et Biophysica Acta* 1982;714(2):265-270.
20. Stanisz GJ, Li JG, Wright GA, Henkelman RM. Water dynamics in human blood via combined measurements of T₂ relaxation and diffusion in the presence of gadolinium. *Magnetic Resonance in Medicine* 1998;39(2):223-233.
21. Blockley NP, Jiang L, Gardener AG, Ludman CN, Francis ST, Gowland PA. Field Strength Dependence of R₁ and R₂* Relaxivities of Human Whole Blood to ProHance, Vasovist, and Deoxyhemoglobin. *Magnetic Resonance in Medicine* 2008;60(6):1313-1320.

22. Zhao JM, Clingman CS, Narvainen MJ, Kauppinen RA, van Zijl PCM. Oxygenation and Hematocrit dependence of transverse relaxation rates of blood at 3T. *Magnetic Resonance in Medicine* 2007;58(3):592-597.
23. Silvennoinen MJ, Clingman CS, Golay X, Kauppinen RA, van Zijl PCM. Comparison of the dependence of blood R-2 and R*(2) on oxygen saturation at 1.5 and 4.7 Tesla. *Magnetic Resonance in Medicine* 2003;49(1):47-60.
24. Wright GA, Hu BS, Macovski A. Estimating Oxygen-Saturation of Blood In Vivo with MR Imaging at 1.5T. *Jmri-Journal of Magnetic Resonance Imaging* 1991;1(3):275-283.
25. Morgan LO, Murphy J, Cox PF. Proton Spin Relaxation in Aqueous Solutions of Paramagnetic Ions .3. Copper(II) Diamine Complexes. *Journal of the American Chemical Society* 1959;81(19):5043-5047.
26. Teng CL, Hong H, Kiihne S, Bryant RG. Molecular oxygen spin-lattice relaxation in solutions measured by proton magnetic relaxation dispersion. *Journal of Magnetic Resonance* 2001;148(1):31-34.
27. Mirhej ME. Proton Spin Relaxation by Paramagnetic Molecular Oxygen. *Canadian Journal of Chemistry* 1965;43(5):1130.
28. Parker DS, Harmon JF. Dipolar Spin-Lattice Relaxation in Water Containing Oxygen. *Chemical Physics Letters* 1974;25(4):505-506.
29. Molinari F, Puderbach M, Eichinger M, Ley S, Fink C, Bonomo L, Kauczor HU, Bock M. Oxygen-enhanced magnetic resonance imaging: Influence of different gas delivery methods on the T1-changes of the lungs. *Investigative Radiology* 2008;43(6):427-432.
30. Nekolla S, Gneiting T, Syha J, Deichmann R, Haase A. T1 Maps by k-Space Reduced SNAPSHOT-FLASH MRI. *Journal of Computer Assisted Tomography* 1992;16(2):327-332.
31. Winter JD, Akens MK, Cheng HLM. Quantitative MRI assessment of VX2 tumour oxygenation changes in response to hyperoxia and hypercapnia. *Physics in Medicine and Biology* 2011;56(5):1225-1242.

32. O'Connor JPB, Naish JH, Jackson A, Waterton JC, Watson Y, Cheung S, Buckley DL, McGrath DM, Buonaccorsi GA, Mills SJ, Roberts C, Jayson GC, Parker GJM. Comparison of Normal Tissue R-1 and R-2* Modulation by Oxygen and Carbogen. *Magnetic Resonance in Medicine* 2009;61(1):75-83.
33. O'Connor JPB, Naish JH, Parker GJM, Waterton JC, Watson Y, Jayson GC, Buonaccorsi GA, Cheung S, Buckley DL, McGrath DM, West CML, Davidson SE, Roberts C, Mills SJ, Mitchell CL, Hope L, Ton C, Jackson A. Preliminary Study of Oxygen-Enhanced Longitudinal Relaxation in MRI: a potential novel biomarker of oxygen changes in solid tumors. *International Journal of Radiation Oncology Biology Physics* 2009;75(4):1209-1215.
34. O'Connor JPB, Jackson A, Buonaccorsi GA, Buckley DL, Roberts C, Watson Y, Cheung S, McGrath DM, Naish JH, Rose CJ, Dark PM, Jayson GC, Parker GJM. Organ-specific effects of oxygen and carbogen gas inhalation on tissue longitudinal relaxation times. *Magnetic Resonance in Medicine* 2007;58(3):490-496.
35. Berkowitz BA. Role of dissolved plasma oxygen in hyperoxia-induced contrast. *Magnetic Resonance Imaging* 1997;15(1):123-126.
36. Bulte D, Chiarelli P, Wise R, Jezzard P. Measurement of cerebral blood volume in humans using hyperoxic MRI contrast. *Journal of Magnetic Resonance Imaging* 2007;26(4):894-899.
37. Bulte DP, Chiarelli PA, Wise RG, Jezzard P. Cerebral perfusion response to hyperoxia. *Journal of Cerebral Blood Flow and Metabolism* 2007;27(1):69-75.
38. Goodwin JA, Vidyasagar R, Balanos GM, Bulte D, Parkes LM. Quantitative fMRI using hyperoxia calibration: Reproducibility during a cognitive Stroop task. *Neuroimage* 2009;47(2):573-580.
39. Mark CI, Fisher JA, Pike GB. Improved fMRI calibration: Precisely controlled hyperoxic versus hypercapnic stimuli. *Neuroimage* 2011;54(2):1102-1111.

40. Jensen FB. Red blood cell pH, the Bohr effect, and other oxygenation-linked phenomena in blood O₂ and CO₂ transport. *Acta Physiologica Scandinavica* 2004;182(3):215-227.
41. Watson NA, Beards SC, Altaf N, Kassner A, Jackson A. The effect of hyperoxia on cerebral blood flow: a study in healthy volunteers using magnetic resonance phase-contrast angiography. *European Journal of Anaesthesiology* 2000;17(3):152-159.
42. Becker HF, Polo O, McNamara SG, BerthonJones M, Sullivan CE. Effect of different levels of hyperoxia on breathing in healthy subjects. *Journal of Applied Physiology* 1996;81(4):1683-1690.
43. Johnston AJ, Steine LA, Gupta AK, Menon DK. Cerebral oxygen vasoreactivity and cerebral tissue oxygen reactivity. *British Journal of Anaesthesia* 2003;90(6):774-786.
44. Johnston AJ, Steiner LA, Balestreri M, Gupta AK, Menon DK. Hyperoxia and the cerebral hemodynamic responses to moderate hyperventilation. *Acta Anaesthesiologica Scandinavica* 2003;47(4):391-396.
45. Poulin MJ, Liang PJ, Robbins PA. Fast and slow components of cerebral blood flow response to step decreases in end-tidal PCO₂ in humans. *Journal of Applied Physiology* 1998;85(2):388-397.
46. Zaharchuk G, Martin AJ, Dillon WP. Noninvasive imaging of quantitative cerebral blood flow changes during 100% oxygen inhalation using arterial spin-labeling MR imaging. *American Journal of Neuroradiology* 2008;29(4):663-667.
47. Duong TQ, Iadecola C, Kim SG. Effect of hyperoxia, hypercapnia, and hypoxia on cerebral interstitial oxygen tension and cerebral blood flow. *Magnetic Resonance in Medicine* 2001;45(1):61-70.
48. Floyd TF, Clark JM, Gelfand R, Detre JA, Ratcliffe S, Guvakov D, Lambertsen CJ, Eckenhooff RG. Independent cerebral vasoconstrictive effects of hyperoxia and accompanying arterial hypocapnia at 1 ATA. *Journal of Applied Physiology* 2003;95(6):2453-2461.

49. Kolbitsch C, Lorenz IH, Hormann C, Hinteregger M, Lockinger A, Moser PL, Kremser C, Schocke M, Felber S, Pfeiffer KP, Benzer A. The influence of hyperoxia on regional cerebral blood flow (rCBF), regional cerebral blood volume (rCBV) and cerebral blood flow velocity in the middle cerebral artery (CBFVMCA) in human volunteers. *Magnetic Resonance Imaging* 2002;20(7):535-541.
50. Demchenko IT, Boso AE, O'Neill TJ, Bennett PB, Piantadosi CA. Nitric oxide and cerebral blood flow responses to hyperbaric oxygen. *Journal of Applied Physiology* 2000;88(4):1381-1389.
51. Allen BW, Demchenko IT, Piantadosi CA. Two faces of nitric oxide: implications for cellular mechanisms of oxygen toxicity. *Journal of Applied Physiology* 2009;106(2):662-667.
52. Reinstrup P, Ryding E, Ohlsson T, Dahm PL, Uski T. Cerebral Blood Volume (CBV) in Humans during Normo- and Hypocapnia - Influence of Nitrous Oxide (N₂O). *Anesthesiology* 2001;95(5):1079-1082.
53. Rostrup E, Larsson HBW, Toft PB, Garde K, Henriksen O. Signal changes in gradient-echo images of human brain induced by hypoxia and hyperoxia. *NMR in Biomedicine* 1995;8(1):41-47.
54. Fridovich I. Oxygen toxicity: A radical explanation. *Journal of Experimental Biology* 1998;201(8):1203-1209.
55. Imlay JA. Pathways of oxidative damage. *Annual Review of Microbiology* 2003;57:395-418.
56. Groger M, Radermacher P, Speit G, Muth CM. Genotoxicity of hyperbaric oxygen and its prevention: what hyperbaric physicians should know. *Diving and Hyperbaric Medicine* 2008;38(4):200-205.
57. Djurhuus R, Svardal AM, Thorsen E. Glutathione in the cellular defense of human lung cells exposed to hyperoxia and high pressure. *Undersea & Hyperbaric Medicine* 1999;26(2):75-85.

58. Freiburger J, Coulombe K, Suliman H, Carraway M, Piantadosi C. Superoxide dismutase responds to hyperoxia in rat hippocampus. *Undersea & Hyperbaric Medicine* 2004;31(2):227-232.
59. Smerz RW. Incidence of oxygen toxicity during the treatment of dysbarism. *Undersea & Hyperbaric Medicine* 2004;31(2):199-202.
60. Hampson N, Atik D. Central nervous system oxygen toxicity during routine hyperbaric oxygen therapy. *Undersea & Hyperbaric Medicine* 2003;30(2):147-153.
61. Butler FK, White E, Twa M. Hyperoxic myopia in a closed-circuit mixed-gas scuba diver. *Undersea & Hyperbaric Medicine* 1999;26(1):41-45.
62. Bitterman H. Bench-to-bedside review: Oxygen as a drug. *Critical Care* 2009;13(1).
63. Jackson RM. Pulmonary Oxygen Toxicity. *Chest* 1985;88(6):900-905.
64. Hoshino T, Okamoto M, Sakazaki Y, Kato S, Young HA, Aizawal H. Role of Proinflammatory Cytokines IL-18 and IL-1 beta in Bleomycin-Induced Lung Injury in Humans and Mice. *American Journal of Respiratory Cell and Molecular Biology* 2009;41(6):661-670.
65. Santosh C, Brennan D, McCabe C, Macrae IM, Holmes WM, Graham DI, Gallagher L, Condon B, Hadley DM, Muir KW, Gsell W. Potential use of oxygen as a metabolic biosensor in combination with T2*-weighted MRI to define the ischemic penumbra. *Journal of Cerebral Blood Flow and Metabolism* 2008;28(10):1742-1753.
66. Dani KA, Santosh C, Brennan D, Condon B, Macrae IM, Hadley DM, Shaw M, Muir KW. Oxygen Challenge with T2*MRI as a Metabolic Biomarker In Acute Ischemic Stroke Patients. *Stroke* 2009;40(4):E116-E116.
67. Baskerville TA, Deuchar GA, McCabe C, Robertson CA, Holmes WM, Santosh C, Macrae IM. Influence of 100% and 40% oxygen on penumbral blood flow, oxygen level, and T(2)(star)-weighted MRI in a rat stroke model. *Journal of Cerebral Blood Flow and Metabolism* 2011;31(8):1799-1806.

68. Robertson CA, McCabe C, Gallagher L, Lopez-Gonzalez MD, Holmes WM, Condon B, Muir KW, Santosh C, Macrae IM. Stroke penumbra defined by an MRI-based oxygen challenge technique: 2. Validation based on the consequences of reperfusion. *Journal of Cerebral Blood Flow and Metabolism* 2011;31(8):1788-1798.
69. Baudelet C, Gallez B. How does blood oxygen level-dependent (BOLD) contrast correlate with oxygen partial pressure (pO₂) inside tumors? *Magnetic Resonance in Medicine* 2002;48(6):980-986.
70. McGrath DM, Naish JH, O'Connor JPB, Hutchinson CE, Waterton JC, Taylor CJ, Parker GJM. Oxygen-induced changes in longitudinal relaxation times in skeletal muscle. *Magnetic Resonance Imaging* 2008;26(2):221-227.
71. Zaharchuk G, Busse RF, Rosenthal G, Manley GT, Glenn OA, Dillon WP. Noninvasive oxygen partial pressure measurement of human body fluids in vivo using magnetic resonance imaging. *Academic Radiology* 2006;13(8):1016-1024.
72. Losert C, Peller M, Schneider P, Reiser M. Oxygen-enhanced MRI of the brain. *Magnetic Resonance in Medicine* 2002;48(2):271-277.
73. Tadamura E, Hatabu H, Li W, Prasad PV, Edelman RR. Effect of oxygen inhalation on relaxation times in various tissues. *Journal of Magnetic Resonance Imaging* 1997;7(1):220-225.
74. Anzai Y, Ishikawa M, Shaw DWW, Artru A, Yarnykh V, Maravilla KR. Paramagnetic effect of supplemental oxygen on CSF hyperintensity on fluid-attenuated inversion recovery MR images. *American Journal of Neuroradiology* 2004;25(2):274-279.
75. Weast RC. *CRC handbook of chemistry and physics*. Boca Raton, FL: CRC Press; 1988.
76. Egan DF, Wilkins RL, Stoller JK, Scanlan CL. *Egan's fundamentals of respiratory care*. St. Louis, Mo.: Mosby; 2003.
77. Smith SM, Jenkinson M, Woolrich MW, Beckmann CF, Behrens TEJ, Johansen-Berg H, Bannister PR, De Luca M, Drobnjak I, Flitney DE, Niazy RK, Saunders

- J, Vickers J, Zhang YY, De Stefano N, Brady JM, Matthews PM. Advances in functional and structural MR image analysis and implementation as FSL. *Neuroimage* 2004;23:S208-S219.
78. McGonigle DJ, Howseman AM, Athwal BS, Friston KJ, Frackowiak RSJ, Holmes AP. Variability in fMRI: An examination of intersession differences. *Neuroimage* 2000;11(6):708-734.
 79. Zhang YY, Brady M, Smith S. Segmentation of brain MR images through a hidden Markov random field model and the expectation-maximization algorithm. *IEEE Transactions on Medical Imaging* 2001;20(1):45-57.
 80. Jenkinson M, Smith S. A global optimisation method for robust affine registration of brain images. *Medical Image Analysis* 2001;5(2):143-156.
 81. Hood CM, Schroter RC, Doorly DJ, Blenke E, Tolley NS. Computational modeling of flow and gas exchange in models of the human maxillary sinus. *Journal of Applied Physiology* 2009;107(4):1195-1203.
 82. Raj D, Paley DP, Anderson AW, Kennan RP, Gore JC. A model for susceptibility artefacts from respiration in functional echo-planar magnetic resonance imaging. *Physics in Medicine and Biology* 2000;45(12):3809-3820.
 83. Lu HZ, Law M, Johnson G, Ge YL, van Zijl PCM, Helpert JA. Novel approach to the measurement of absolute cerebral blood volume using vascular-space-occupancy magnetic resonance imaging. *Magnetic Resonance in Medicine* 2005;54(6):1403-1411.
 84. Severinghaus JW. Simple, accurate equations for human blood O₂ dissociation computations. *Journal of Applied Physiology* 1979;46(3):599-602.
 85. Zeng HR, Constable RT. Image distortion correction in EPI: Comparison of field mapping with point spread function mapping. *Magnetic Resonance in Medicine* 2002;48(1):137-146.
 86. Fernandez-Seara MA, Wehrli FW. Postprocessing technique to correct for background gradients in image-based R-2(*) measurements. *Magnetic Resonance in Medicine* 2000;44(3):358-366.

87. Poser BA, Norris DG. Fast spin echo sequences for BOLD functional MRI. *Magnetic Resonance Materials in Physics Biology and Medicine* 2007;20(1):11-17.
88. Noseworthy MD, Kim JK, Stainsby JA, Stanisz GJ, Wright GA. Tracking oxygen effects on MR signal in blood and skeletal muscle during hyperoxia exposure. *Journal of Magnetic Resonance Imaging* 1999;9(6):814-820.
89. Buxton RB, Frank LR, Wong EC, Siewert B, Warach S, Edelman RR. A general kinetic model for quantitative perfusion imaging with arterial spin labeling. *Magnetic Resonance in Medicine* 1998;40(3):383-396.
90. Thomas DL, Lythgoe MF, Gadian DG, Ordidge RJ. In vivo measurement of the longitudinal relaxation time of arterial blood (T-1a) in the mouse using a pulsed arterial spin labeling approach. *Magnetic Resonance in Medicine* 2006;55(4):943-947.
91. Nichols MB, Paschal CB. Measurement of longitudinal (T1) relaxation in the human lung at 3.0 Tesla with tissue-based and regional gradient analyses. *Journal of Magnetic Resonance Imaging* 2008;27(1):224-228.
92. Lu HZ, Clingman C, Golay X, van Zijl PCM. Determining the longitudinal relaxation time (T-1) of blood at 3.0 tesla. *Magnetic Resonance in Medicine* 2004;52(3):679-682.
93. Lu J, Dai G, Egi Y, Huang S, Kwon SJ, Lo EH, Kim YR. Characterization of cerebrovascular responses to hyperoxia and hypercapnia using MRI in rat. *Neuroimage* 2009;45(4):1126-1134.
94. Sicard K, Shen Q, Brevard ME, Sullivan R, Ferris CF, King JA, Duong TQ. Regional cerebral blood flow and BOLD responses in conscious and anesthetized rats under basal and hypercapnic conditions: Implications for functional MRI studies. *Journal of Cerebral Blood Flow and Metabolism* 2003;23(4):472-481.
95. Kalisch R, Elbel GK, Gossel C, Czisch M, Auer DP. Blood pressure changes induced by arterial blood withdrawal influence bold signal in anesthetized rats at 7 tesla: Implications for pharmacologic MRI. *Neuroimage* 2001;14(4):891-898.

96. Wong EC, Buxton RB, Frank LR. Quantitative imaging of perfusion using a single subtraction (QUIPSS and QUIPSS II). *Magnetic Resonance in Medicine* 1998;39(5):702-708.
97. Luh WM, Wong EC, Bandettini PA, Hyde JS. QUIPSS II with thin-slice TI1 periodic saturation: A method for improving accuracy of quantitative perfusion imaging using pulsed arterial spin labeling. *Magnetic Resonance in Medicine* 1999;41(6):1246-1254.
98. Wong EC, Buxton RB, Frank LR. Implementation of quantitative perfusion imaging techniques for functional brain mapping using pulsed arterial spin labeling. *Nmr in Biomedicine* 1997;10(4-5):237-249.
99. Wegener S, Wu WC, Perthen JE, Wong EC. Quantification of rodent cerebral blood flow (CBF) in normal and high flow states using pulsed arterial spin labeling magnetic resonance imaging. *Journal of Magnetic Resonance Imaging* 2007;26(4):855-862.
100. Kohler TR, Jawien A. Flow affects development of intimal hyperplasia after arterial injury in rats. *Arteriosclerosis and Thrombosis* 1992;12(8):963-971.
101. Buxton RB. Quantifying CBF with arterial spin labeling. *Journal of Magnetic Resonance Imaging* 2005;22(6):723-726.
102. Frank LR, Wong EC, Haseler LJ, Buxton RB. Dynamic imaging of perfusion in human skeletal muscle during exercise with arterial spin labeling. *Magnetic Resonance in Medicine* 1999;42(2):258-267.
103. Cavusoglu M, Pfeuffer J, Ugurbil K, Uludag K. Comparison of pulsed arterial spin labeling encoding schemes and absolute perfusion quantification. *Magnetic Resonance Imaging* 2009;27(8):1039-1045.
104. Donahue MJ, Lu HZ, Jones CK, Edden RAE, Pekar JJ, van Zijl PCM. Theoretical and experimental investigation of the VASO contrast mechanism. *Magnetic Resonance in Medicine* 2006;56(6):1261-1273.

105. Wansapura JP, Holland SK, Dunn RS, Ball WS. NMR relaxation times in the human brain at 3.0 tesla. *Journal of Magnetic Resonance Imaging* 1999;9(4):531-538.
106. Paxinos G, Watson C. *The rat brain in stereotaxic coordinates*. San Diego: Academic Press; 1997.
107. Hoge RD, Atkinson J, Gill B, Crelier GR, Marrett S, Pike GB. Investigation of BOLD signal dependence on cerebral blood flow and oxygen consumption: The deoxyhemoglobin dilution model. *Magnetic Resonance in Medicine* 1999;42(5):849-863.
108. Hofmann M, Bezrukov I, Mantlik F, Aschoff P, Steinke F, Beyer T, Pichler BJ, Scholkopf B. MRI-Based Attenuation Correction for Whole-Body PET/MRI: Quantitative Evaluation of Segmentation- and Atlas-Based Methods. *Journal of Nuclear Medicine* 2011;52(9):1392-1399.
109. Mellon EA, Beesam RS, Elliott MA, Reddy R. Mapping of cerebral oxidative metabolism with MRI. *Proceedings of the National Academy of Sciences of the United States of America* 2010;107(26):11787-11792.
110. Baumgardner JE, Mellon EA, Tailor DR, Mallikarjunarao K, Borthakur A, Reddy R. Mechanical ventilator for delivery of O_2 in brief pulses. *Open Biomed Eng J* 2008;2:57-63.
111. Clark WG, Clark YL. Changes in Body Temperature After Administration of Anti-Pyretics, LSD, delta-9-THC, CNS Depressants and Stimulants, Hormones, Inorganic-Ions, Gases, 2,4-DNP and Miscellaneous Agents. *Neuroscience and Biobehavioral Reviews* 1981;5(1):1-136.
112. Dai WY, Garcia D, de Bazelaire C, Alsop DC. Continuous Flow-Driven Inversion for Arterial Spin Labeling Using Pulsed Radio Frequency and Gradient Fields. *Magnetic Resonance in Medicine* 2008;60(6):1488-1497.
113. Wu W-C, Fernandez-Seara M, Detre JA, Wehrli FW, Wang J. A theoretical and experimental investigation of the tagging efficiency of pseudocontinuous arterial spin labeling. *Magnetic Resonance in Medicine* 2007;58(5):1020-1027.

114. Wang JJ, Alsop DC, Li L, Listerud J, Gonzalez-At JB, Schnall MD, Detre JA. Comparison of quantitative perfusion imaging using arterial spin labeling at 1.5 and 4.0 tesla. *Magnetic Resonance in Medicine* 2002;48(2):242-254.
115. Boxerman JL, Bandettini PA, Kwong KK, Baker JR, Davis TL, Rosen BR, Weisskoff RM. The Intravascular Contribution to fMRI Signal Change - Monte-Carlo Modeling and Diffusion-Weighted Studies In-Vivo. *Magnetic Resonance in Medicine* 1995;34(1):4-10.
116. Grubb RL, Raichle ME, Eichling JO, Terpogos.Mm. Effects of Changes in PaCO₂ on Cerebral Blood Volume, Blood Flow, and Vascular Mean Transit Time. *Stroke* 1974;5(5):630-639.
117. Leenders KL, Perani D, Lammertsma AA, Heather JD, Buckingham P, Healy MJR, Gibbs JM, Wise RJS, Hatazawa J, Herold S, Beaney RP, Brooks DJ, Spinks T, Rhodes C, Frackowiak RSJ, Jones T. Cerebral Blood Flow, Blood Volume, and Oxygen Utilization - Normal Values and Effect with Age. *Brain* 1990;113:27-47.
118. Battisti-Charbonney A, Fisher J, Duffin J. The cerebrovascular response to carbon dioxide in humans. *Journal of Physiology-London* 2011;589(12):3039-3048.
119. Xu F, Uh J, Brier MR, Hart J, Yezhuvath US, Gu H, Yang YH, Lu HZ. The influence of carbon dioxide on brain activity and metabolism in conscious humans. *Journal of Cerebral Blood Flow and Metabolism* 2011;31(1):58-67.
120. Chen JJ, Pike GB. Global cerebral oxidative metabolism during hypercapnia and hypocapnia in humans: implications for BOLD fMRI. *Journal of Cerebral Blood Flow and Metabolism* 2010;30(6):1094-1099.
121. Kaanders J, Bussink J, van der Kogel AJ. ARCON: a novel biology-based approach in radiotherapy. *Lancet Oncology* 2002;3(12):728-737.
122. Krause BJ, Beck R, Souvatzoglou M, Piert M. PET and PET/CT studies of tumor tissue oxygenation. *Quarterly Journal of Nuclear Medicine and Molecular Imaging* 2006;50(1):28-43.
123. Takeshita K, Kawaguchi K, Fujii-Aikawa K, Ueno M, Okazaki S, Ono M, Krishna MC, Kuppusamy P, Ozawa T, Ikota N. Heterogeneity of Regional Redox

- Status and Relation of the Redox Status to Oxygenation in a Tumor Model, Evaluated Using Electron Paramagnetic Resonance Imaging. *Cancer Research* 2010;70(10):4133-4140.
124. Magat J, Jordan BF, Cron GO, Gallez B. Noninvasive mapping of spontaneous fluctuations in tumor oxygenation using (19)F MRI. *Medical Physics* 2010;37(10):5434-5441.
 125. Rijpkema M, Kaanders J, Joosten FBM, van der Kogel AJ, Heerschap A. Effects of breathing a hyperoxic hypercapnic gas mixture on blood oxygenation and vascularity of head-and-neck tumors as measured by magnetic resonance imaging. *International Journal of Radiation Oncology Biology Physics* 2002;53(5):1185-1191.
 126. Steinhoff S, Zaitsev M, Zilles K, Shah NJ. Fast T(1) mapping with volume coverage. *Magnetic Resonance in Medicine* 2001;46(1):131-140.
 127. Aradi M, Steier R, Bukovics P, Szalay C, Perlaki G, Orsi G, Pal J, Janszky J, Doczi T, Schwarcz A. Quantitative proton MRI and MRS of the rat brain with a 3T clinical MR scanner. *Journal of Neuroradiology* 2011;38(2):90-97.
 128. Deoni SCL. High-resolution T1 mapping of the brain at 3T with driven equilibrium single pulse observation of T1 with high-speed incorporation of RF field inhomogeneities (DESPOT1-HIFI). *Journal of Magnetic Resonance Imaging* 2007;26(4):1106-1111.
 129. Frietsch T, Krafft P, Piepgras A, Lenz C, Kuschinsky W, Waschke KF. Relationship between local cerebral blood flow and metabolism during mild and moderate hypothermia in rats. *Anesthesiology* 2000;92(3):754-763.
 130. Krafft P, Frietsch T, Lenz C, Piepgras A, Kuschinsky W, Waschke KF. Mild and moderate hypothermia (alpha-stat) do not impair the coupling between local cerebral blood flow and metabolism in rats. *Stroke* 2000;31(6):1393-1400.
 131. Gold J. Metabolic Profiles in Human Solid Tumors.I. A New Technique for Utilization of Human Solid Tumors in Cancer Research and Its Application to

- Anaerobic Glycolysis of Isologous Benign and Malignant Colon Tissues. *Cancer Research* 1966;26(4P1):695.
132. Francis ST, Bowtell R, Gowland PA. Modeling and optimization of Look-Locker spin labeling for measuring perfusion and transit time changes in activation studies taking into account arterial blood volume. *Magnetic Resonance in Medicine* 2008;59(2):316-325.
133. Durduran T, Yu GQ, Burnett MG, Detre JA, Greenberg JH, Wang JJ, Zhou C, Yodh AG. Diffuse optical measurement of blood flow, blood oxygenation, and metabolism in a human brain during sensorimotor cortex activation. *Optics Letters* 2004;29(15):1766-1768.